

AD-A039 899

STANFORD UNIV CALIF CENTER FOR MATERIALS RESEARCH
SOLID ELECTROLYTE BATTERY MATERIALS. (U)
NOV 74 R A HUGGINS
CMR-74-16

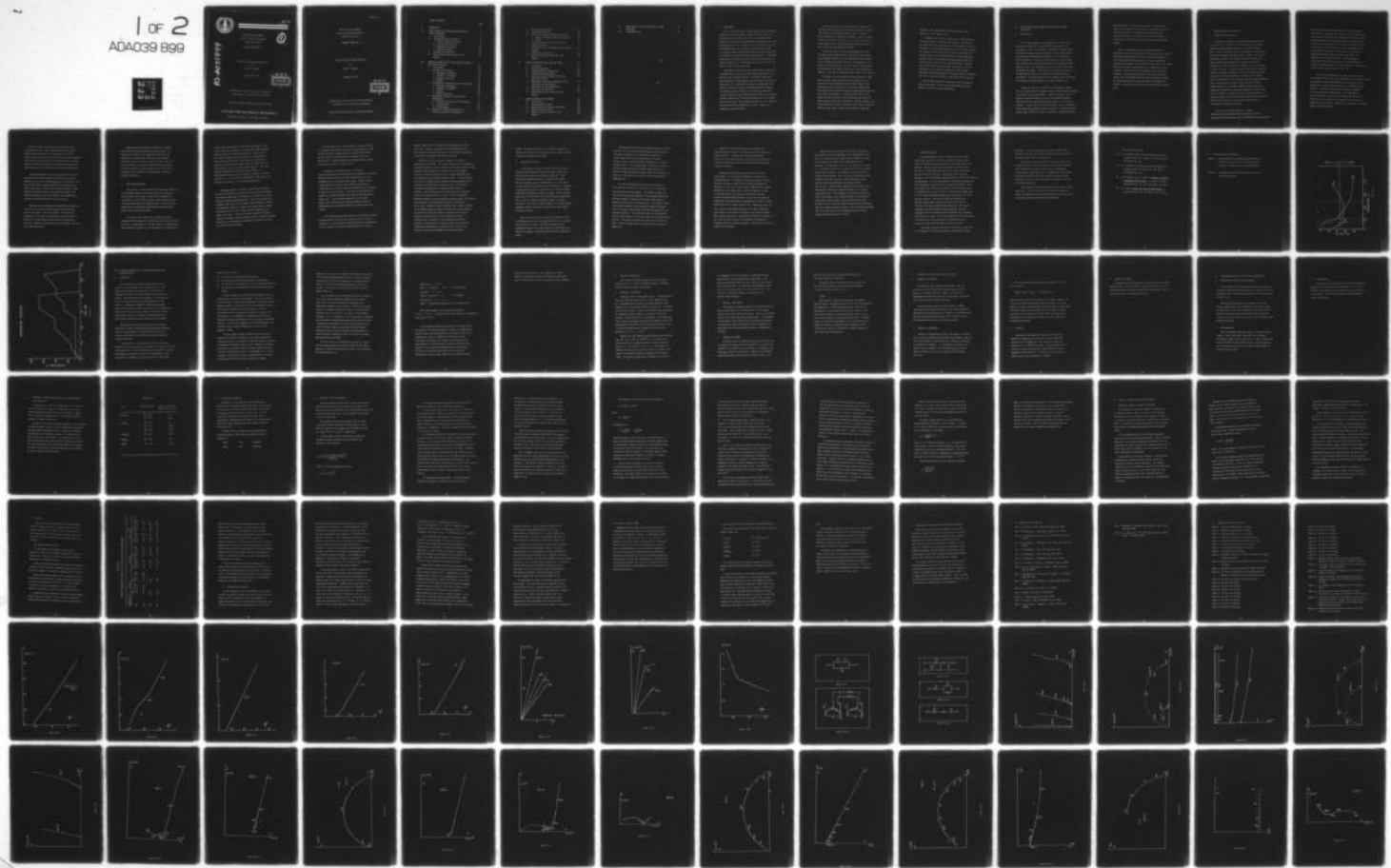
UNCLASSIFIED

F/G 10/2

N00014-67-A-0112-0075

NL

1 of 2
ADA039 899





JAN 20 1975

CMR-74-16

OFFICE OF NAVAL RESEARCH

Contract N00014-67-A-0112-0075

Task No. NR 056-555

TECHNICAL REPORT NO. 3

①

B.S.

Solid Electrolyte Battery Materials

by

Robert A. Huggins

November 30, 1974



Reproduction in whole or in part is permitted for
any purpose of the United States Government

Approved for Public Release; Distribution Unlimited

CENTER FOR MATERIALS RESEARCH ✓

STANFORD UNIVERSITY • STANFORD, CALIFORNIA

CMR-74-16 ✓

OFFICE OF NAVAL RESEARCH

Contract N00014-67-A-0112-0075 ✓

Task No. NR 056-555

TECHNICAL REPORT NO. 3 ✓

Solid Electrolyte Battery Materials

by

Robert A. Huggins

November 30, 1974



Reproduction in whole or in part is permitted for
any purpose of the United States Government

Approved for Public Release; Distribution Unlimited

TABLE OF CONTENTS

	Page
I. INTRODUCTION	1
II. OXIDE FABRICATION VIA CONTROLLED OXIDATION OF POLYMER PRECURSORS	4
A. Introduction	4
B. Experimental Work and Results	6
1. Polymer Precursor Materials	6
2. Salt Soaking Processes	9
3. Decomposition Behavior	13
4. Oxidation Behavior	17
C. References for Section II	19
D. Figure Captions for Section II, and Figures	20
III. ELECTRICAL CONDUCTIVITY OF SOME LITHIUM SILICATES AND ALUMINO-SILICATES	21
A. Introduction	21
B. Materials Investigated	26
1. $\text{LiAlSi}_2\text{O}_6$, β -spodumene	26
2. LiAlSiO_4 , β -eucryptite	27
3. $\text{Li}_2\text{Si}_2\text{O}_5$ and Li_2SiO_3	27
4. Li_4SiO_4	28
C. Preparation and Characterization of Materials	29
1. $\text{LiAlSi}_2\text{O}_6$, β -spodumene	29
2. LiAlSiO_4 , β -eucryptite	29
3. $\text{Li}_2\text{Si}_2\text{O}_5$	30
4. Li_2SiO_3 and Li_4SiO_4	31
D. Experimental Aspects of the Electrical Measurements	32
1. Preparation of Samples for Measurements	32
2. ac Measurements	32
3. dc Measurements	33
E. Variation of Apparent Conductivity at Constant Frequency with Temperature	34

F.	dc Polarization Results	36
G.	Equivalent Parameters	37
H.	Results of Frequency Response Measurements	45
1.	LiAlSi_2 , LiAlSiO_4 , $\text{Li}_2\text{Si}_2\text{O}_5$, and Li_2SiO_3	45
2.	Li_4SiO_4	48
I.	Electrical Conductivity of Silicates and Alumino-Silicates	55
J.	Discussion of the Interpretation of Frequency Response	57
K.	References for Section III	58
L.	Figure Captions for Section III, and Figures	60
IV. DEFECT STRUCTURE OF ABX_4 , A_2BX_5 AND A_3BX_6		62
A.	Introduction	62
B.	Intrinsic Equilibria	64
C.	Nonstoichiometric Compositions	66
D.	Electronic Minority Defects	70
E.	Equivalent Concentrations of Ionic and Electronic Defects	74
F.	Influence of Aliovalent Impurities on the Ionic Defect Concentrations	79
G.	Discussion and Concluding Remarks	85
H.	References for Section IV	90
I.	Figure Captions for Section IV, and Figures	91
V. GRAPHITE INTERCALATION COMPOUNDS		92
A.	Introduction	92
B.	Carbon/Fluorine Systems	92
C.	Graphite/Antimony Pentafluoride System	93
D.	References for Section V	94
E.	Figure Captions for Section V, and Figures	95

VI.	OTHER POTENTIAL SOLID ELECTROLYTES OR MIXED CONDUCTORS	96
VII.	DISTRIBUTION LIST	97

I. INTRODUCTION

This is the third technical report relating to work on Solid Electrolyte Battery Materials. During the past 18 months our efforts have had two major aims: one is to develop a novel technique for producing beta alumina solid electrolytes for use in the sodium-sulfur cell. The other is to search for new fast ion conducting materials for lithium and potassium ions, as well as to examine mixed conductor materials for potential application as electrodes in advanced secondary battery designs. The details and results of our efforts for the first year are presented in Technical Report No. 2. The present report covers the first six months of effort in the second year.

The viability has now been well demonstrated for the use of the sodium-sulfur cell as a potential high energy density, high specific power, secondary battery. The Central Electricity Generating Board in Great Britain, with an electric delivery van operating off of a sodium-sulfur battery, has shown that this system is definitely feasible for powering electric vehicles. The Companie General d'Electricity in France has shown that suitable lifetimes (about 1300 amp-hours per cm^2) can be achieved with the sodium-sulfur cell provided high quality, beta alumina electrolyte is used. The overriding problem now is to reduce the costs of manufacturing these cells in order to make it an economically feasible venture.

A prime cost factor in the sodium-sulfur cell design is that for producing the beta alumina solid electrolyte. Because beta alumina is a refractory material, costly classical ceramic fabrication techniques are required. This is worsened by the need to control the sodium vapor pressure in order to reduce sodium loss at temperatures above 900°C, and, thus, be able to maintain close composition control.

The main objective of this research program is to show that solid, bulk, oxide materials, specifically beta alumina, can be prepared through controlled decomposition and oxidation of salt infiltrated polymer precursors. The simplicity of the process, as well as the fact that the materials are fabricated at temperatures below 1000°C, implies that a very significant reduction in the cost of producing ceramic bodies can be realized.

The reason that the sodium-sulfur system presently is the most attractive solid electrolyte battery system is due to the fact that beta alumina is the only really useful, solid electrolyte material available for large scale applications. Both lithium and potassium secondary cell systems potentially have more useful characteristics. Lithium systems could provide higher specific energy than does the sodium-sulfur system, as well as greater open-circuit potentials. Potassium systems could provide operation at lower temperatures. Thus, there is a need to find new, solid, fast, lithium and potassium ion conducting

materials. This need forms the base for the other main objective of this research work.

In addition to the above, there also is a need for better electrode materials, especially for cathodes. The problems encountered with the sulfur side of the sodium-sulfur cells are an example. The non-conductive nature of sulfur, which requires the presence of a current collector such as carbon felt, and the poor wetting of the electrolyte by the sodium polysulfide reaction product, which leads to poor electrical contact with the electrolyte, have only been partially overcome. Thus, as part of the present research program, we also are pursuing an investigation of a variety of potentially useful cathode materials, particularly graphite intercalates, which have already been shown to have some utility in high energy density systems.

The following sections of this report discuss progress in some of these areas. Others have been mentioned in previous reports, or will be included subsequently.

II. OXIDE FABRICATION VIA CONTROLLED OXIDATION OF POLYMER PRECURSORS

A. Introduction

We have been engaged in the development of a rather novel processing technique for the production of beta-alumina solid electrolytes. This is an attempt to circumvent the normal ceramic fabrication processes presently required. This technique involves the controlled decomposition and oxidation of salt infiltrated polymer precursors. The goals of this work are to produce defect-free, coherent, bulk oxide materials which have specified chemical compositions and crystallographic structures and which have useful thicknesses and shapes. The properties of these materials are to be determined and they are to be used in electrochemical cell experiments. The overall process and the primary factors which must be considered have been presented in previous reports [1,2].

During the first year of effort in this program we showed that the polymer precursor technique could be used to produce materials of specified chemical composition. Sodium beta alumina as well as sodium and lithium aluminates and pure and stabilized zirconia materials have been prepared using filter paper as the precursor material. In the course of this work we found a new, low temperature phase, $\text{Na}_2\text{O} \cdot \text{xAl}_2\text{O}_3$ having the mullite structure. A potassium analog exists, also. Further, we found a new hydrate of sodium aluminate,

$\text{Na}_2\text{O} \cdot \text{Al}_2\text{O}_3 \cdot 6\text{H}_2\text{O}$. In addition, we were able to prepare dense, defect free, transport foils of alumina and translucent foils of zirconia 15 microns in thickness, using cellophane as the precursor material. As a result of this work we were able to define many of the more important factors affecting the overall process.

With the achievements and the knowledge gained in the first year of work our orientation for the second year was shifted towards producing material with useful thickness and shapes in order that property measurements could be made. Significant progress has been made in this direction in that defect free, alumina materials 80 microns in thickness have now been made, as well as glassy carbon tubes 3.0 mm in diameter and 0.5 mm in wall thickness. New precursor materials are also being considered with the aim of increasing oxide yield and decreasing the extent of overall shrinkage, and thus decreasing the propensity for cracking. The details and results of this work will be presented below.

B. Experimental Work and Results

1. Polymer Precursor Materials

Work with cellophane as a standard precursor material has been enlightening. Cellophane is a regenerated cellulose not requiring further treatment before use. We have determined many of the more important factors contributing to the processing steps through studies with this material. However, the limited thicknesses available (38 microns) precludes its further use, since shrinkage during processing to the oxide reduces the thickness to a final value around 15 microns, which is too thin to handle with ease. Various types of dialysis tubing, which are basically the same as cellophane, are of only limited use, also, since their starting thicknesses are no more than 90 microns and after processing to the oxide this reduces to about 35 microns, still a very fragile foil. Thus, we have turned our efforts towards working with esterified cellulose materials which are commercially available in much greater thicknesses and in a wide variety of shapes. Cellulose esters can be easily dissolved in suitable solvents and we can cast shapes having any wall thickness desired (and without any of the additives which might be encountered in commercial material).

The use of esterified cellulose requires a saponification (de-esterification) step in order to give a regenerated cellulose material that is thermosetting (the esterified

forms are thermoplastic) and which can be used with aqueous salt systems. This processing, however, gives a material which is structurally different from cellophane (or dialysis tubing). The latter material has a significant amount of crystallinity as revealed by x-ray diffraction. The crystalline form present is closely related to but not exactly the "Crystalline-II" or "soda-cellulose" structure. X-ray diffraction analysis of saponified material, however, indicates that there is no significant crystallinity present. A moderate degree of crystallinity can be induced, however, through treating the material in boiling water for at least two hours. "Cellulose-II" is the crystal structure formed in this case.

The basic de-esterification procedure used is that given by Erickson and Brown [3] for the deacetylation of cellulose acetate. We found, however, that slight modification is required for its application to mixed ester materials such as cellulose acetate-butyrate. This material must first be swollen in methanol and then reacted with methanol/NaOH. The preswelling is necessary in order to open the structure so that the base can have access to the interior of the material and, thus, effect complete de-esterification. Ethanol is not as effective a swelling agent for the mixed esters.

Ammonia has much the same effect on cellulose as does sodium hydroxide [4]. Thus, saponification was tried using NH_4OH in place of NaOH in order to eliminate Na from the structure and give more direct control of final oxide composition. Positive results were obtained for cellulose acetate. However, NH_4OH is not sufficiently active to completely de-esterify the mixed esters and thus, cannot be used for their saponification.

The saponification step has a strong effect also on the distribution of carboxyl groups in the regenerated cellulose. Evidence for this comes from measurements of cation uptake. The data were obtained by microprobe analysis of materials at the glassy carbon stage. We have found different amounts of cation uptake for different batches of de-esterified material. No consistent behavior has yet been observed, but experiments are underway to determine the cause of this phenomenon.

Measurements of the density of de-esterified materials not treated in salt, but heat-treated through the glassy carbon stage to 600°C , gave a value of 1.32 gm/cc. The density was independent of the type of saponification treatment studied or whether or not the material was pretreated in boiling water. There was a temperature dependence, as one would expect, but this will be discussed below.

Measurements were also made of the density of glassy carbon stage material produced from dialysis tubing. The measurements revealed a very significant lowering of the density due to boiling water treatment of the precursor. Microprobe analysis of related samples revealed a large drop in cation uptake as a result of the boiling water treatment. The precise reasons for these changes are not clear, but it is apparent that a boiling water pretreatment of dialysis tubing is detrimental.

2. Salt Soaking Processes

In an attempt to clear up some of the questions relating to the interaction between the precursor and the salt solution, a study was made of the effects of anion and cation type and concentration, and the effect of mixed cations and mixed anions on cation uptake during the soaking process. To this end, the compositions of glassy carbon stage materials were determined using electron microprobe analysis.

For a single salt system, AlCl_3 , aluminum ion uptake decreased with decreasing salt concentration, but the behavior was not linear. Mixing anions, Cl^- and NO_3^- , resulted in significantly lower aluminum ion uptake, with the least amount (a 33% decrease)

occurring when equal amounts of each anion were present. Only a small difference was observed in cation uptake when comparing aluminum nitrate with zirconium oxychloride. Mixing sodium with aluminum (same salt system) results in a large decrease (25%) in total cation uptake, though dilution with water or the mixing of anions has no further effect on either the total cation uptake or the ratio of the cations taken up. This ratio, generally independent of precursor or salt system, is approximately twice the ratio of sodium to aluminum in the salt solution, i.e., if in the salt we have Na:Al ~ 1:10, then in the polymer we have Na:Al = 1:5, as noted previously [2].

Cellophane soaked in a saturated sulfate salt solution of one molar concentration in aluminum ion took up 5% more aluminum ions than one would expect for soaking in a nitrate salt solution of similar aluminum ion concentration. This of course would give a greater oxide yield for the sulfate treated materials. However, the composition analysis of sulfate salt treated samples revealed the presence of up to 3% by weight of sulfur remaining in the glassy carbon state. Further, the sulfur remains in the relic through the oxidation and high temperature heat treatment processing, giving rise to the formation of oxysulfide compounds rather than the alumina materials desired.

We also found that up to 1% by weight of chlorine remains at the glassy carbon stage for chloride treated materials. With excessive amounts of sodium present this tends to form sodium chloride even at the oxide stage when temperatures have not exceeded 850°C. Higher temperature treatments, however, remove the chlorine and give the desired phases.

In addition to the above effects, we observed that when nitrate salt treated materials were decomposed along with sulfate treated materials, the former would contain up to 1% by weight sulfur at the glassy carbon stage. Further, nitrate treated materials containing sodium showed the presence of sodium chloride at the oxide stage when decomposed in the presence of chloride treated materials. These observations indicate that transfer is occurring through the gas phase in the decomposition furnace tube. The most likely mechanism is via the acid (H_2SO_4 or $HC1$) resulting from reaction between the water of decomposition and the residual chlorine or sulfate ions in the polymer.

X-ray diffraction has been carried out on different precursor materials soaked in various salt solutions and dried at room temperature. The crystallinity initially present in cellophane was lost as a result of treatment in chloride base salts (with or

without sodium), but it was unaffected by treatment in nitrate base salts. However, treatment of de-esterified materials in these same salt solutions resulted in the formation of significant crystallinity, especially when sodium was present.

In the past we have been using inorganic salt systems exclusively for this work. The primary reason is their availability and high solubility in water. However, the chemical strength of these inorganic salts prompted us to consider less active, organic systems. The major obstacle is that most organic aluminum salts are insoluble or only slightly soluble in water. We found that the acid form of aluminum acetate, formed by reacting aluminum sulfate and barium acetate, was quite soluble in water. The reaction precipitates barium sulfate, leaving aluminum acetate in solution. After filtering out the barium sulfate, the solution could then be concentrated to at least 2 molar by evaporation. Soaking cellophane in this concentrated aluminum acetate salt solution and subsequently decomposing and oxidizing it resulted in a defect free, transparent foil of aluminum oxide. However, DTA/TGA of such imbibed material revealed the same characteristic behavior as observed for materials treated in inorganic salt solutions, apparently signifying that no real advantage was gained. Aluminum acetate treatment of thicker regenerated cellulose obtained by saponification of cellulose esters still resulted in cracking upon decomposition, though the extent was much less severe as compared with inorganic salt treated materials.

Further work with this salt will be pursued in attempts to improve the behavior for thick materials and to observe effects occurring when combined with sodium.

3. Decomposition Behavior

As noted above, soaking in concentrated salt solutions followed by room temperature drying has marked effects upon the crystalline structure of cellulosic materials. This crystalline cellulosic structure is altered still further during the initial stages of decomposition, i.e., the period of heat treatment where absorbed water is coming off. Amorphous, de-esterified materials not treated in a salt solution develop significant crystallinity through this range. Those materials which have been salt soaked and already developed crystallinity tend to lose it, except for materials treated in chloride base salts. These latter materials appear to be forming unknown compounds, evidence for which is first noted in some samples treated to only 60°C.

Most, if not all, of the crystalline cellulose structure has disappeared from all salt treated materials by the time they have been heated to 120°C. No further manifestations of crystallinity appear with further heating to high temperatures (with the exception of sodium chloride formation, as discussed above).

Thermal analysis of various precursor materials treated in different salt solutions show essentially the same behavior for all samples decomposed under non-oxidizing conditions. A typical weight loss versus temperature curve in either purified argon or purified nitrogen atmospheres for a constant heating rate of 2.5°C per minute (TGA) is presented in Figure 1a. The heat exchange associated with this typical behavior is given by differential thermal analysis (DTA) and is presented in Figure 1b. Note that this is similar to the data presented previously [2].

The overall decomposition process can be divided into four regions as indicated in Figure II-1, each of which may be associated with specific behavior. The extent of weight loss and the depth and precise position of the associated endothermic DTA peak in Region I depends upon how much absorbed water is present (as well as upon the heating rate). The extent of weight loss and the intensity of the endotherms in Region II appears to be a function of how much salt has been incorporated into the cellulose structure. The "twin" peak nature of this endotherm has been characteristic of all the inorganic salt systems examined thus far. Only minor differences have been noted for different salts. These are slight shifts in the temperatures at which the peaks occur.

Region III is characterized only by the weight loss behavior observed with TGA. No associated heat effects have been observed with DTA. In Region IV no further decomposition reactions are occurring and, thus, no heat effects are observed. A small but measureable weight loss is observed with increasing temperature, however.

Obviously gross changes are taking place in the first three regions, all of which have significant bearing on the shrinkage behavior. In attempts to reduce the severity of these reactions, and thus to reduce the rate and non-uniformity of shrinkage, we have tried a wide variety of heating rates, soaking temperatures, and soaking times. Consistent behavior in terms of obtaining defect free, glassy carbon material from salt treated, saponified cellulose esters, has not yet been observed. Decomposition heating schedules representing the extremes of those examined thus far are shown in Figure II-2. Relatively defect free (only several, small blisters present) thick (80μ) alumina has been obtained in each case, yet successive runs have not always given equally good results. Significant variations in procedure at this time can only be related to differences in decomposition atmosphere and de-acetylation processing. Further analysis of this situation is in progress.

Measurements have been made of the density of specimens heat treated to various temperatures in the decomposition cycle. For both untreated and salt soaked dialysis tubing, the density does not change appreciably (within experimental error) throughout the temperature range where decomposition takes place, i.e., in Regions II and III. The density at 320°C for untreated material was 1.50 gm/cc. The presence of salt gives rise to slightly lower densities. For 2.5 M AlCl₃ treated material the density at 230°C was 1.44 gm/cc, while for dialysis tubing treated in AlCl₃ containing Na⁺, the density at 250°C was 1.41 gm/cc. However, small temperature effects exist as one observes when comparing the densities obtained for different decomposition runs. With increases in temperature from 600 to 735°C, there appears to be a slight decrease in the density of glassy carbon stage materials obtained from dialysis tubing precursors, while for de-acetylated cellulose acetate precursors there is a slight increase in density. Over the temperature region 600 to 650°C the density of de-esterified cellulose acetate butyrate remains constant at 1.34 gm/cc.

4. Oxidation Behavior

Good oxide products cannot be obtained from poor glassy carbon stage materials. Specimens containing cracks or other flaws at the glassy carbon stage will give only oxide pieces when oxidized. Since our primary problem has been to obtain thick, defect free, glassy carbon stage material, we have concentrated our efforts in that direction. Only a small effort has been expended to date in examining oxidation behavior. Within the constraint of maintaining a slow rate of oxidation as previously discussed [2] we have examined a limited variety of different procedures. These have included fast ($50^{\circ}\text{C}/\text{hr}$) and moderate ($16^{\circ}\text{C}/\text{hr}$) heating rates to temperatures of from 540 to 675°C . Gas flow rates ranging from 20 to 70 cc/min and oxygen concentrations varying from 0.5 to 17% have been utilized. Best results have been obtained using moderate heating rates, and gas flow rates of the order of 50 cc/min with oxygen concentrations of about 4%. Under these conditions, and using dialysis tubing precursors, we obtain transparent foils of aluminum oxide and aluminum oxide containing small amounts of sodium. Also, dense relatively defect free sheets of aluminum oxide, about 80 microns in thickness have been obtained from deacetylated cellulose acetate precursors.

High oxygen concentrations and fast heating rates give rise to a "peeling" or "scaling" oxide product which leads to severe

degradation. This is observed most frequently with the thick materials, but occurs also with the thin materials, and results in the samples being reduced to small pieces.

The amount of cation contained in the glassy carbon stage material determines to a large degree whether or not an otherwise "good" specimen will result in a defect free, oxide product. In other words, a high oxide yield is necessary for a good product. This feature accounts for the poor oxidation results for many specimens, and can be used as a subjective evaluation of factors controlling oxide yield.

Future studies of oxidation behavior will continue along the same lines. A low level effort will be initiated, however, to examine the oxidation characteristics using TGA in conjunction with both scanning and transmission electron microscopy.

C. References for Section II

- [1] R. A. Huggins, "Solid Electrolyte Battery Materials",
Technical Report #1, November, 1973, ONR Task No.
NR 056-555, pp. 8-17.
- [2] R. A. Huggins, "Solid Electrolyte Battery Materials",
Technical Report #2, March, 1974, ONR Task No.
NR 056-555, pp. 7-32.
- [3] P. H. Erickson and B. S. Brown, in Analytical Chemistry
of Polymers: High Polymers 7, ed. Gordon M. Kline,
Interscience Pub. Inc., New York, 1959, pp 97-102.
- [4] K. H. Meyer, Natural and Synthetic High Polymers,
Interscience Pub. Inc., New York, 1950, pp 344=351.

D. Figure Captions for Section II

Figure 1. Thermal Analysis of Cellulosic Materials Treated
in Various Salts: a) TGA at 2.5°C/min, Purified
Nitrogen, b) DTA at 5°C/min, Purified Nitrogen

Figure 2. Decomposition Heating Schedules for Salt Treated
Cellulosic Materials

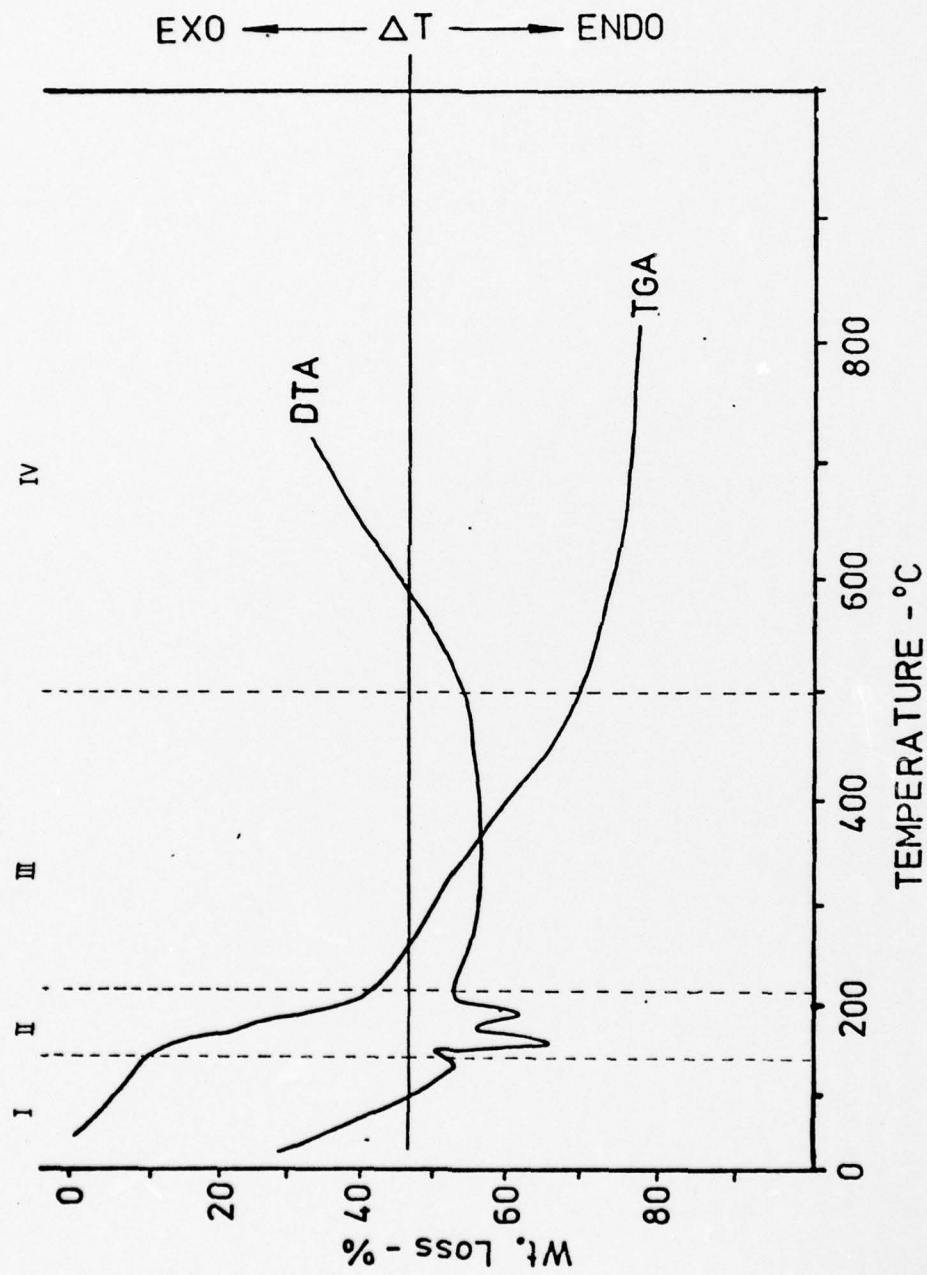


Figure II-1

DECOMPOSITION PROCESSING

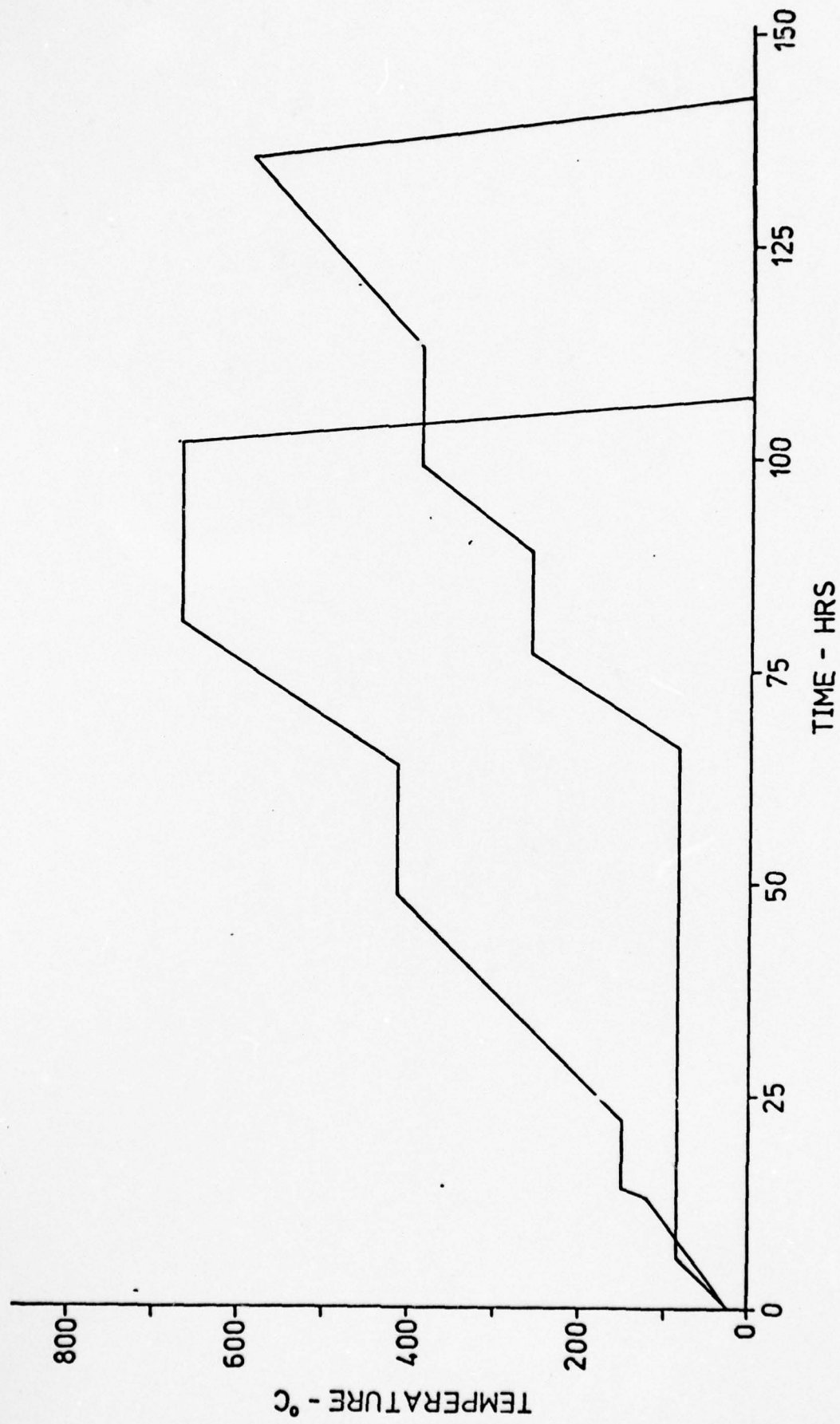


Figure II-2

III. ELECTRICAL CONDUCTIVITY OF SOME LITHIUM SILICATES AND ALUMINO-SILICATES

A. Introduction

At the present time the most highly developed solid electrolyte battery system is the sodium-sulfur cell. This employs liquid sodium and liquid sulfur in the electrode compartments separated by an electrolyte of solid sodium beta-alumina. The advanced state of development of this system is due to the existence and the favorable properties of beta-alumina. A comparative evaluation of possible high energy density battery systems, however, indicates that a cell employing lithium metal as the oxidizable component would have a higher energy output, and it has, therefore, become apparent that a good lithium conducting solid electrolyte would be desirable.

The present report discusses the conductivity results obtained for a number of lithium silicates and alumino-silicates chosen as representatives of different structural types, in the hope of arriving at some conclusions relating structure to transport properties.

A major portion of our program has focused on the interpretation of electrical response as applied to this group of potential solid electrolytes. Such an investigation is essential in removing the ambiguities traditionally attached to measurements of ionic conductivity. Ultimately our study is intended to clarify four

major areas of confusion:

- 1) the role of the sample-electrode interface,
- 2) the interpretation of frequency-dependent measurements,
- 3) the inferences of conductivity data on diffusion mechanisms, and
- 4) the influence of grain boundary diffusion in polycrystalline samples.

We have concluded that two fundamental problems hinder the interpretation of electrical measurements. The first is related to the difficulty in controlling thermodynamic activities in multi-component systems. The second is that in such systems, more than one diffusion mechanism may be contributing to the total conductivity and that unless these processes are separated and characterized, it is impossible to unambiguously attribute an electrical response to the transport of ions through a crystalline lattice. It is this latter problem that has received most of our attention, since it applies to binary as well as to multi-component systems.

The most common procedure for measuring the electrical properties of potential electrolytes is to place a dense polycrystalline pellet of the material between two electrodes which will be blocking to the majority ionic carrier. Although irreversible electrodes are justified by their convenience, they necessitate the use of alternating currents in the measurement of electrical response. Traditionally, the use of high frequency ac currents with blocking electrodes has been considered an adequate

substitute for the use of dc currents with reversible electrodes. It has become strikingly apparent, however, that the frequency-dependence of the electrical response of the sample-electrode system is a particularly important parameter in the interpretation of electrical measurements upon samples containing highly mobile ions.

As a sinusoidal electric potential difference is imposed on a circuit which includes the sample-electrode assembly, there occurs a periodic charging and discharging of the capacitative components of the circuit. The rate at which each capacitor is charged is measured in terms of a characteristic relaxation time, τ , such that $\tau = \omega RC$ where ω is the angular frequency, R is a resistance and C is a capacitance. Therefore, each effective R-C combination existing in the circuit will make a significant contribution to the electrical response only in certain frequency ranges, and when more than one transport mechanism occurs, it is only fortuitous if measurements at a single frequency unambiguously relate to the ionic resistance supposedly being investigated.

We have found it to be particularly valuable to express the ac frequency response as a locus of points in the complex admittance, impedance and permittivity planes. The expressions for these quantities are:

Admittance $\equiv Y = G + jB$

where G = conductance and B = susceptance,

Impedance $\equiv Z = R - jX$

where R = resistance and X = reactance,

Permittivity $\equiv \epsilon = \epsilon' - j\epsilon''$

where ϵ' = dielectric constant and ϵ'' = dielectric loss

Since these parameters are related by translations

$Y = 1/Z = \epsilon'' + j\epsilon'$, the three complex plane figures can be generated from one set of data.

If the imaginary versus the real parts of these expressions are plotted as a function of frequency, particular combinations of circuit elements give characteristic curve shapes on each type of complex plane. Thus, an examination of such plots of the experimental data allows one to propose an equivalent circuit which simulates the relevant physical process involved in the ac response in the frequency and temperature range investigated. The choice of appropriate equivalent circuits under these conditions has recently been a subject of much interest in the

scientific literature [1-7]. The limitations of such a method are the range of frequency available experimentally and the trial and error choice of equivalent circuit components.

B. Materials Investigated

This section will briefly describe the main structural features of the five lithium-containing compounds, $\text{LiAlSi}_2\text{O}_6$, LiAlSiO_4 , $\text{Li}_2\text{Si}_2\text{O}_5$, Li_2SiO_3 , and Li_4SiO_4 .

1. $\text{LiAlSi}_2\text{O}_6$, β -Spodumene

$\text{LiAlSi}_2\text{O}_6$ exists in three modifications. A low temperature form has a diopside chain structure, a high temperature form is a "stuffed"keatite structure, and a high temperature-high pressure form has the stuffed β -quartz structure [8]. In nature, only the first is found, whilst the usual laboratory preparation at atmospheric pressure results in the second: known as β -spodumene, stable above 500°C but meta-stable at room temperature. A wide range of β -spodumene solid solution is known to exist [9], approximately lying between 60 and 80 mole percent SiO_2 . Close to the ideal composition, the tetragonal unit cell has the parameters $a_0 = 7.53$ $c_0 = 9.14^\circ \text{A}$.

Keatite is a high temperature-high pressure modification of SiO_2 [10] ($a_0 = 7.456$ $c_0 = 8.604^\circ \text{A}$). It is constructed of corner-sharing SiO_4 tetrahedra arranged in spirals around the lines $x = 0$, $y = 1/2$ and $x = 1/2$, $y = 0$. The spirals are linked by Si atoms in such a way that each Si is linked to the oxygen of four different spirals, resulting in five membered rings, the cavities of which extend throughout the structure.

In β -spodumene $1/3$ of the Si atoms are replaced by aluminum atoms randomly, and the lithium ions occupy either of two equivalent positions within the rings. There are twice as many sites as lithium ions. The large channels presumably account for the ion exchange properties of this compound [11]. This fact led to the present interest in this material as a possible solid electrolyte.

2. LiAlSiO_4 , β -eucryptite

This material is another example of a "stuffed" structure, [12], but this time is it a superstructure of the β -quartz modification of SiO_2 , rather than keatite. Quartz is the closest packed of the three common silica modifications. It is composed of interlinked helical chains of corner shared SiO_4 tetrahedra. The interstices, which are occupied by Li^+ in eucryptite, are much smaller than the interstices in keatite, crystobalite or tridymite.

3. $\text{Li}_2\text{Si}_2\text{O}_5$ and Li_2SiO_3

By contrast with the previous two structures, the Li^+ ions in $\text{Li}_2\text{Si}_2\text{O}_5$ and Li_2SiO_3 are not "interstitial" in nature but are essential to the cohesion of the framework. In $\text{Li}_2\text{Si}_2\text{O}_5$ (as in $\text{LiAlSi}_4\text{O}_{10}$, petalite) the silicate tetrahedra form 6-membered rings, which share vertices leading to infinite sheets. Two

sheets are held together by ionic bonding through Li^+ , positioned between the layers [13].

In Li_2SiO_3 , rather than forming sheets, the SiO_4 tetrahedra form zig-zag chains, which are again held together by lithium ions lying between them [14].

4. Li_4SiO_4

The structure of Li_4SiO_4 is monoclinic with isolated $(\text{SiO}_4)^{4-}$ groups. The eight lithiums per unit cell are distributed over eighteen 4-, 5- and 6-coordinated sites. West [15] and Völlenkle, et al [17] describe the structure in detail. They also discuss a structural transformation which seems to occur over a broad temperature range between 600 and 725°C. Previous reports on conductivity measurements [15,16] indicate that the lithium ion mobility is unusually high in compounds of this structure type, however, no analysis of frequency response in these systems has been presented.

C. Preparation and Characterization of Materials

1. $\text{LiAlSi}_2\text{O}_6$, β -spodumene

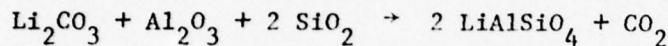
Two samples of this material were prepared. The first was made by a solid state reaction between Li_2CO_3 , SiO_2 and Al_2O_3 , in an alumina crucible at 1200°C . The electrical measurements reported here were made on this sample. X-ray data were in good agreement with the literature.

The second sample, which has not as yet been studied electrically was prepared by quenching a melt of the appropriate composition from just above the m.p. (1225°C) to room temperature, and then annealing below the melting point for about 24-hours. The reaction was carried out in a platinum crucible.

2. LiAlSiO_4 , β -eucryptite

Electrical measurements were made on two samples of LiAlSiO_4 . One of these was obtained from the FOOTE Mineral Company, Exton, Pa. (Lot #114-1021-008, 325 mesh) which will be referred to hereafter as "commercial - LiAlSiO_4 ". No information is available with regard to purity; however, the x-ray powder pattern of this sample was sharp and in very good agreement with published data [12].

The other sample was prepared in this laboratory by a solid state reaction:



The reaction was carried out at 1050°C in an alumina crucible. The mixture was fired twice and reground between firings. The x-ray pattern was again in good agreement with the literature, although the reflections were not quite as sharp as in the commercial sample. An attempt to make LiAlSiO_4 by cooling a melt of the appropriate composition in the presence of LiF/AlF_3 flux [12] produced an unidentifiable material.

3. $\text{Li}_2\text{Si}_2\text{O}_5$

This material was prepared by melting a mixture of the appropriate composition for three hours at about 1200°C and quenching to room temperature. The crystals so formed were annealed in air at 900°C for 48 hours. The x-ray powder pattern indicated a single phase material, whose lines were in good agreement with published data. An earlier batch prepared in a similar way had been contaminated by Li_2SiO_3 .

4. Li_2SiO_3 and Li_4SiO_4

These materials were prepared by a solid state reaction between Li_2CO_3 and SiO_2 . They were heated at about 1200°C for 12 hours, re-ground and heated at the same temperature for 5 hours before confirming the preparation by x-ray powder diffraction.

D. Experimental Aspects of the Electrical Measurements

1. Preparation of Samples for Measurements

A small quantity of the ground material was hot pressed at temperatures between 800 and 1000°C and at a pressure of 6000 psi, in graphite dies. Carbon was then burned off the resulting discs at 800° in air.

The surfaces of the discs were polished using 400 mesh silicon carbide paper and both surfaces of the pellets x-rayed to insure that the surface was composed of the correct material. 1000 Å of platinum was then sputtered onto both surfaces and electrical contact was made to this in the cell, by spring loaded platinum foil discs.

2. ac Measurements

The ac measurements were made using one of three different bridges; General Radio 1608, 1615 and a Hewlett-Packard 4 Frequency automatic bridge, Model 4270 A. Below a conductivity of 100 micro Mhos the 1615 bridge was used. Some discrepancies, up to a maximum of about 12%, were evident between bridges in certain frequency ranges.

3. dc Measurements

dc polarization measurements were made on some samples by applying a dc step voltage of known magnitude (0 - 1 V) and following the resultant current transient using a dc amplifier and a recorder. The current at infinite time was measured using a microammeter.

E. Variation of Apparent Conductivity at Constant Frequency with Temperature

In Figures III-1 - III-4 the conductivity data at 10 kHz in air are plotted as a function of temperature for the four materials $\text{Li}_2\text{Si}_2\text{O}_5$, Li_2SiO_3 , $\text{LiAlSi}_2\text{O}_6$ and LiAlSiO_4 . Li_4SiO_4 will be treated in a later section. The computed activation energies are shown in Table III-1.

In Figure III-5 data for LiAlSiO_4 (prepared in this laboratory) are shown measured in vacuum. The data obtained on cooling from high temperatures presumably reflect a considerable electronic contribution due to reduction in vacuum. The sample was dark grey in color after this treatment. On reoxidizing in air at 900°C the original behavior was restored. LiAlSiO_4 was the only one of the four samples which showed such behavior upon heating in vacuum, although small changes were observed for all samples, as will be noted in the next section.

TABLE III-I.

Sample	Temp. Range (°C)	Apparent Activation Energy (kCal mole ⁻¹)
$\text{Li}_2\text{Si}_2\text{O}_5$	337 - 415	24
	415 - 650	29.4
Li_2SiO_3	140 - 171	21
	171 - 268	10.34
	268 - 527	18.75
$\text{LiAlSi}_2\text{O}_6$	253 - 496	22.82
LiAlSiO_4	212 - 441	19.7
Li_4SiO_4	90 - 730	17.9

F. dc Polarization Results

Measurements of the long time current response upon application of an electric potential difference were carried out in detail only on LiAlSiO_4 , although approximate measurements on $\text{Li}_2\text{Si}_2\text{O}_6$ indicated results of the same form. The final current is a linear function of applied voltage at low temperatures, although there would appear to be some deviation from this at high temperatures and high voltages. (Figures III-6 and III-7).

In Figure III-8, dc conductances are plotted against $(1/T)$ for LiAlSiO_4 . The activation energies for the two regions are:

< 600°C	3.96	kcal/mole
> 600°C	26.15	kcal/mole

G. Equivalent Circuit Parameters

The ideal equivalent circuit for a purely ionic conductor with blocking electrodes can be represented by Figure III-9, where R_1 is the bulk resistance, C_1 is the interfacial capacitance in the microfarad range, and C_2 is the geometric capacitance in the picofarad range.

The complex admittance and impedance plots for such a circuit both contain two distinct regions (Figure III-10).

Note that the peaks of the semicircular portions occur when $\omega_y = (R_1 C_1)^{-1}$ and $\omega_z = (R_1 C_2)^{-1}$, respectively.

For this simple circuit, the frequency at which the transition between the semicircular and straight line portions occurs is given by

$$\omega^2 = \frac{C_1 - 2 C_2 + (C_1^2 - 8 C_1 C_2)^{1/2}}{2 R_1^2 C_1^2 C_2}$$

For $C_1 \gg C_2$, this expression reduces to

$$\omega = 1 / R_1 (C_1 C_2)^{1/2}$$

In a general electrochemical system, there will be three possible contributions to the interfacial capacitance.

1) The compact double layer. This arises as a property of all interfaces and is a physical consequence of the termination of an electrical medium. The characteristic charge balance of the bulk is destroyed and a net surface excess charge induces an opposite charge in the adjacent phase; the separated charges behaving as a capacitance. Values for a compact double layer would be in the 1-50 μ F range.

2) The diffuse double layer. The mobile charge carriers will be distributed over the electrical field according to Boltzmann statistics. The resultant charge distribution is given by the Poisson-Boltzmann equation, which predicts an exponential decay of charge from the interface into the bulk of the solid. Depending on the concentration of the mobile species the electrical field may extend much further in the solid (the Debye length) than would be expected from compact double layer considerations. The diffuse double layer may be represented as a parallel plate capacitor with a much larger plate separation than that of the compact double layer, hence the values of capacitances will be rather smaller.

3) Adsorption pseudocapacitance. A third capacitance which may be observed at interfaces is associated with

adsorption of a charged species at the interface. The concentration of adsorbed species is potential-dependent and adsorption-desorption equilibria may be very rapid, leading to a large apparent capacitance of the interface. If a full monolayer is set as the maximum coverage for an effect of this kind then the observed capacitances may easily be several thousand μ F. As such high capacitances have not been observed in the present work, they will not be discussed further.

The double layer capacitance is expected to be in series electrically with a resistance which hinders the charging and discharging of the double layer. Thus in the present case, the bulk ionic resistance of Li^+ in the electrolyte will be measured as an R. Note that this may well include grain boundary resistances as well as "true" bulk resistance.

For our samples, the center of the half-circle of the admittance plots are often lowered below the G axis, and in the impedance plots the vertical line becomes inclined to the horizontal. This behavior cannot be modeled by any finite network of resistors and capacitors. Instead, it is usual to model such behavior by a Warburg impedance (-W-) which has the properties of an infinite chain of resistors and capacitors (Figure III-11).

The admittance of the Warburg impedance is given by

$$Y = M \omega^{1/2} + j M \omega^{1/2}$$

where

$$M = \sqrt{C'/2 R'}$$

Its impedance is

$$Z = \frac{1}{2 M \omega^{1/2}} - \frac{j}{2 M \omega^{1/2}}$$

A Warburg impedance arises naturally in electrochemistry in those situations where an electrochemical charge transfer step is controlled by a concentration term (at the electrode) which is a solution of Fick's Second Law. In other words, the reaction rate (and the current) is diffusion controlled under conditions in which Fick's Second Law is valid. The usual conditions under which this may occur are:

- a) Electrochemical discharge of the majority carrier to a neutral species which can then diffuse into the bulk of either the electrode or the electrolyte according to Fick's Second Law. This seems unlikely in the present case as there is no evidence of lithium precipitation in either the electrode

or the electrolyte even after long dc polarization times at potentials up to one volt. Normal ac behavior could be observed immediately after a polarization experiment which would surely not be the case if large quantities of lithium were being transported across the interfaces.

b) Electrochemical discharge of a minority carrier in the presence of a large excess of indifferent electrolyte (i.e., an electrolyte which cannot undergo discharge at the electrodes). This is equivalent to saying that, for a charged minority carrier there must be zero internal field in the electrolyte. If there is an internal field Fick's Second Law does not hold.

c) Also, it is a necessary condition that the electrode is relatively reversible to the minority carrier, otherwise the reaction will no longer be diffusion controlled and the electrode kinetics will be all important in determining the Faradaic admittance of the system. It would then appear to be impossible to observe a Warburg impedance and a reaction resistance in the same equivalent circuit. The non-Faradaic admittance will be dominated by the blocked component, in this case the Li^+ .

In the present case minority carriers could be either electrons (or holes) or oxygen ions. In the first case, the concentration on the electrolyte side of the interfaces would be

a linear function of potential difference, whereas if O⁼ were the minority carrier, the activities of O inside the interfaces would be given by the Nernst equation and hence an exponential dependence of current on voltage would be observed in the steady state studies. Referring to the results of the dc polarization experiments on LiAlSiO₄ (Figures III-6 and III-7) a linear dependence of current or voltage is observed, providing strong evidence that either electrons or holes are the predominant minority carrier. A study of the dependence of current on oxygen partial pressure would also be of value at this point.

In an aqueous system the majority and minority carriers move essentially independently of one another and so the Faradaic admittance is independent of the non-Faradaic admittance (double layer charging), and the two admittances appear in parallel (Figure III-12a). This situation may also be true in a solid electrolyte. However, there is an important difference in that local defect equilibria are maintained in the solid even in those regions (i.e., the double layer) where charge neutrality is not adhered to. In other words the charging and discharging of the double layer may be determined by the diffusion of the minority carrier under certain circumstances. In this case, the equivalent circuit may be valid as shown in Figure III-12b.

Both of these circuits predict B-G plots of the form observed, i.e., a half circle with its center lowered below the G axis. Attempts are being made to resolve the problem by fitting data to the theoretical admittance equations for the two circuits.

If C were a compact double layer capacitance than a small temperature coefficient is to be expected. If however C is a diffuse double layer capacitance then it has the form (at the potential of zero charge)

$$C_0 = \left(\frac{K \epsilon_0 e^2 n_0}{2\pi kT} \right)^{1/2}$$

where K is the dielectric constant, ϵ_0 is the permittivity of free space, e is the electronic charge, n_0 is the carrier concentration, and kT is the Boltzmann factor. Thus if the number of charge carriers is independent of temperature (which may well not be the case in these materials) $C \propto T^{-1/2}$.

The Warburg admittance is also temperature dependent

$$M = \frac{Z^2 e^2 n_0 D^{1/2}}{\sqrt{2} k T}$$

where D is the diffusion coefficient. D is presumably exponentially dependent on temperature and so we may expect a much larger temperature dependence of the Warburg than of the double layer capacitance, and we would certainly not expect a negative temperature coefficient. However, temperature dependent carrier concentrations, and a diffusion coefficient which depends on both minority and majority carrier diffusion coefficients make the separation of the various components a formidable task.

H. Results of Frequency Response Measurements

1. $\text{LiAlSi}_2\text{O}_6$, LiAlSiO_4 , $\text{Li}_2\text{Si}_2\text{O}_5$, and Li_2SiO_3

The dependence of electrical response on frequency of the applied signal was similar in the first four materials, when studied in an air atmosphere. (The response of LiAlSiO_4 in vacuum was drastically different, presumably due to the large number of electronic carriers present under these conditions. This resulted in frequency independent conductivities above 300°C).

The following description of the results, therefore, deals with all four materials simultaneously. There are obvious differences in the absolute magnitudes of parameters and the temperatures at which a certain type of behavior occurs, but it seems certain that the behavior of the four materials do not differ significantly in mechanism.

By no means are all the data obtained on these materials included here; sufficient detail, however, is given to illustrate the points of major importance. The response observed may be more conveniently classified by the temperature region in which it occurs. At the end of this section the different temperature regions will be brought together to deduce a composite picture of the response at all temperatures of interest.

Although the entire complex plane curve cannot be examined with the limited frequency range available in a given experiment, the decrease in the bulk resistance of an electrolyte with increasing temperature brings low frequency regions of the curves into the experimentally observable range. Thus the shape of the complex plane curve will change with temperature.

An additional parameter will be used where appropriate for B-G plots where a semicircle appears to have its center below the abscissa (G axis).

$$\alpha = \sin^{-1} \left(\frac{q^2 - 4}{q^2 + 4} \right)$$

where α is the angle between the origin and the center of the circle and $q = G_{\text{max}}/B_{\text{max}}$.

In the lowest temperature region the characteristic B-G plot is of the form seen in Figures III-13, III-15, III-17-III-18, III-19 and III-21. At the very lowest temperatures, an almost vertical-straight line is obtained, but on increasing the temperature the line inches away from the vertical and a low frequency "tail" develops which eventually becomes a minimum with respect to B. For the highest conductivity

samples there is evidence of a low frequency distortion suggesting a semicircle being overtaken by a vertical line. For example, see Figures III-17 and III-19.

The X-R plots are of the form seen in Figures III-14, III-16 and III-20. They are semicircles with their centers lying below the R axis. (This corresponds to a nonvertical B-G line).

As the temperature is increased, it becomes apparent that the low frequency "tail" of the B-G plots is the high frequency end of a semicircle, with its center below the G axis. The circle extends back toward the origin, see data in Figures III-22 and 23. As the temperature is increased still further, the high frequency part of these curves is removed completely from the observable frequency range (≥ 1 MHz) and all that remains is a half circle with its center below the axis. At even higher temperatures the half circle moves up until its center is on the G axis ($\alpha = 0$), see data in Figures III-24, III-26 and III-28. The corresponding X-R plots are of the form seen in Figures III-25, III-27 and III-29.

One additional plot (Figure III-30) is included for β -spodumene at low temperatures in vacuum. This illustrates how the high frequency end of the B-G spectrum falls to a second semicircle rather than continuously increasing.

2. Li_4SiO_4

Figure III-31 contains sketches of complex admittance plots for Li_4SiO_4 obtained at several temperatures and in different ambients. In oxygen, as well as in helium (at lower temperatures), we see that both the semicircular and the vertical regions of the ideal curve (Figure III-10) are distorted.

a) Temperatures above 300°C

For the shapes of the admittance plots in this temperature range, we have assumed the equivalent circuit of Figure III-32, where W is a complex admittance with Warburg-type behavior as discussed earlier.

Since the electronic resistance is large and the geometric capacitance small, they have a negligible contribution to the electrical response in this range of temperature and frequency.

Using a grid search program, we have successfully fit all of the data in this temperature range to the above circuit, and in doing so have obtained values for R, C, and the Warburg coefficient (M) for each temperature. A strong positive temperature dependence is found for each parameter (Table II).

A comparison of data obtained in helium and oxygen ambients shows two major differences. First, the deviation from the ideal complex admittance curve expected for the simple circuit

TABLE III-II

VALUES OF PARAMETERS IN CIRCUIT III-32 FOR Li_4SiO_4 AT HIGH TEMPERATURES

Temperature °C	R_1 ohms	C_1 farads		M ohm ⁻¹ sec ^{1/2}	
		O_2	H_2	O_2	H_2
443	4.43×10^2	3.88×10^2	7.58×10^{-8}	1.18×10^{-8}	1.39×10^{-5}
500	1.35×10^2	1.14×10^2	1.61×10^{-7}	1.58×10^{-8}	3.01×10^{-5}
680	30.2	14.8	3.7×10^{-7}	6.61×10^{-8}	1.88×10^{-4}
730	16.11	9.52	9.67×10^{-7}	1.79×10^{-7}	4.55×10^{-4}
					5.31×10^{-6}

(Figure III-9) is less in helium, particularly at high temperatures. This results in a large decrease in the Warburg coefficient. A corresponding but much smaller decrease in the interfacial capacitance is also calculated but the explanation for this is not clear at this time.

However, a decrease in the Warburg coefficient with decreasing oxygen partial pressure is evidence that oxygen is a minority carrier which is not totally blocked by the metallic electrodes.

Figure III-33 shows the complex admittance and impedance of Li_4SiO_4 at 730°C before, during, and after the introduction of helium into the system.

It has also been found that the ac conductance is greater when the sample is in helium than in air, while the dc conductance remains negligible in both cases. From Figure III-33, it is apparent that the difference in the conductance is not directly related to the presence of the diffusional behavior of the sample-electrode system.

b) Temperatures below 300°C

In this temperature range the resistance is high enough so that the available frequency range gives data in the region beyond the first semicircle for all five compounds. At higher frequencies, there is an additional contribution to the real part of the admittance which prevents a vertical line

from being obtained in the admittance plot up to the maximum frequency of the measurement. A likely explanation for such behavior is that a second semicircle is present and being partially overshadowed by high values of B contributed by the geometric capacitance. Such a model would necessitate the addition of a new resistance to the equivalent circuit, making a total of three if one includes the high electronic resistance. Figure III-34 shows how a complex impedance would be added to the circuit derived from high temperature data and indicates a possible breakdown of this impedance into components. The R_2 and C_2 of Figure III-34 would be commensurate with the inclusion of a resistance and capacitance related to ionic transport across grain boundaries.

In this high frequency range, a more useful interpretation of the results can be obtained from plots of impedance than admittance. Figures III-35a and III-35b show impedance and admittance plots for Li_4SiO_4 which give direct evidence of three contributing resistances. In Figure III-35a each semicircle results from relaxation between parallel R-C components. One notices that circle #3 is lowered below the X (reactance) = 0 plane. This can be explained by relaxation of the $R_3 - C_1 - M$ portion of the circuit in Figure III-34. Reasonable values for these three parameters are $R_3 \sim 1 \times 10^8$ ohms, $C_1 \sim 1 \times 10^{-9}$ F, and $M \sim 1 \times 10^{-7}$ in admittance units. Circle #2 could be a

relaxation of the $R_2 - C_2$ portion with values of $R_2 \sim 1 \times 10^6$ ohms and $C_2 \sim 1 \times 10^{-11}$ F. Circle #3 at high frequencies would then be a relaxation of the $R_1 - C_3$ combination with values of $R_1 \sim 5 \times 10^5$ ohms and $C_3 \sim 5 \times 10^{-12}$ F.

In the admittance plot (Figures III-35b) the second semicircle is not generally seen as such, because the effective capacitance defined by the second semicircle is of the same order of magnitude as the very high frequency capacitance C_3 , which is not in series with a resistance.

Figure III-36 shows the combination of the components in Figure III-34 which would contribute significantly to the region beyond the first semicircle in the admittance plot.

In both plots of Figure III-35 we have indicated the regions from which values of R_1 and R_2 can be obtained according to the circuit in Figure III-34. Interestingly, it is the frequency range in which $R_1 + R_2$ predominates that is commonly available experimentally. Figure III-37 shows a plot of $\log(\sigma T)$ versus $1/T$ for Li_4SiO_4 calculated from this intermediate frequency region for samples in oxygen and in helium. This figure also shows the data presented by West [15] on a similar sample measured in air at a single frequency. At low temperatures, the single frequency measurement gives higher conductivity values since that frequency moves progressively to the right on the admittance plot (Figure III-35b) as the sample

resistance increases. This is a strong argument for the use of frequency dependent measurements, for, unless conductivities are calculated from a critical region of the complex plane plot, they cannot be accurately attributed to any resistance or combination of resistances in the circuit.

It remains now to determine the nature of the resistances that are involved in the equivalent circuit. If a grain boundary model is to be maintained, the lowest resistance of the circuit (R_1) must correspond to the resistance of the ion in the crystal lattice. R_2 would then represent the grain boundary resistance, and C_2 the grain boundary capacitance. It should be noted at this point that although the influence of grain boundaries is only one of several possible explanations for this additional impedance, previous discussions in the literature suggest that this is quite probable [4,14].

In considering this model, two important points must be kept in mind. First, the model does not preclude R_1 and R_2 having identical values. The distinguishable regions of the complex plane plots result from R_2 being shunted by a parallel capacitance, C_2 . Second, the model suggests that ionic motion due to migration through a crystal lattice can be separated from other mechanisms even in polycrystalline samples provided that one is careful to operate in or extrapolate

to the proper frequency range.

Regarding the first point, we have evidence that R_2 is considerably greater than R_1 and thus approximately equal to R_1 and R_2 in our samples of Li_4SiO_4 . At temperatures between 25 and 300°C we have extracted values for R_1 and R_2 from impedance plots such as shown in Figure III-35a. These values are plotted as $\log \sigma T$ versus $1/T$ in Figure III-38 and are shown to represent similar activation energies. Although the sum of R_1 and R_2 may define more accurately the bulk ionic conduction in our samples, we feel that the higher conductivity values related to R_1 are more representative of the properties of the Li_4SiO_4 structure and that such an analysis is necessary if structure-mobility relationships are to be obtained for any potential electrolyte.

I. Electrical Conductivity of Silicates and Alumino-Silicates

The electrical conductivities of the whole group of materials studied at 400°C are:

$\text{Li}_2\text{Si}_2\text{O}_5$	$1.1 \times 10^{-8} (\text{ohm}\cdot\text{cm})^{-1}$
Li_2SiO_3	6.2×10^{-7}
LiAlSiO_4	5.6×10^{-5}
$\text{LiAlSi}_2\text{O}_6$	1.4×10^{-5}
Li_4SiO_4	9.0×10^{-4}

Our results verify that Li_4SiO_4 is among the best of the presently known lithium ion conductors at temperatures above 300°C.

It may be seen that the two materials, LiAlSiO_4 and $\text{LiAlSi}_2\text{O}_6$, where structures are composed of a rigid alumino-silicate framework with interstitial Li ions, are considerably better ionic conductors than the two materials in which the Li^+ ions are essential to the rigidity of the structure. This is by no means unexpected. The second group correspond more closely to classical ionic compounds which are usually very poor ionic conductors, whereas the first group has at least a partial resemblance to materials such as sodium beta-alumina where the sodium ions move through a rigid framework of Al^{3+} and O^- .

ions.

It is proposed, therefore, that future work in the alumino-silicate field should concentrate on the framework type of structure. Stuffed superstructures of both the trydimite and crystobalite modifications of quartz are known (e.g., NaAlSiO_4 , KAISiO_4) and both are rather more open than the beta-quartz structure of β -eucryptite.

In addition the feldspars are an interesting group of materials constructed on the framework principle and some of these materials have been prepared and are under investigation. Many of the silicates and alumino-silicates have several modifications and can form different structures with different cations. There are thus possibilities for making a systematic study of mobility as a function of ionic radius.

J. Discussion of the Interpretation of Frequency Response

Although this work is as yet incomplete, it has proved possible to separate interfacial and bulk effects, to ascribe appropriate values to the various components, and to begin to understand the interface problems associated with solid electrolytes in contact with inert metal electrodes. In the future it is hoped to study the temperature dependence of the interface phenomena, the bulk diffusion coefficients and the grain boundary effects, and to clearly separate grain boundary effects from true bulk (or single crystal) response.

The results obtained for these silicates may have to be modified somewhat in the case of better solid electrolytes. An unusually good conductor for example, should be expected to exhibit a more compact double layer, especially if there is a larger excess of sites over mobile species. Also, the number of carriers would be essentially independent of temperature, and minority carrier effects should be less pronounced.

K. References for Section III

- [1] J. E. Bauerle, *J. Phys. Chem. Solids* 30, 2657 (1969).
- [2] R. D. Armstrong, *J. Electroanal. Chem.* 52, 413 (1974).
- [3] R. D. Armstrong, T. Dickinson, P. M. Willis, *ibid* 48, 47 (1973).
- [4] R. D. Armstrong, T. Dickinson, P. M. Willis, *ibid* 53, 389 (1974).
- [5] J. R. MacDonald, *J. Chem. Phys.* 58, 4982 (1973).
- [6] J. R. MacDonald, *J. Appl. Phys.* 44, 3455 (1973).
- [7] J. R. MacDonald, *J. Electroanal. Chem.* 53, 1 (1974).
- [8] C. T. Li and D. R. Peacor, *Z. Krystallog.* 126, 46 (1968).
- [9] R. Roy, D. M. Roy and E. F. Osborn, *J. Amer. Ceram. Soc.* 33, 152 (1950).
- [10] J. Shropshire, P. P. Keat and P. A. Vaughn, *Z. Kristallog.* 112, 409 (1959).
- [11] G. D. White and T. N. McVay, U. S. Energy Comm. ORNL-2450 (1958).
- [12] H. G. F. Winkler, *Acta Cryst.* 1, 27 (1947).
- [13] F. Liebau, *Acta Cryst.* 14, 389 (1961).
- [14] H. J. Seeman, *Acta Cryst.* 9, 251 (1956).
- [15] A. R. West, *J. Appl. Electrochem.* 3, 327 (1973).
- [16] A. R. West and E. P. Glasser, *J. Mater. Sci.* 5, 676 (1970).

[17] H. Völlenkle, A. Wittmann and H. Novotny, Monat. Chem.
99, 1360 (1968).

[18] R. W. Powers and S. P. Mitoff, General Electric Internal
Report # 74-CRD082 (1973).

L. Figure Captions for Section III.

Figure 1. Electrical Conductivity of $\text{Li}_2\text{Si}_2\text{O}_5$

Figure 2. Electrical Conductivity of Li_2SiO_3

Figure 3. Electrical Conductivity of $\text{LiAlSi}_2\text{O}_6$

Figure 4. Electrical Conductivity of LiAlSiO_4 in Air

Figure 5. Electrical Conductivity of LiAlSiO_4 in Vacuum

Figure 6. dc Polarization Experiment on LiAlSiO_4

Figure 7. dc Polarization Experiment on LiAlSiO_4

Figure 8. dc Conductivity of LiAlSiO_4

Figure 9. Equivalent Circuit for an Ideal Ionic Conductor Between
blocking electrodes

Figure 10. Complex Admittance and Impedance Plots for the Circuit
of Figure 9

Figure 11. Equivalent Circuit Representing a Warburg Admittance

Figure 12. (a) and (b): Equivalent Circuits Representing Two
Models for Diffusion by More Than one Charge Carrier

Figure 13. B-G Data for Li_2SiO_3 at four Temperatures

Figure 14. X-R Data for Li_2SiO_3

Figure 15. B-G Data for $\text{Li}_2\text{Si}_2\text{O}_5$

Figure 16. X-R Data for $\text{Li}_2\text{Si}_2\text{O}_5$

Figure 17. B-G Data for $\text{LiAlSi}_2\text{O}_6$

Figure 18. B-G Data for $\text{LiAlSi}_2\text{O}_6$

Figure 19. B-G Data for LiAlSiO_4

Figure 20. X-R Data for LiAlSiO_4

Figure 21. B-G Data for LiAlSiO_4

Figure 22. B-G Data for LiAlSiO_4

Figure 23. B-G Data for LiAlSiO_4

Figure 24. B-G Data for $\text{LiAlSi}_{2\cdot6}^0$

Figure 25. X-R Data for $\text{LiAlSi}_{2\cdot6}^0$

Figure 26. B-G Data for $\text{LiAlSi}_{2\cdot6}^0$

Figure 27. X-R Data for $\text{LiAlSi}_{2\cdot6}^0$

Figure 28. B-G Data for LiAlSiO_4

Figure 29. X-R Data for $\text{LiAlSi}_{2\cdot6}^0$

Figure 30. B-G Data for $\text{LiAlSi}_{2\cdot6}^0$

Figure 31. Complex Admittance Curves Obtained in two Partial Pressures of Oxygen for Li_4SiO_4 at Several Temperatures

Figure 32. Equivalent Circuit Representing the Electrical Response of Li_4SiO_4 at High Temperatures

Figure 33. Complex Admittance and Impedance Plots for Li_4SiO_4 in Oxygen and in Helium

Figure 34. Proposed Equivalent Circuit Representing Electrical Response of Li_4SiO_4 over the Entire Temperature Range (25-730°C)

Figure 35. a) Impedance, and b) Admittance Plots for Li_4SiO_4 at 200°C

Figure 36. The Portion of the Circuit From Figure 34, which Contributes to the Electrical Response at High Frequencies

Figure 37. Temperature Dependence of the Conductivity of Li_4SiO_4 ; Data Taken in He (0), O_2 (●); Data From West (x). Also Shown is the Electronic Conductivity Determined from Polarization Measurements.

Figure 38. Conductivity Plot for Calculated Values of R_1 and R_2 of Figure 34 for Li_4SiO_4

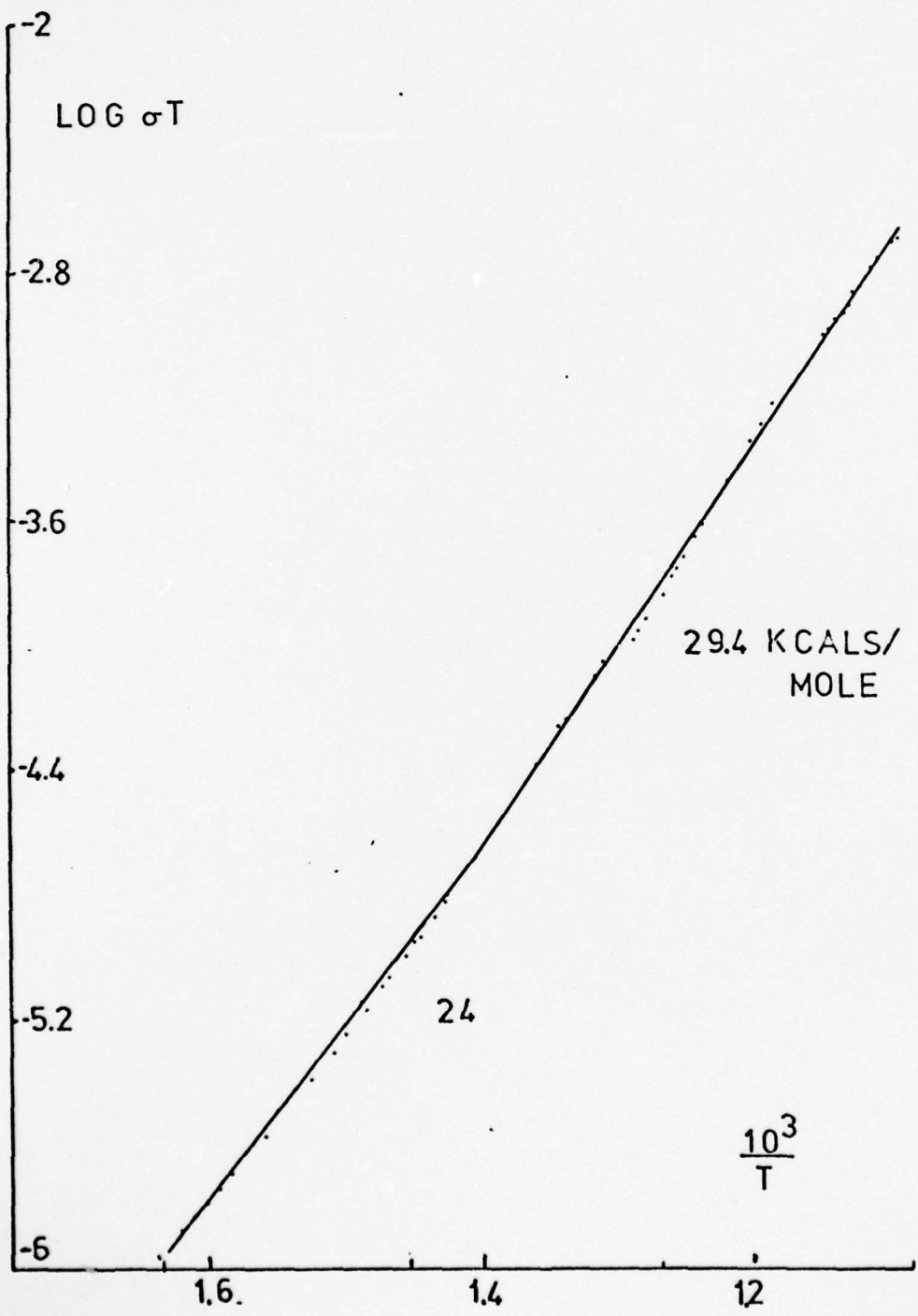


Figure III-1.

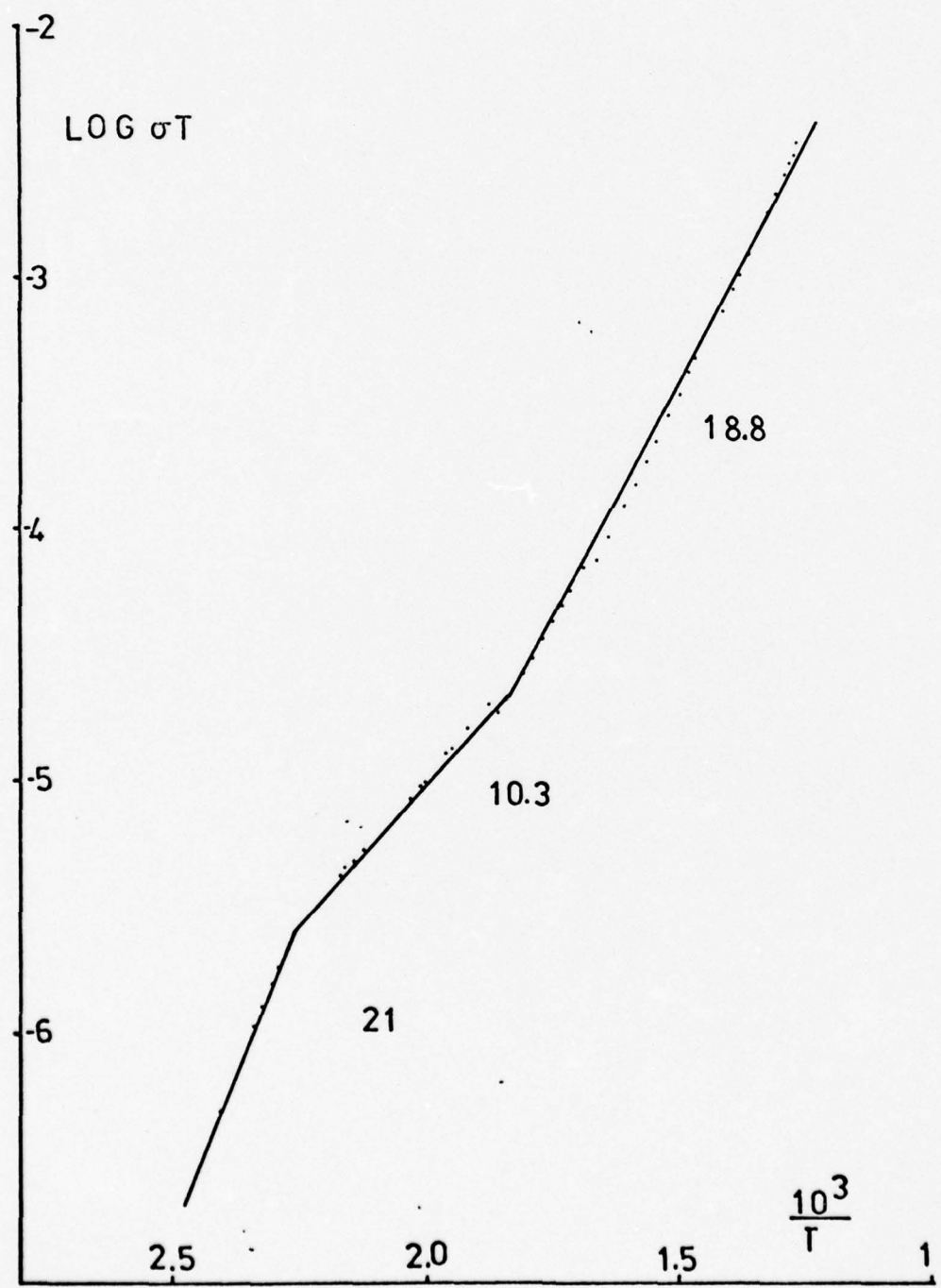


Figure III-2

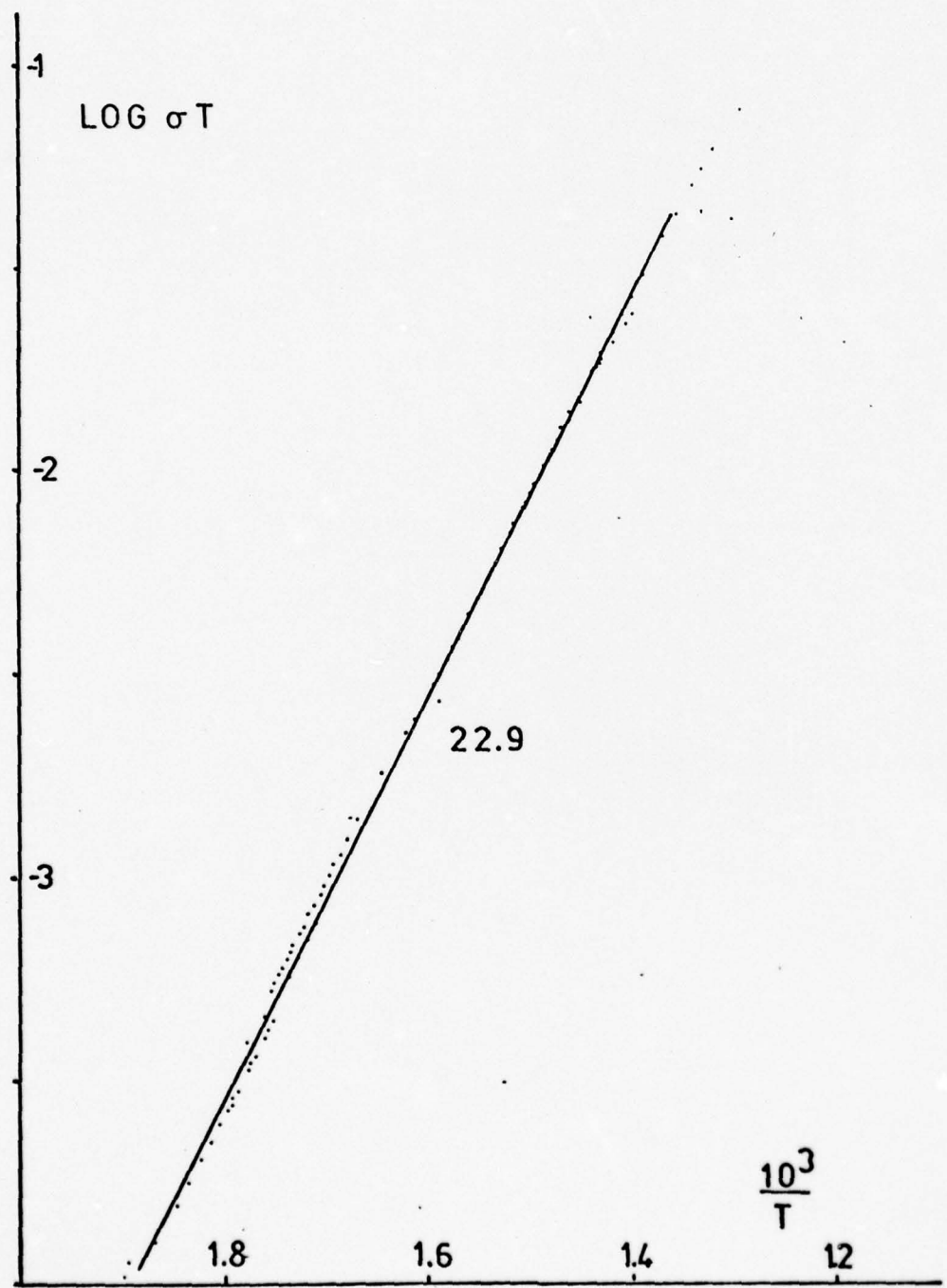


Figure III-3

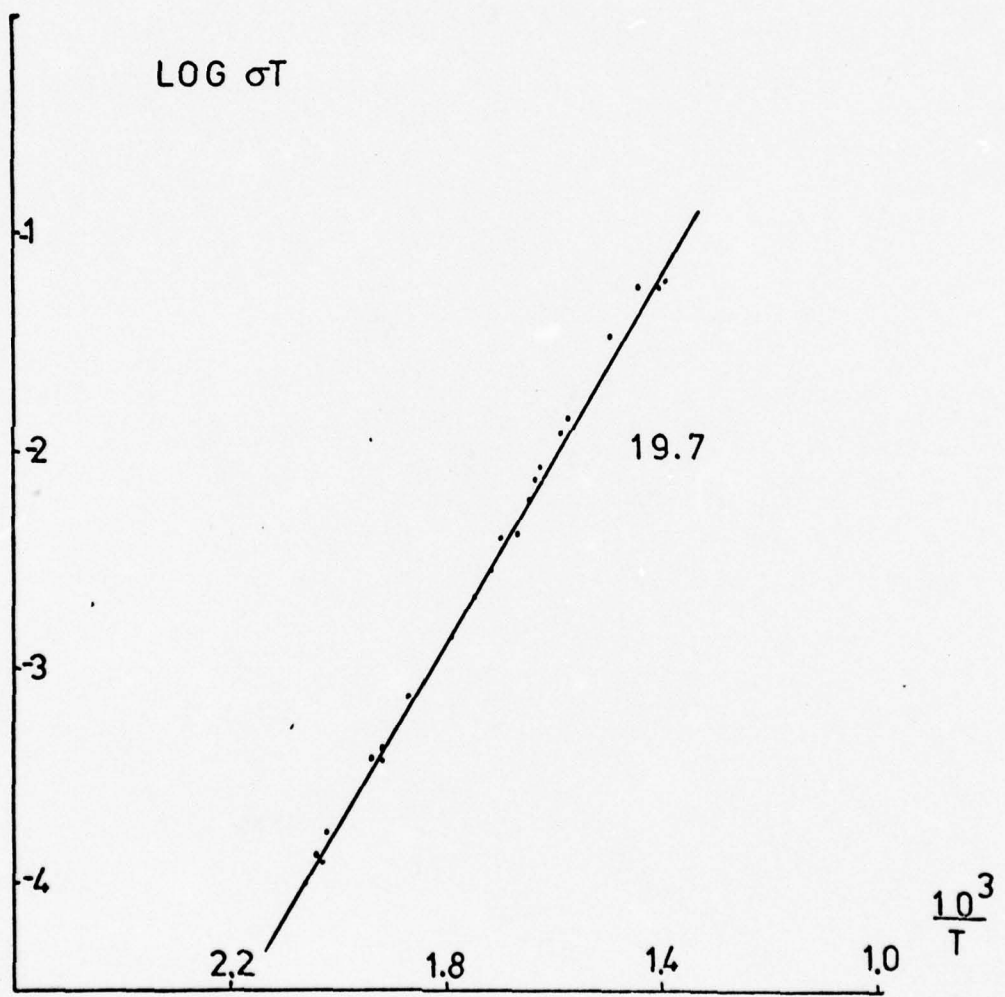


Figure III-4

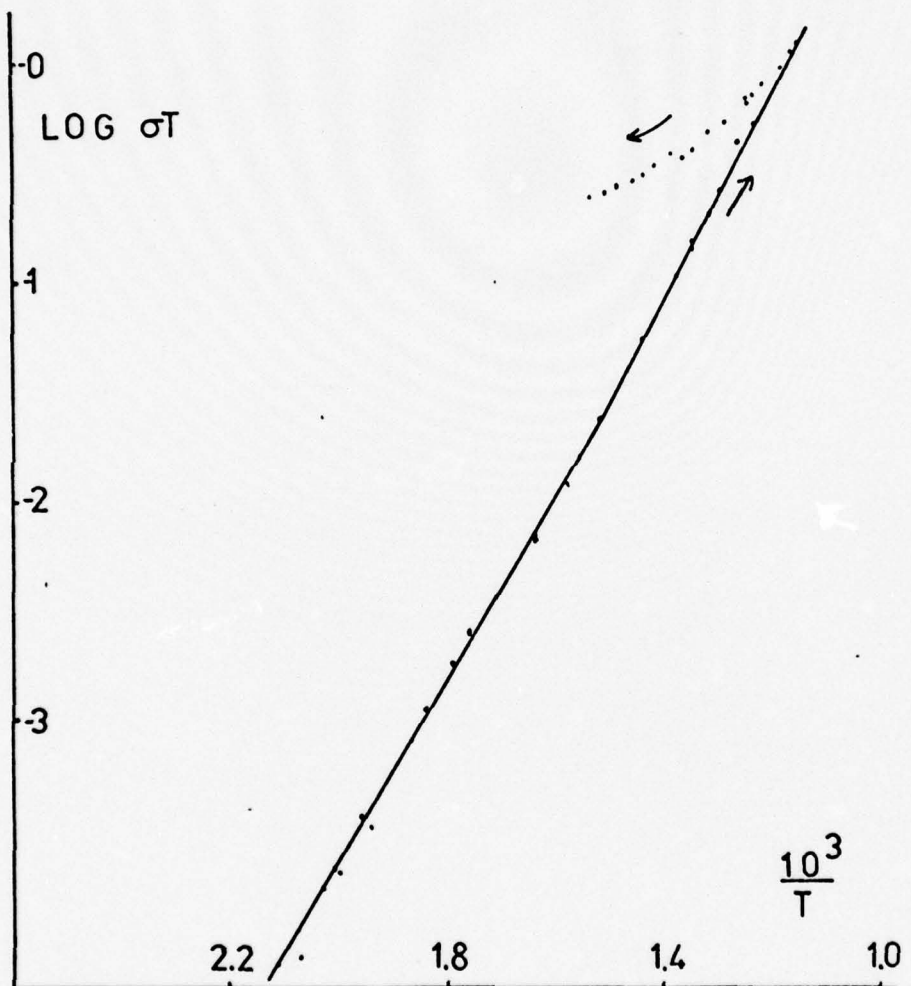


Figure III-5

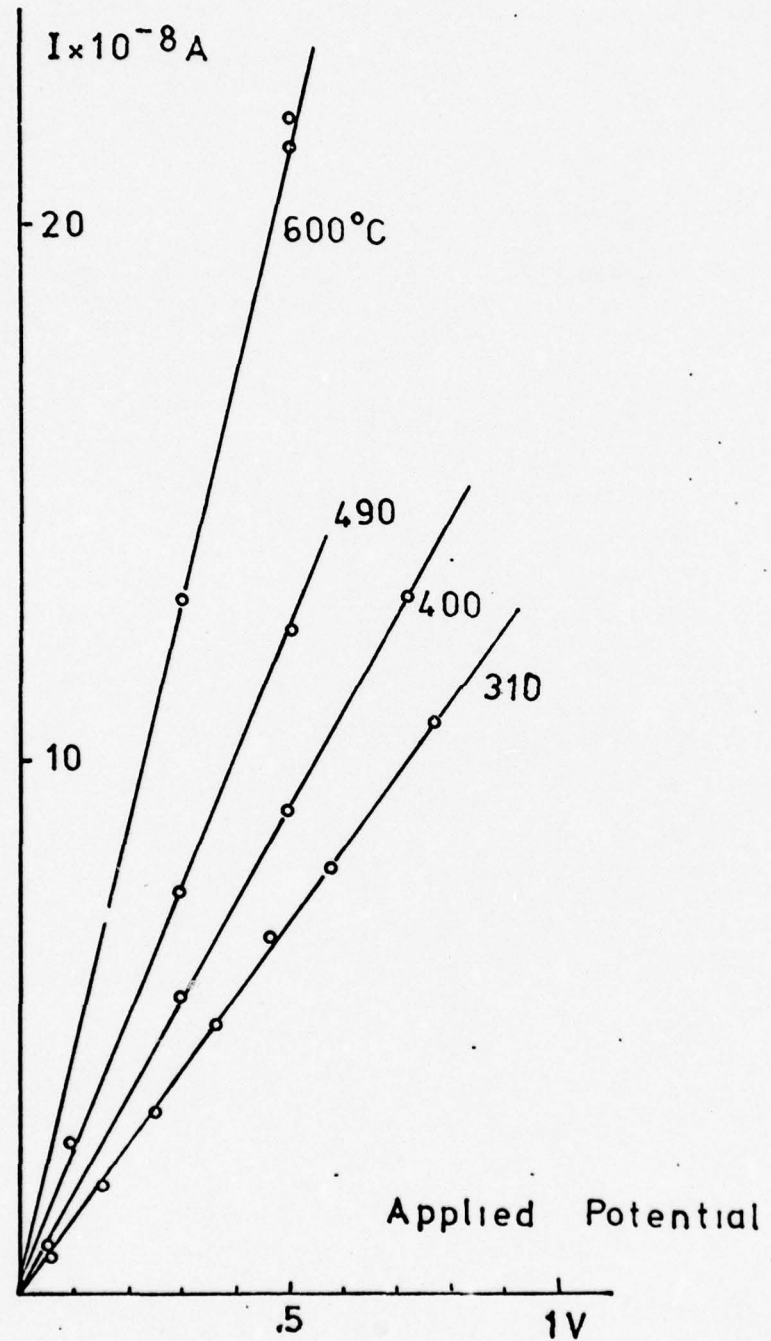


Figure III-6

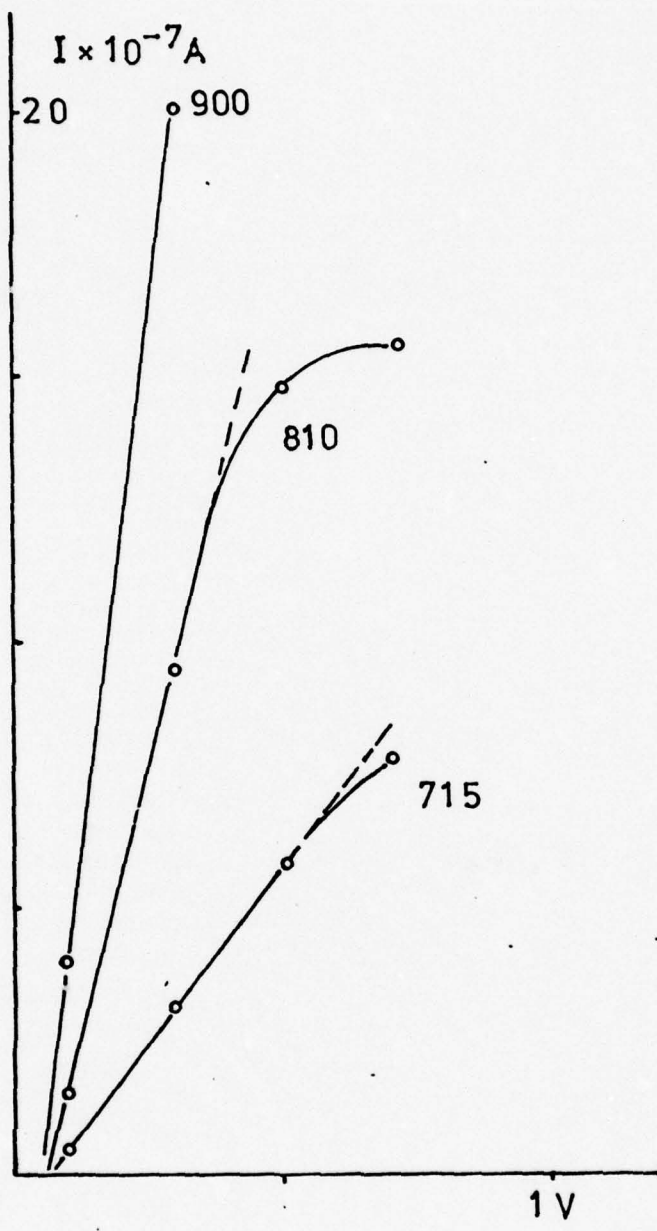


Figure III-7.

LOG σT

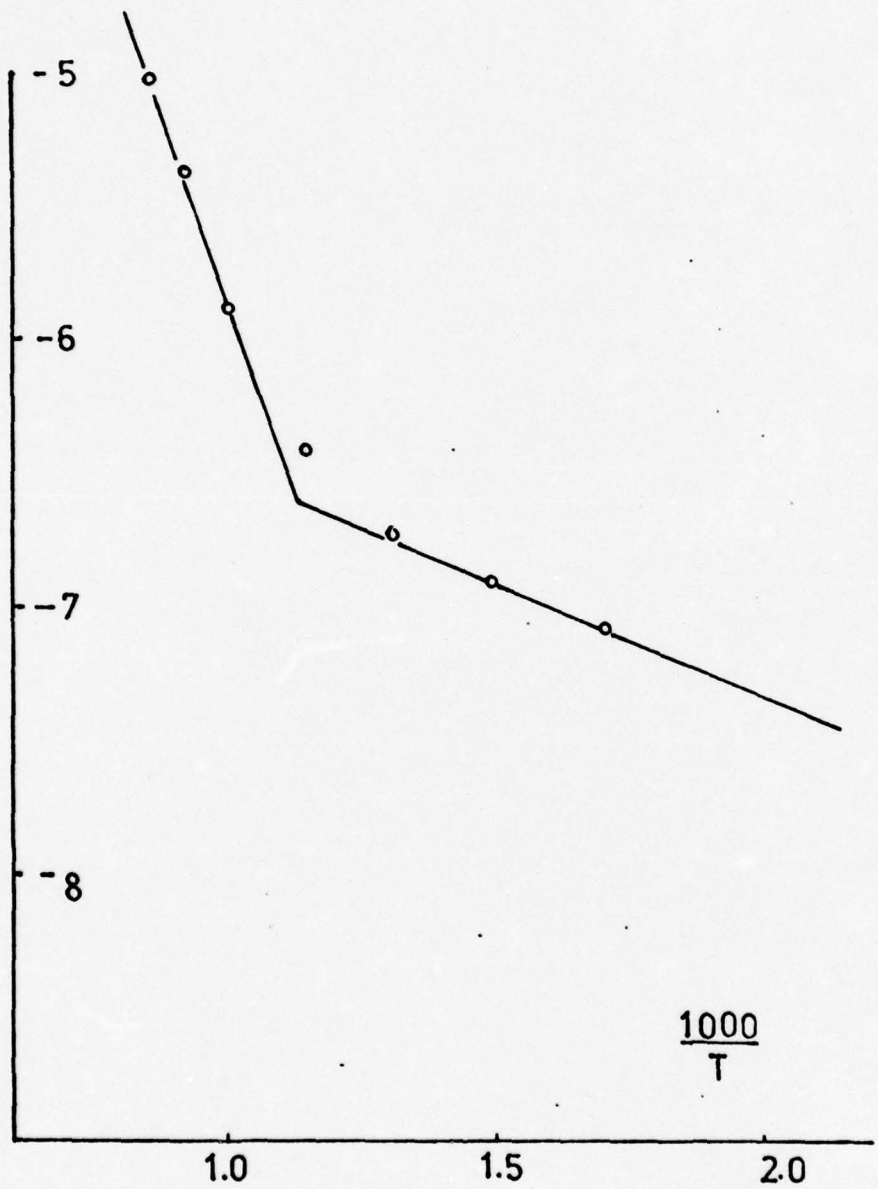


Figure III-8

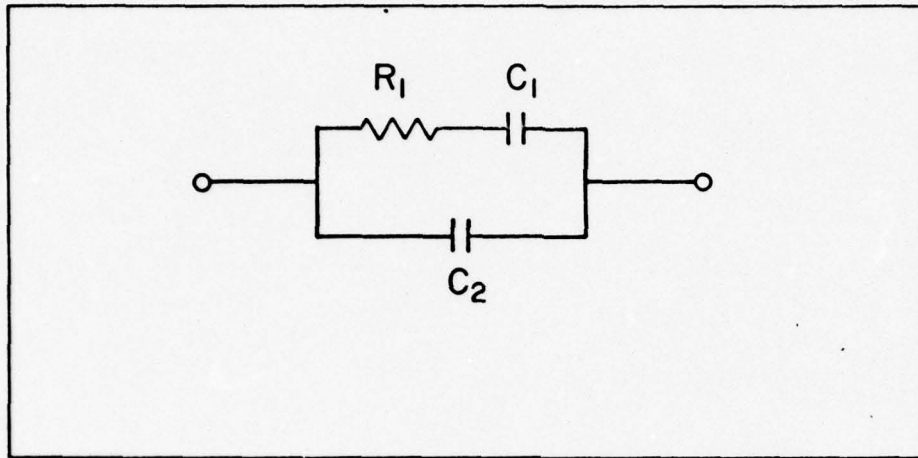


Figure III-9

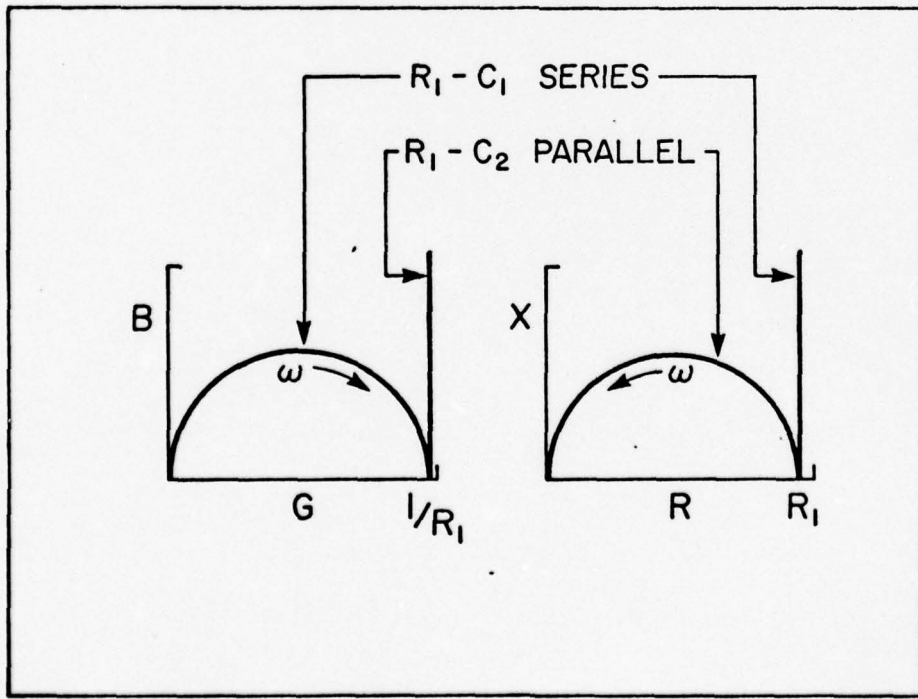


Figure III-10

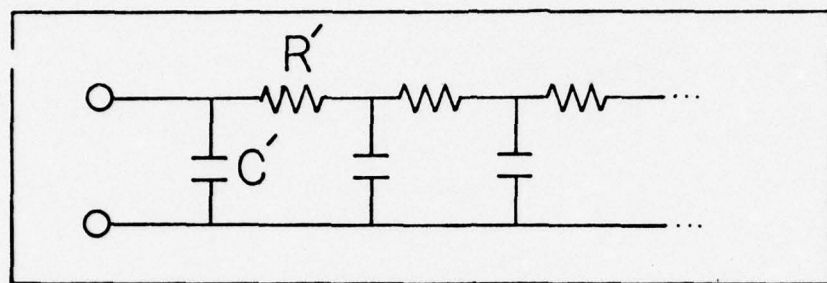


Figure III-11

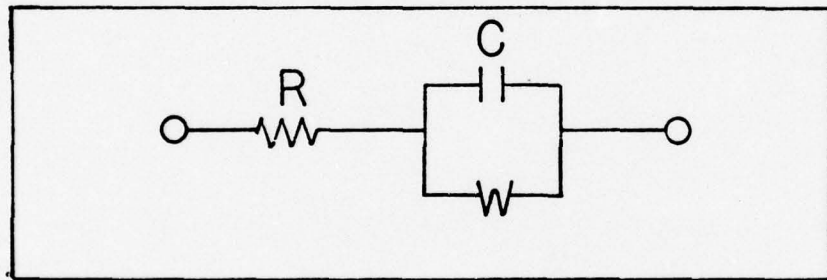


Figure III-12 a

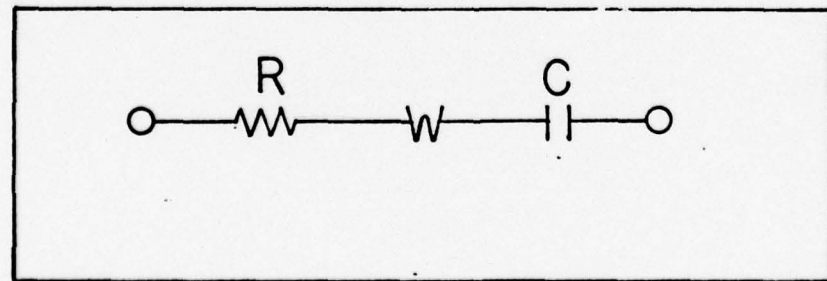


Figure III-12 b

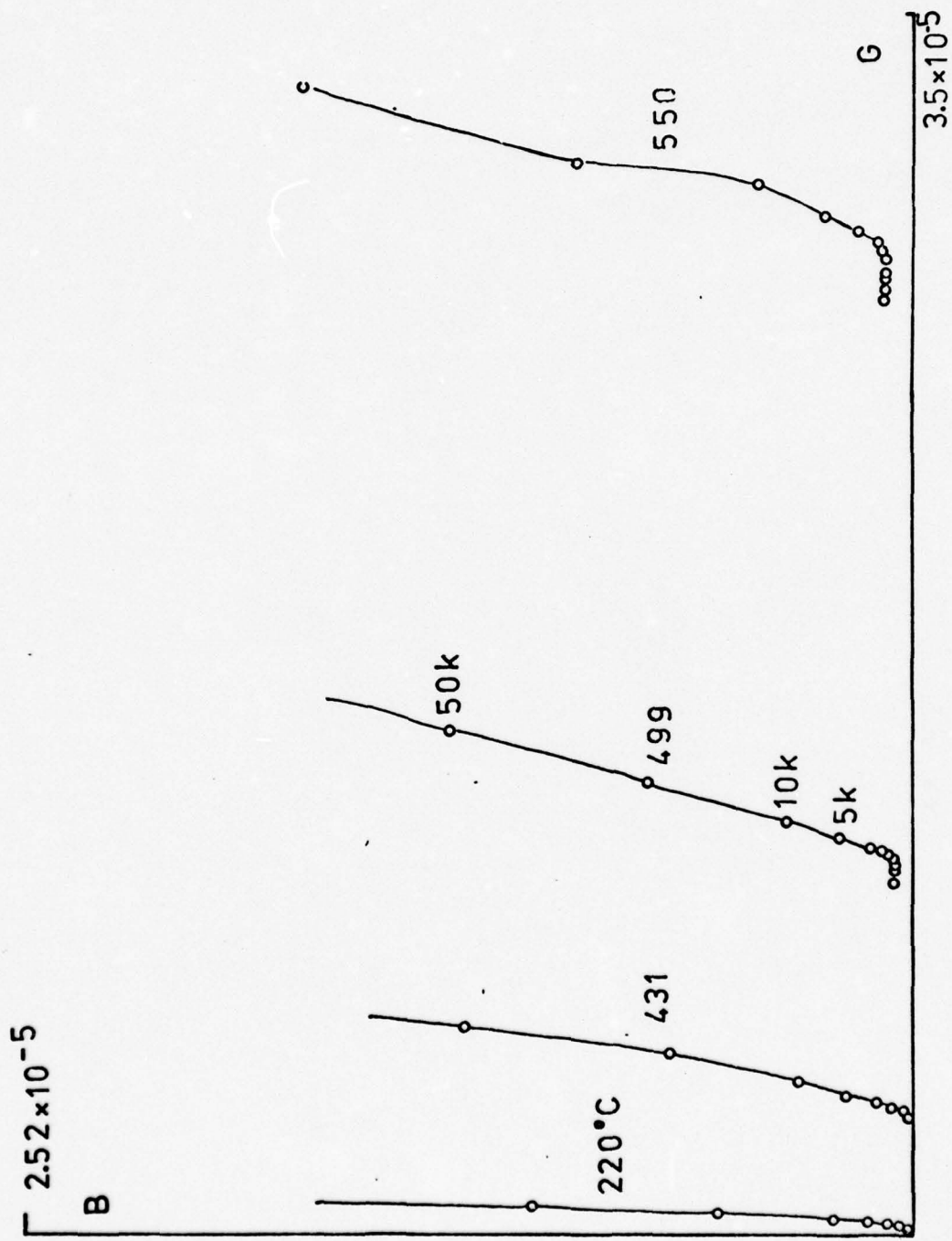


Figure III-13

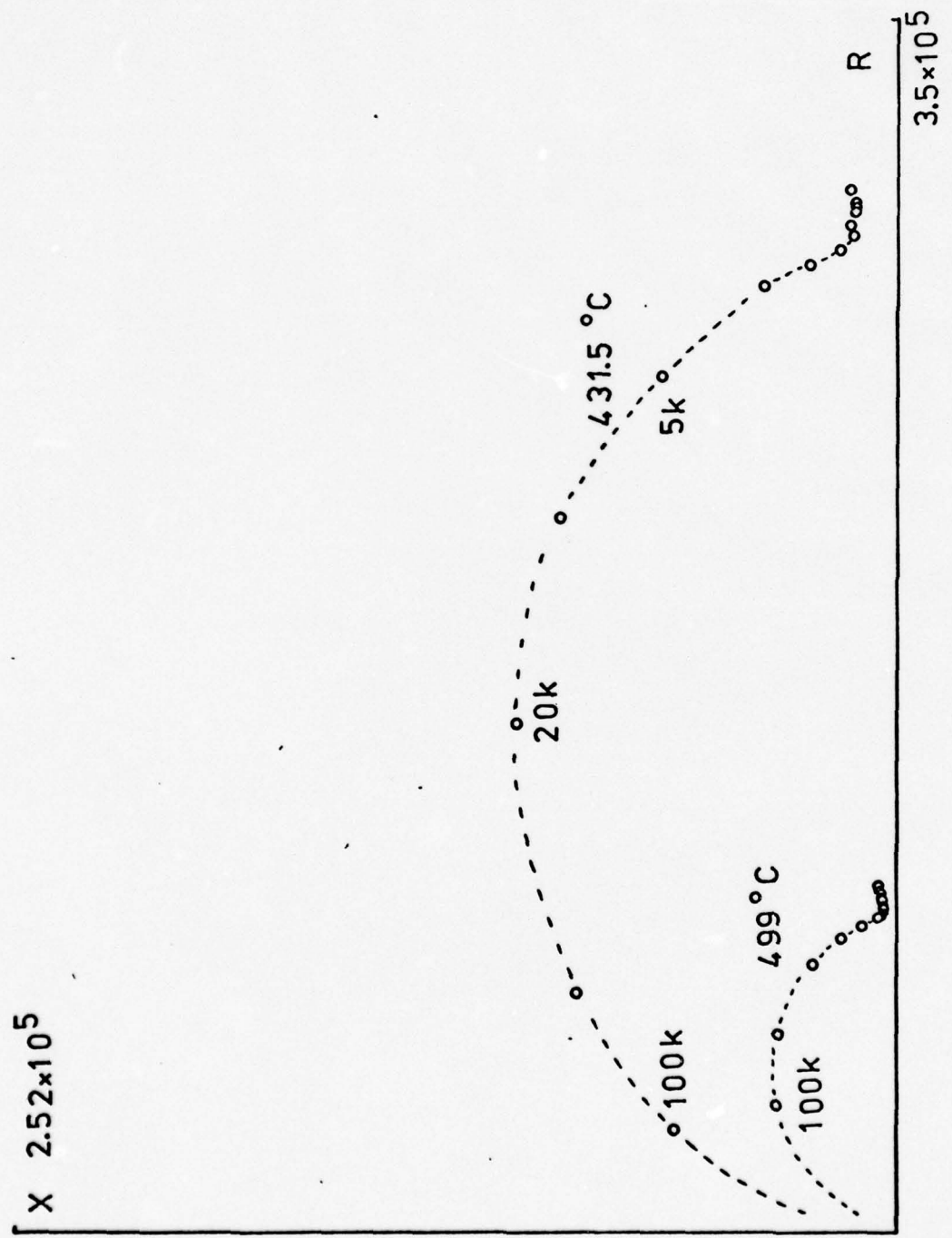


Figure III-14

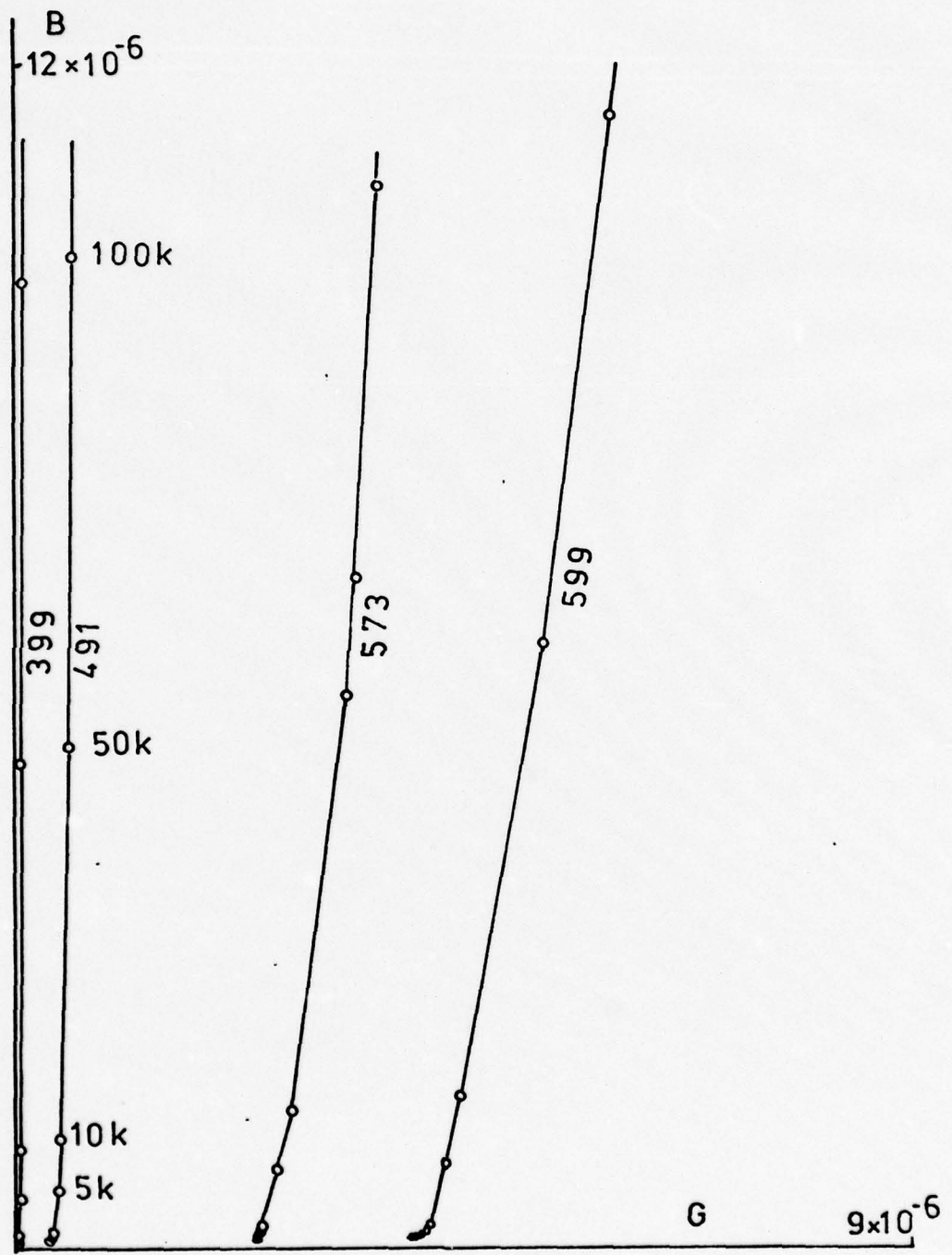


Figure III-15

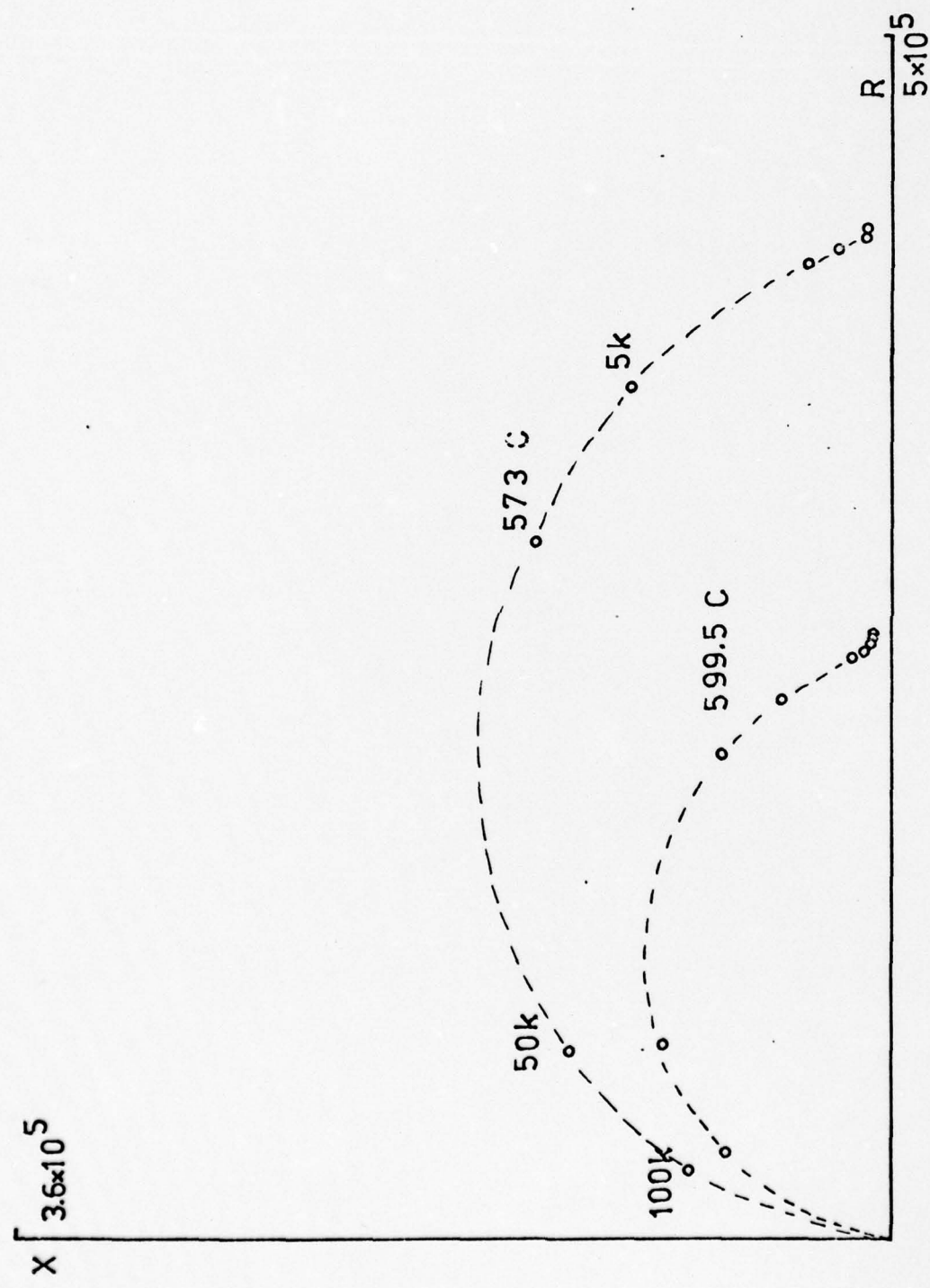


Figure III-16



Figure III-17

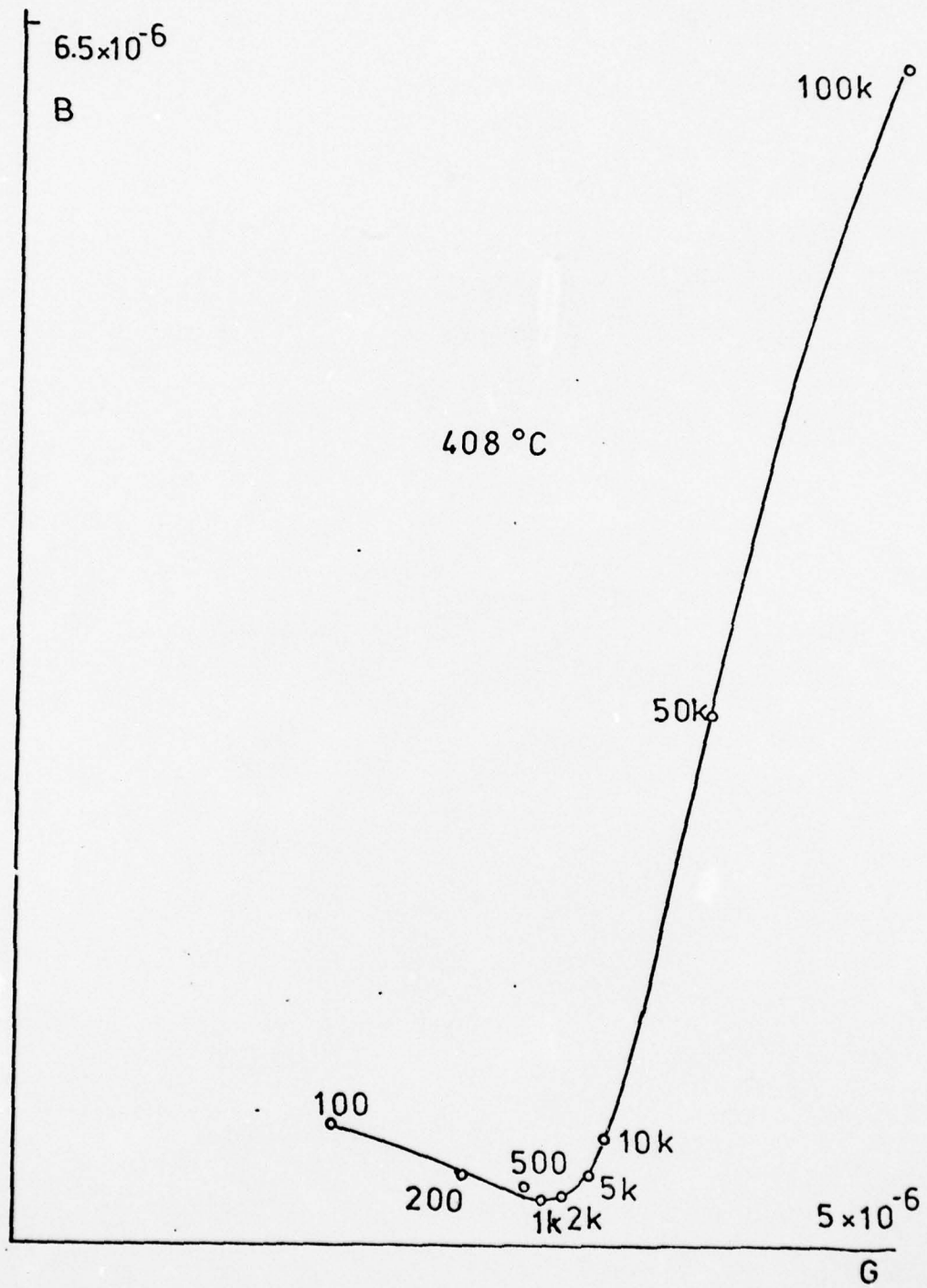


Figure III-18

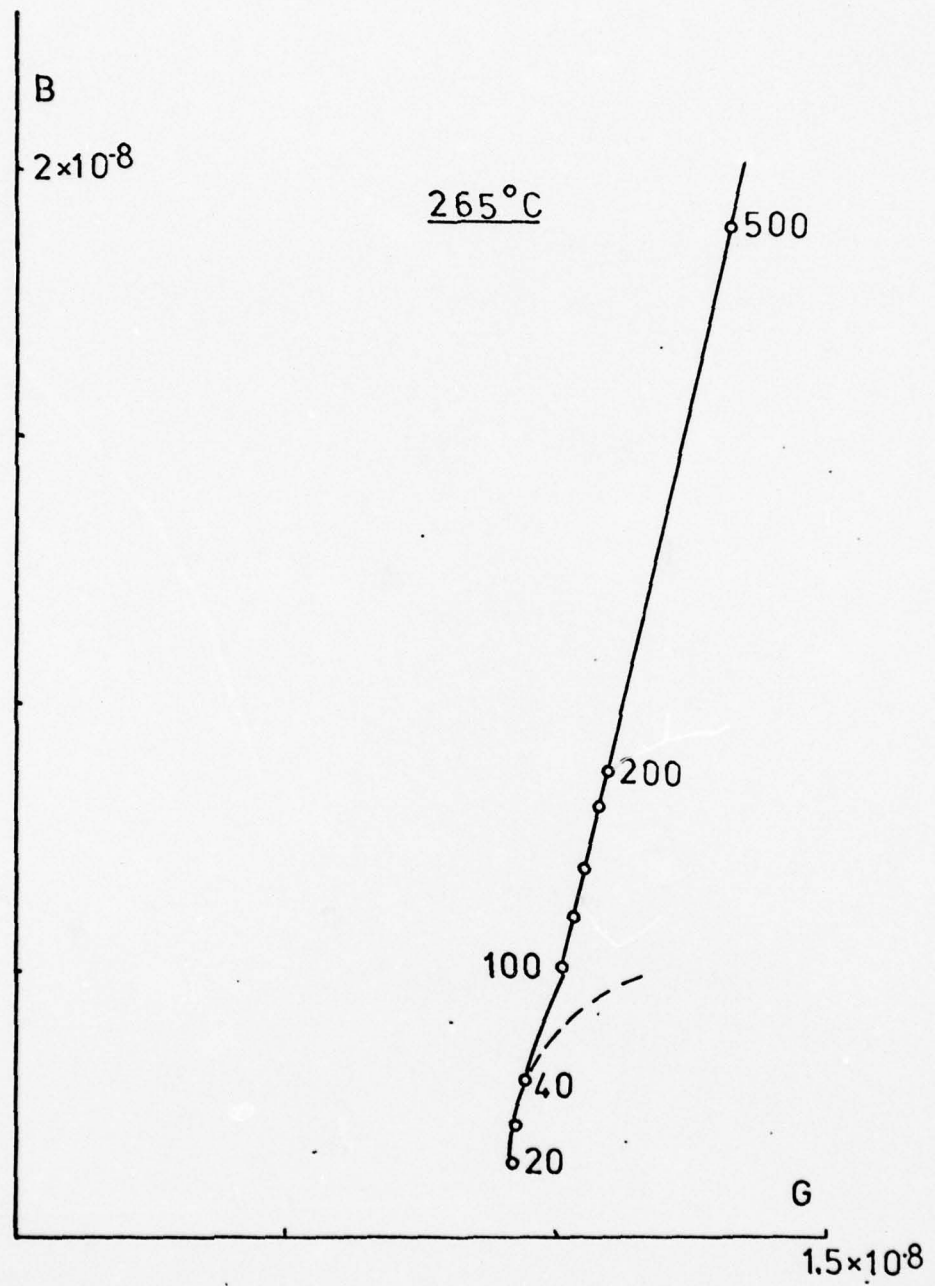


Figure III-19

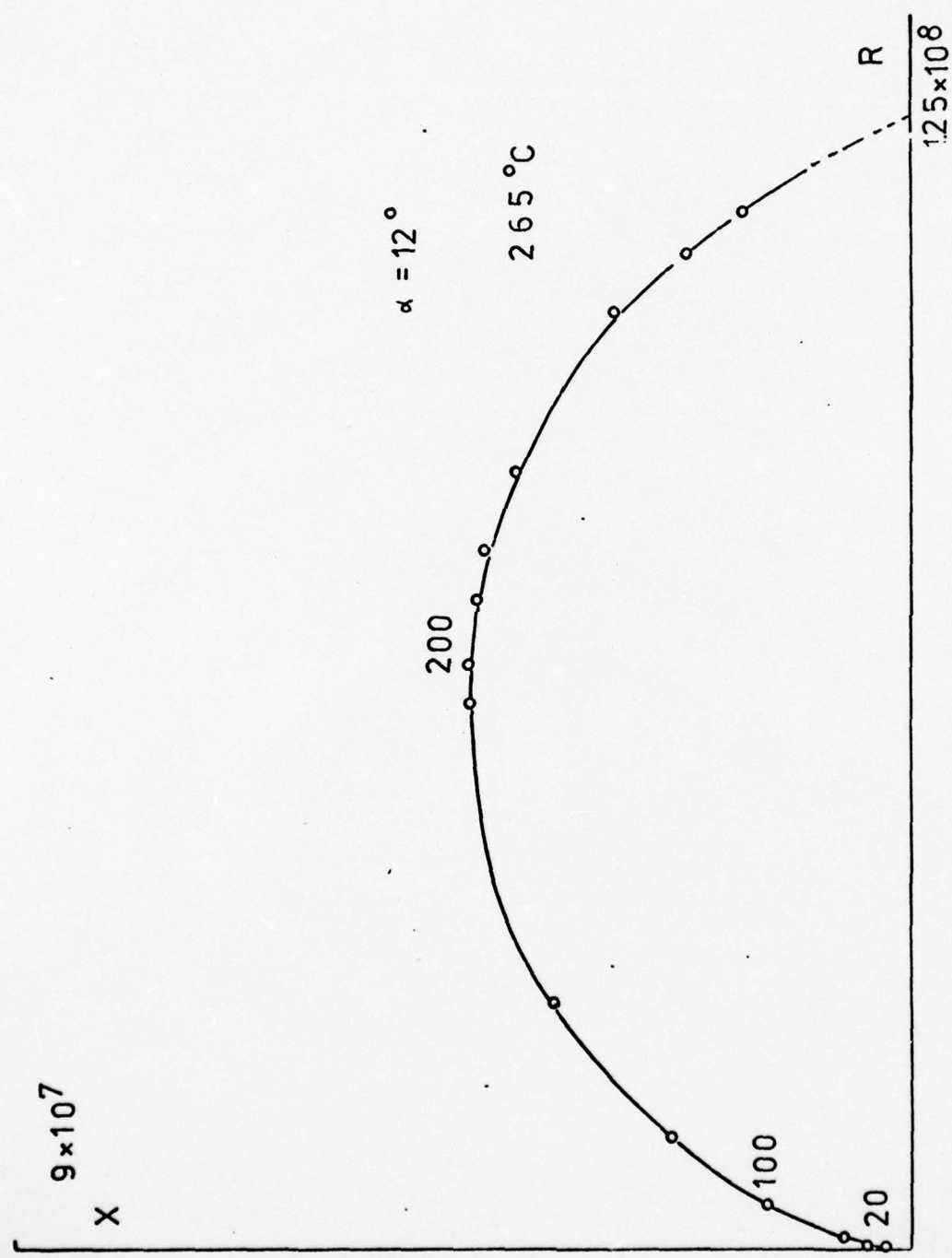


Figure III-20

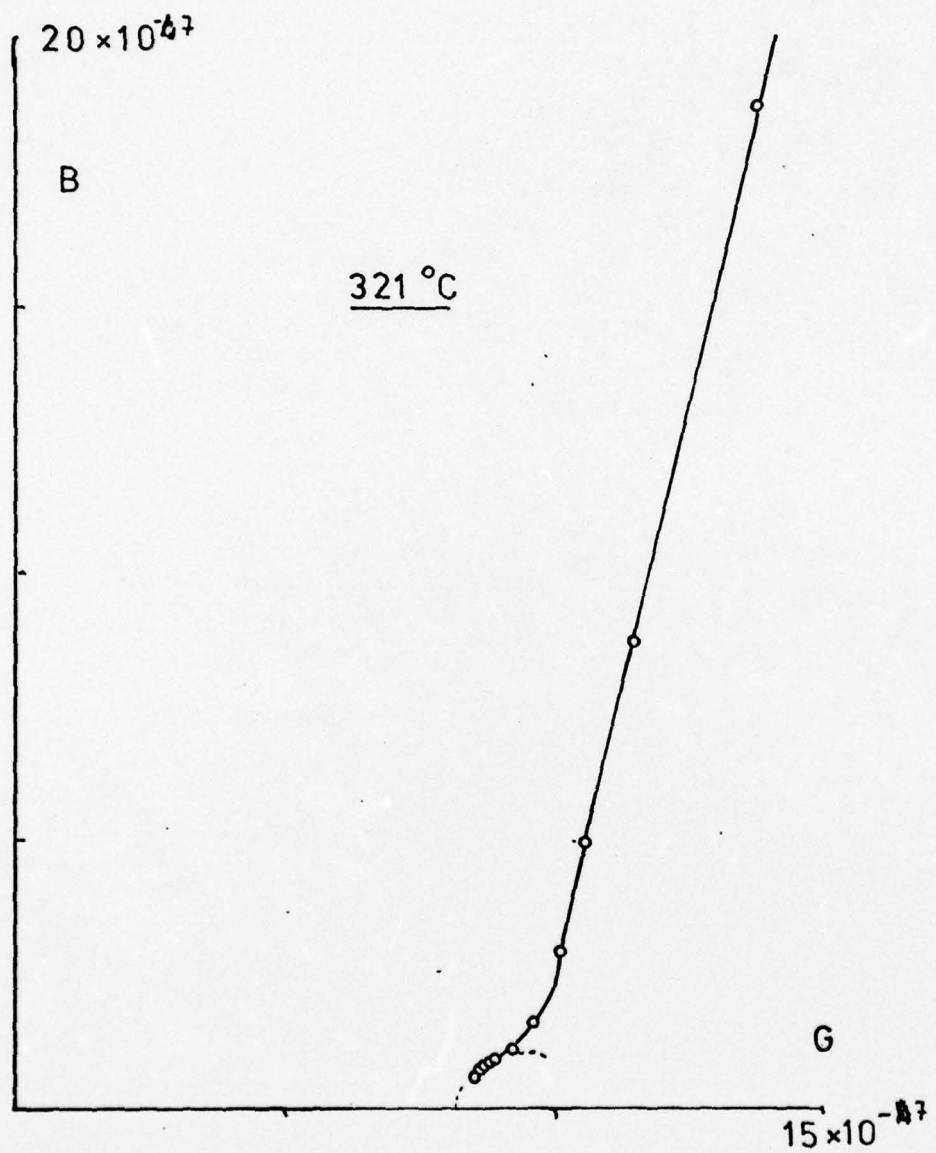


Figure III-21

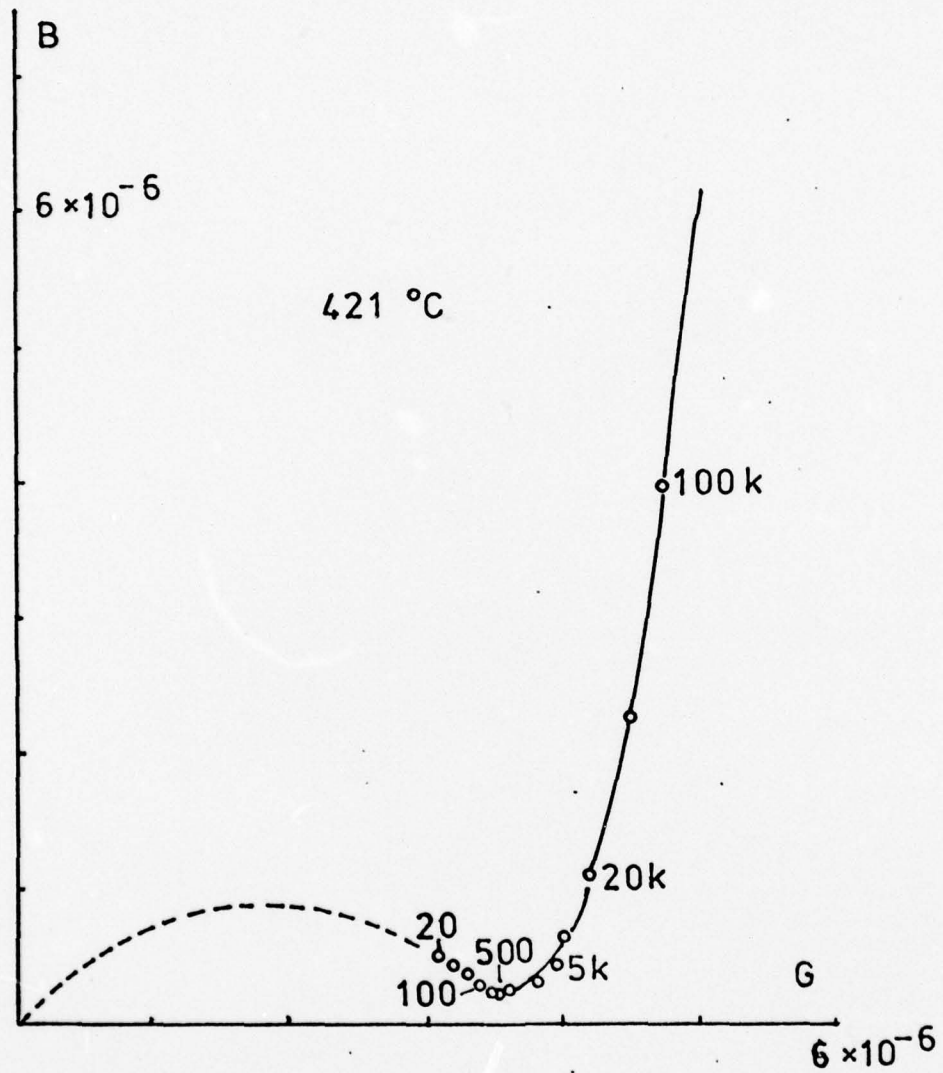


Figure III-22

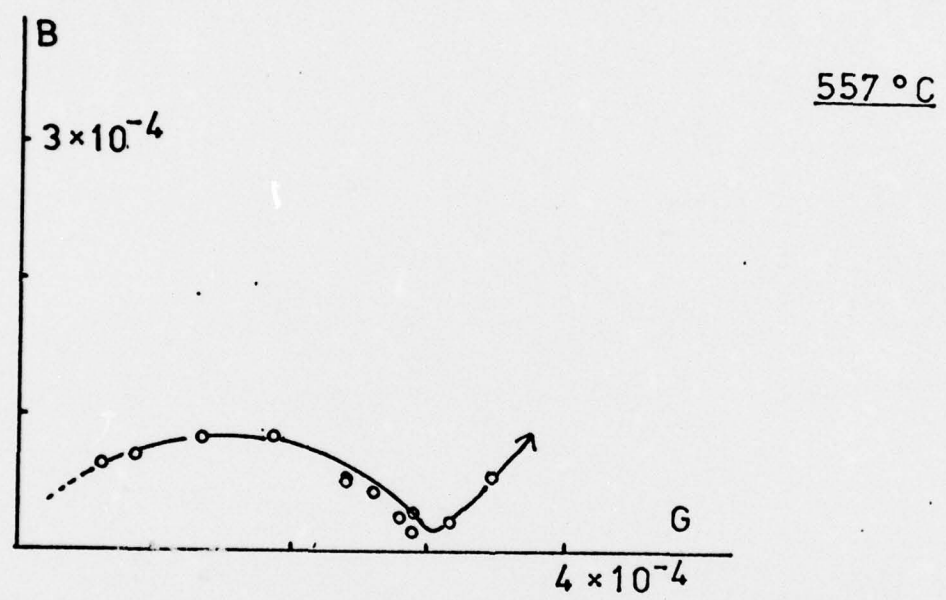


Figure III-23

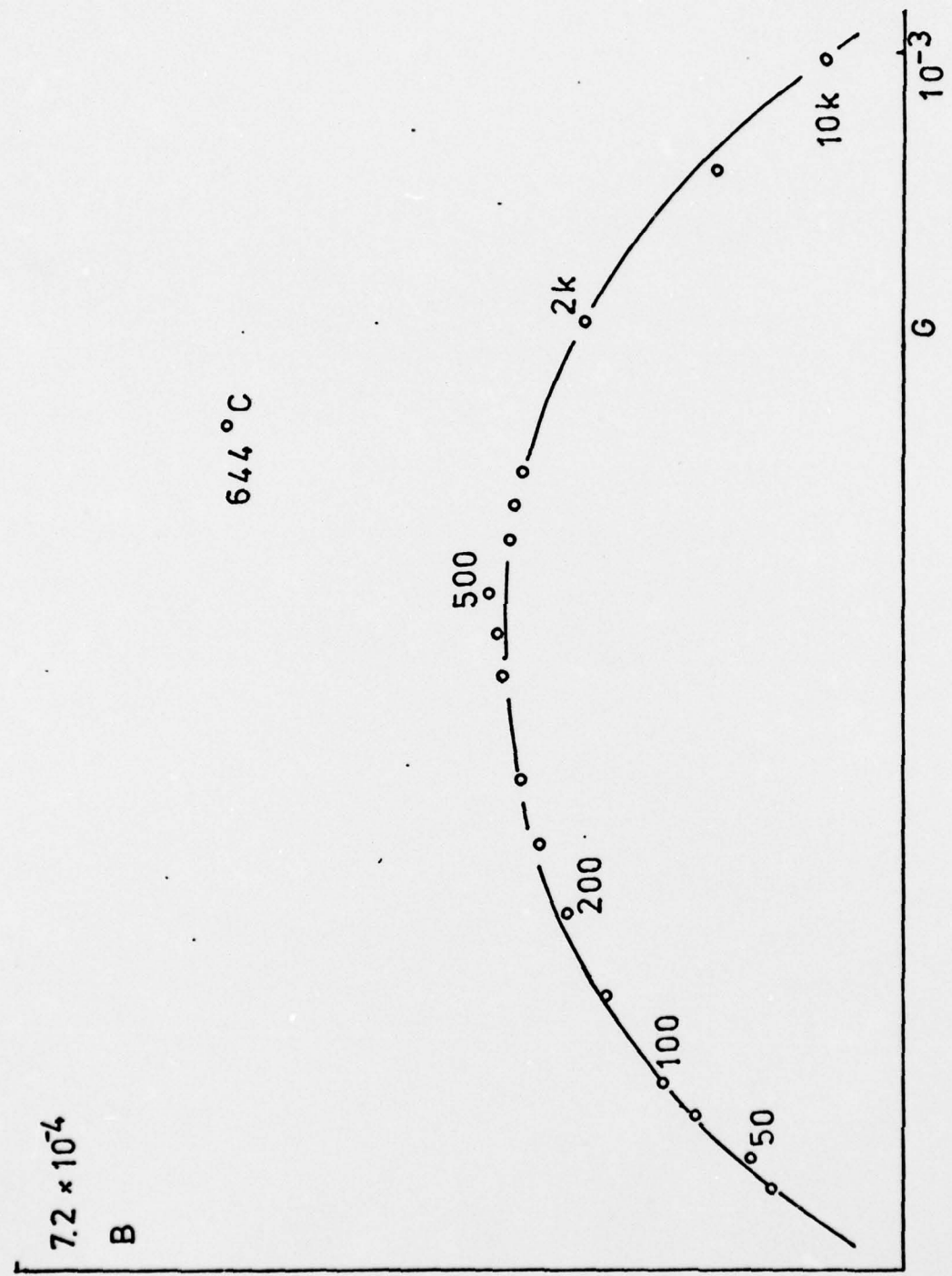


Figure III-24

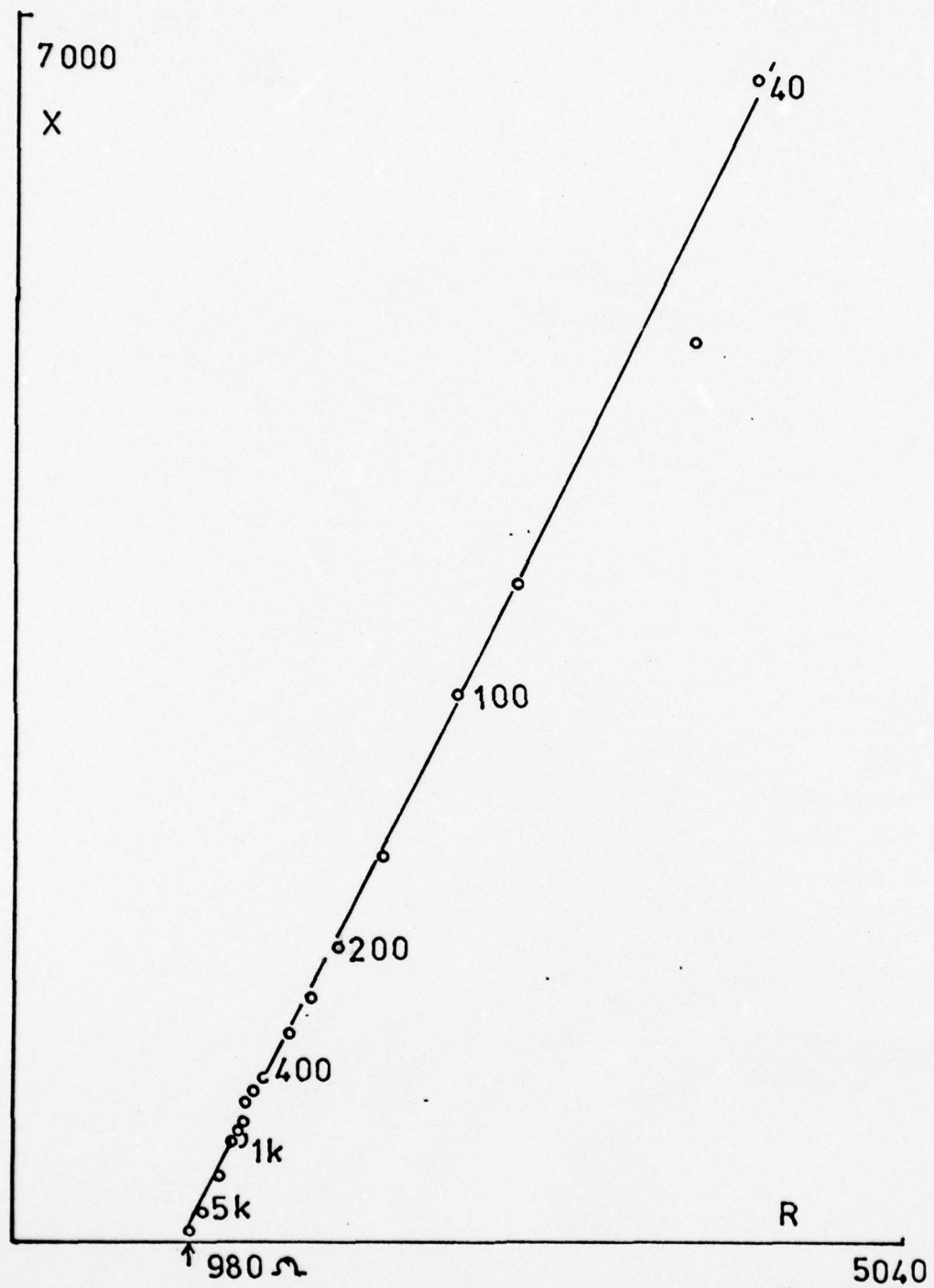


Figure III-25

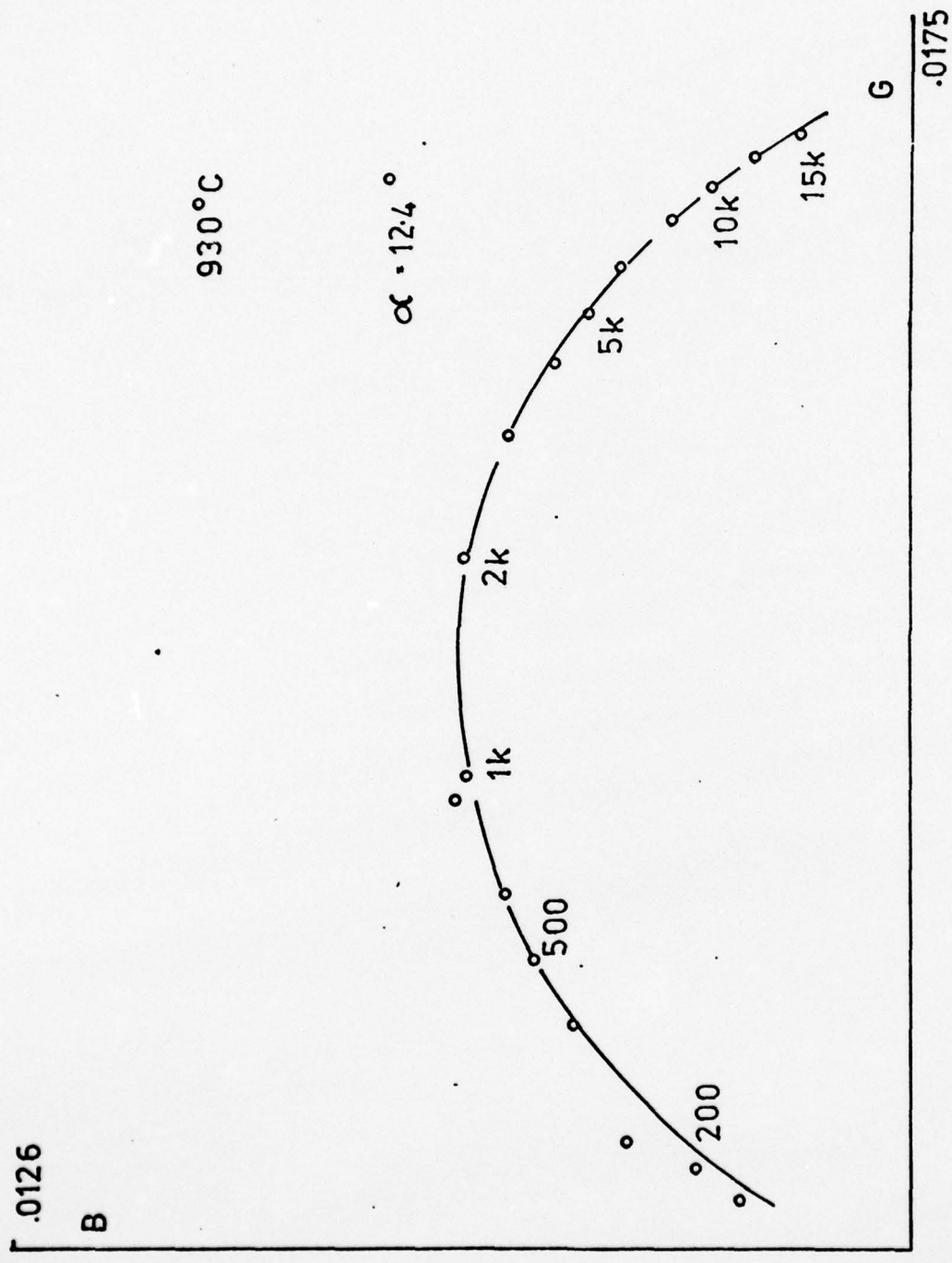


Figure III-26

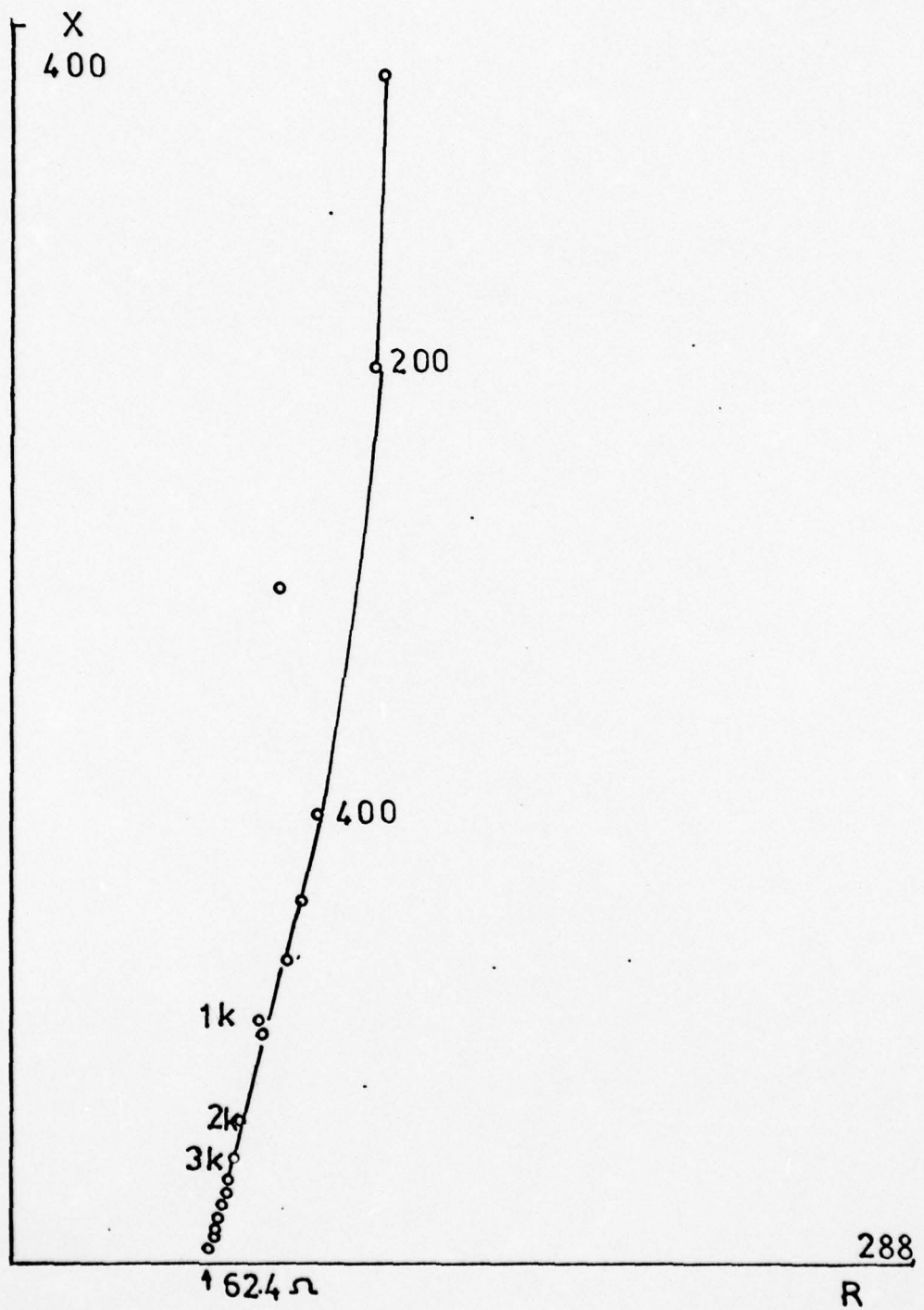


Figure III-27

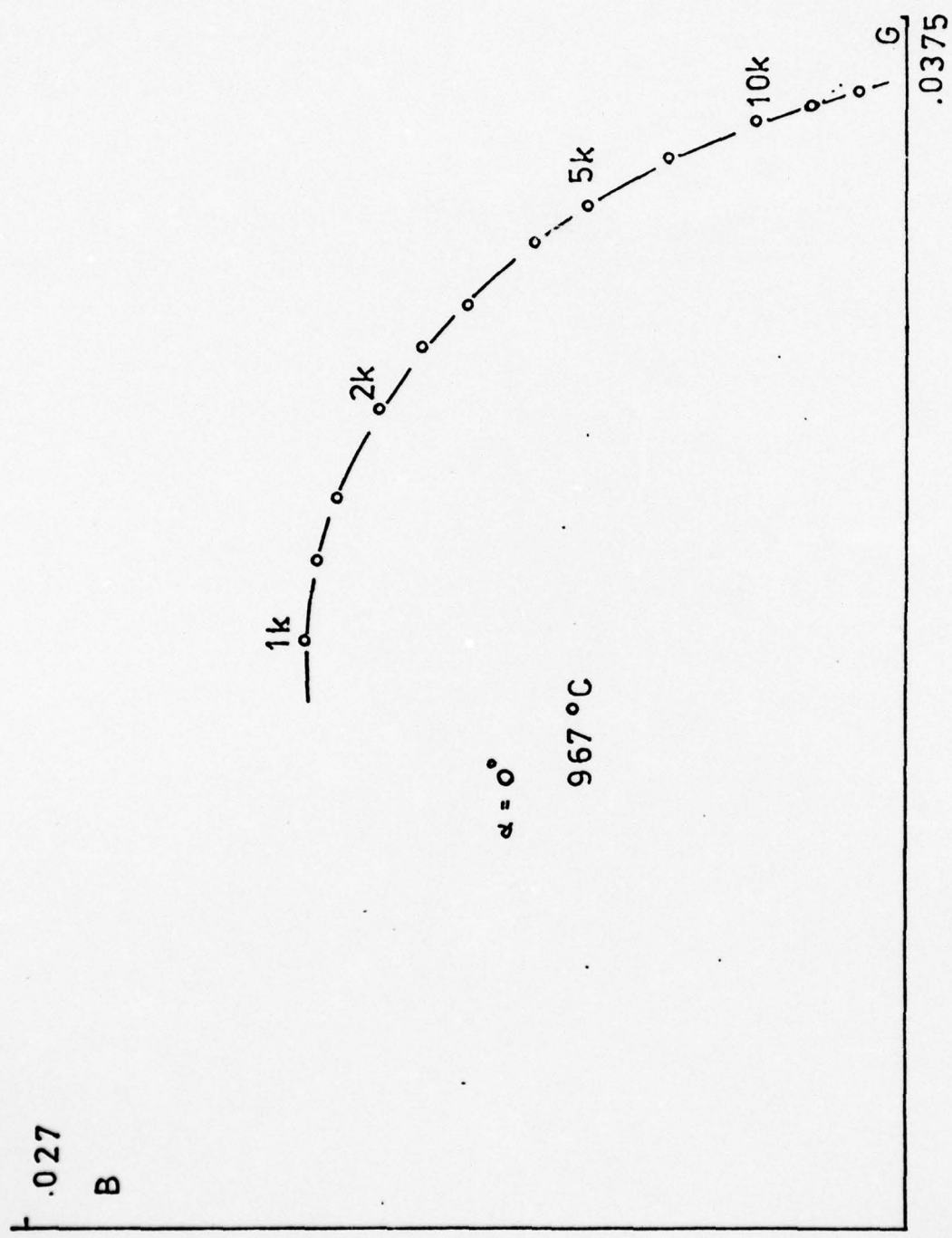


Figure III-28

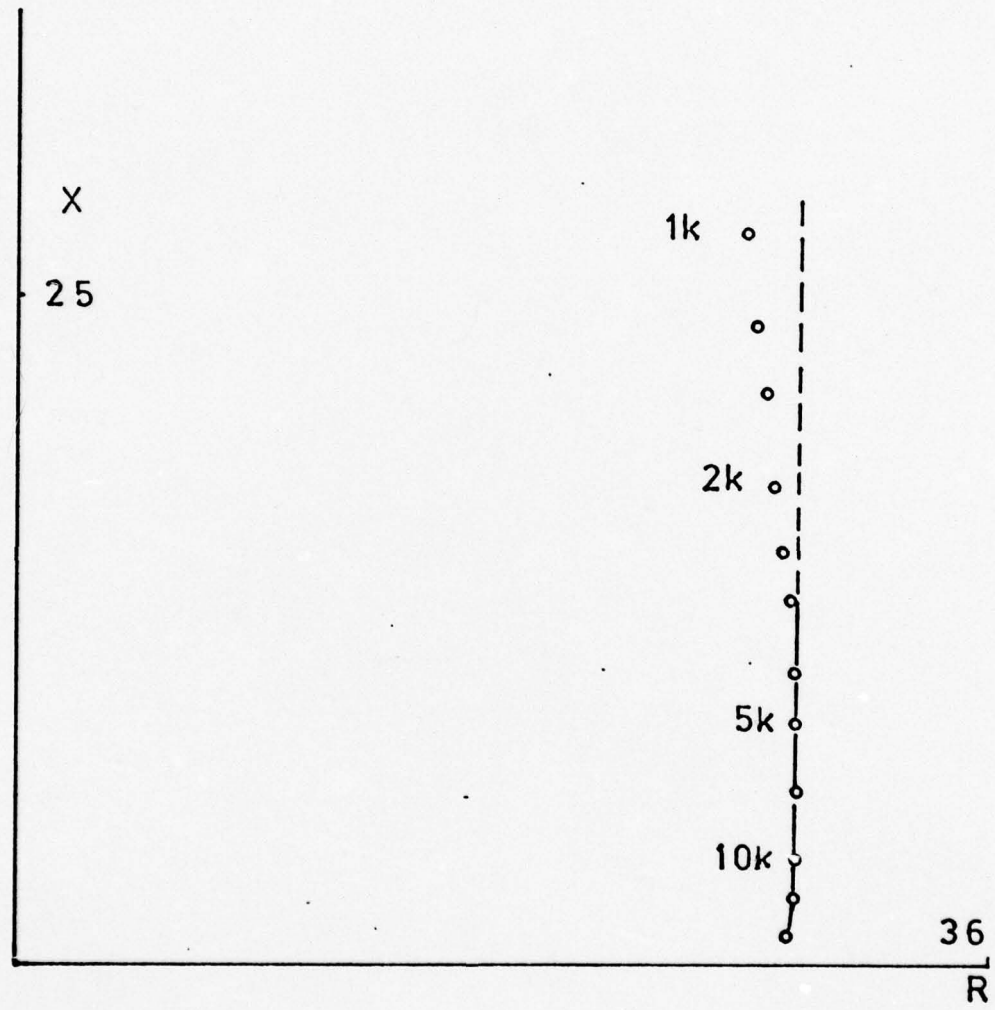


Figure III-29

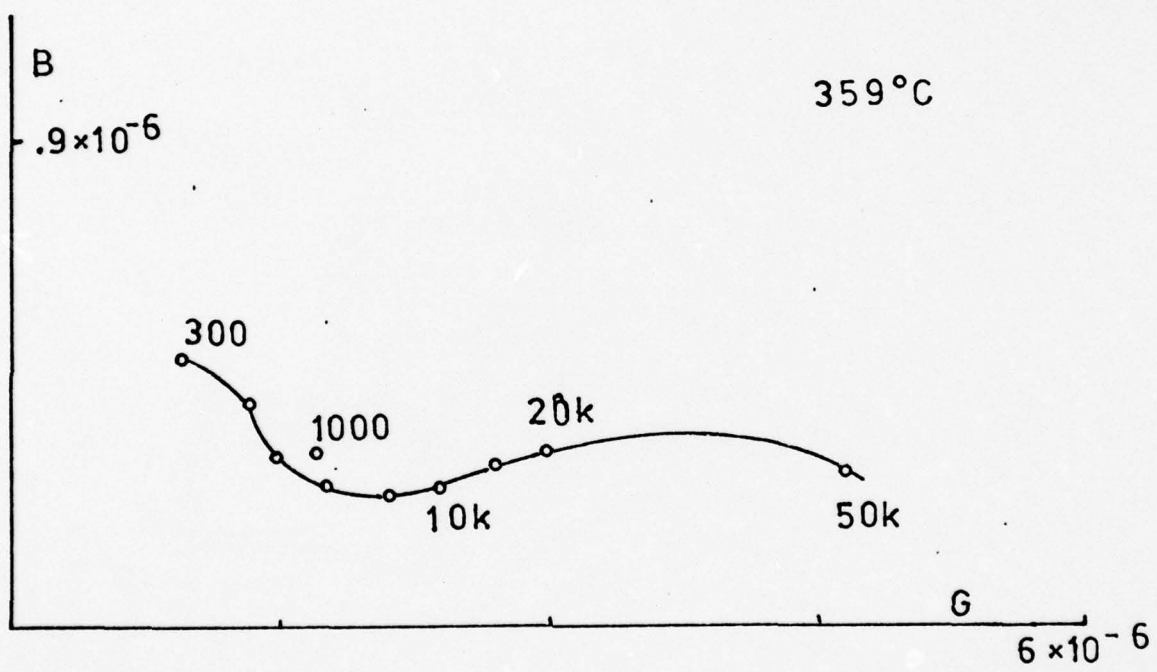


Figure III-30

AD-A039 899

STANFORD UNIV CALIF CENTER FOR MATERIALS RESEARCH
SOLID ELECTROLYTE BATTERY MATERIALS.(U)
NOV 74 R A HUGGINS

UNCLASSIFIED

CMR-74-16

F/G 10/2

N00014-67-A-0112-0075
NL

2 of 2
ADA039 899



END

DATE
FILMED
6 - 77

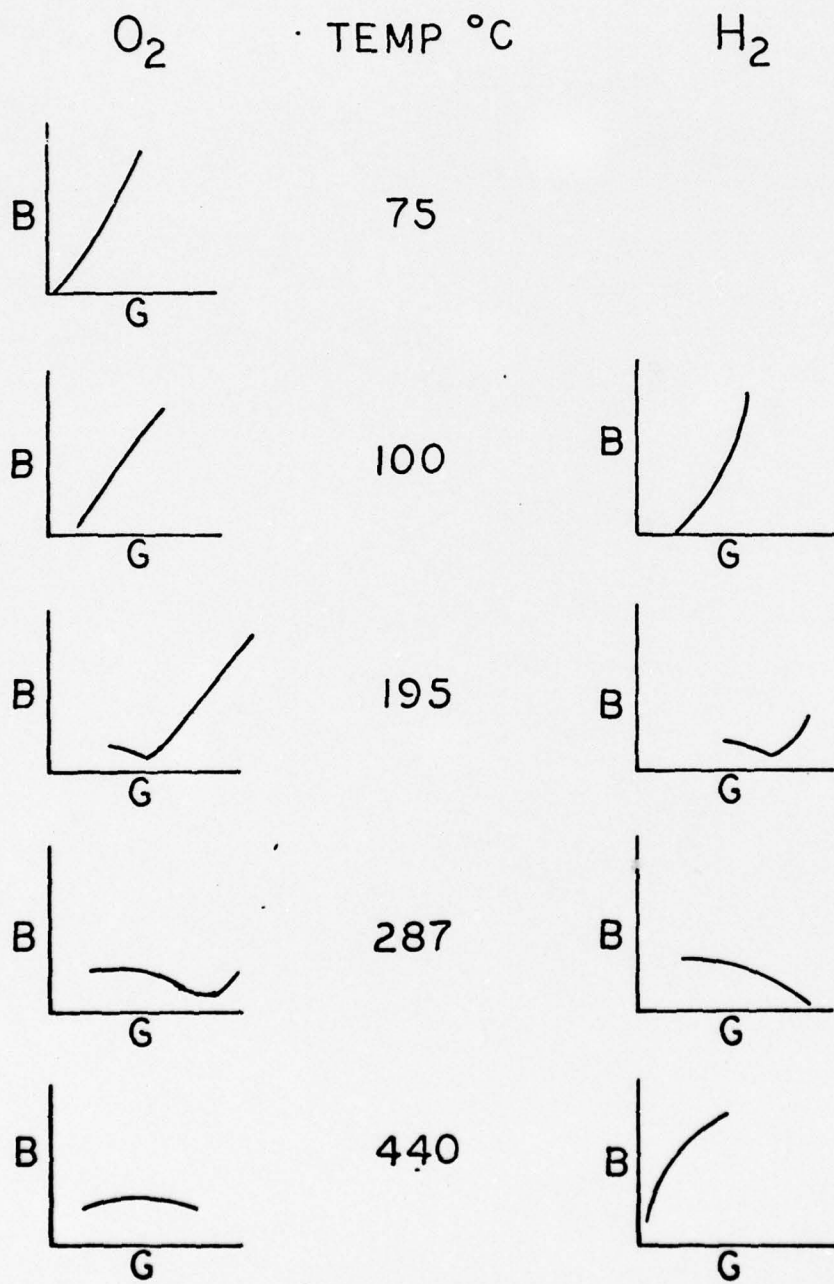


Figure III-31

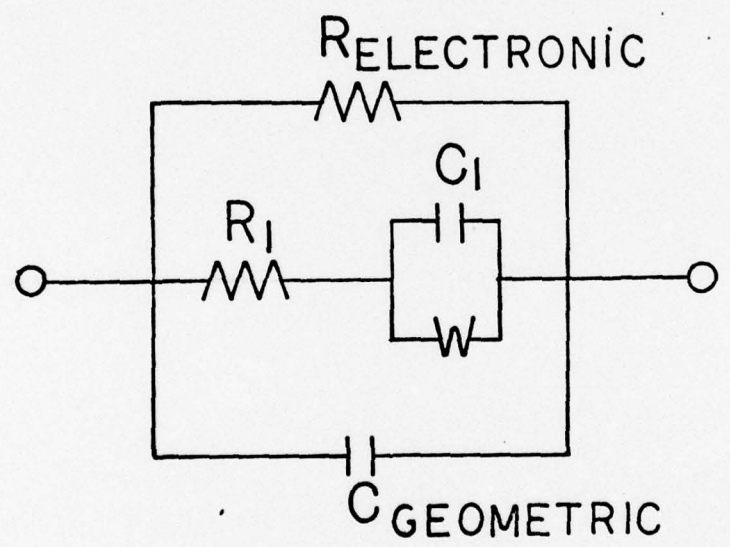


Figure III-32

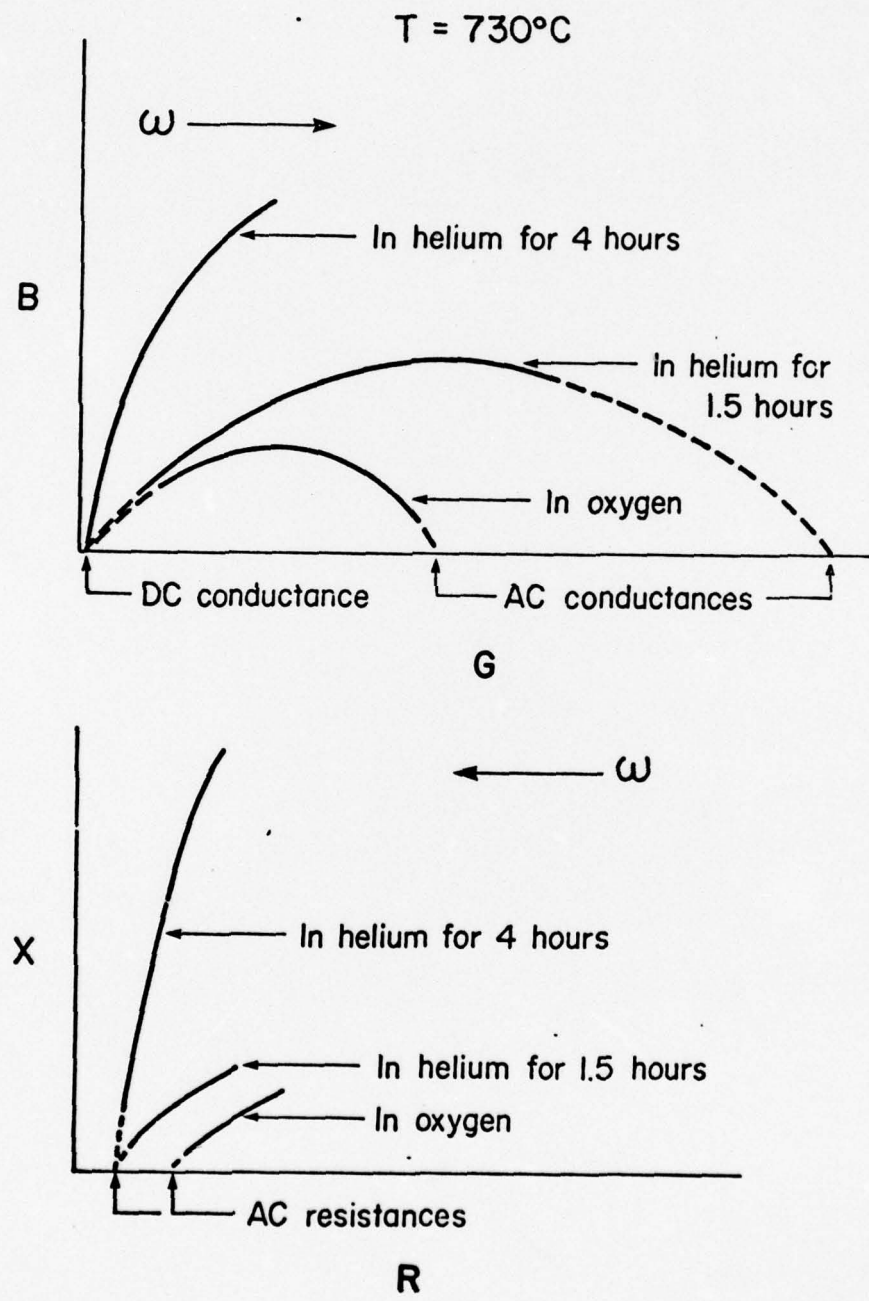
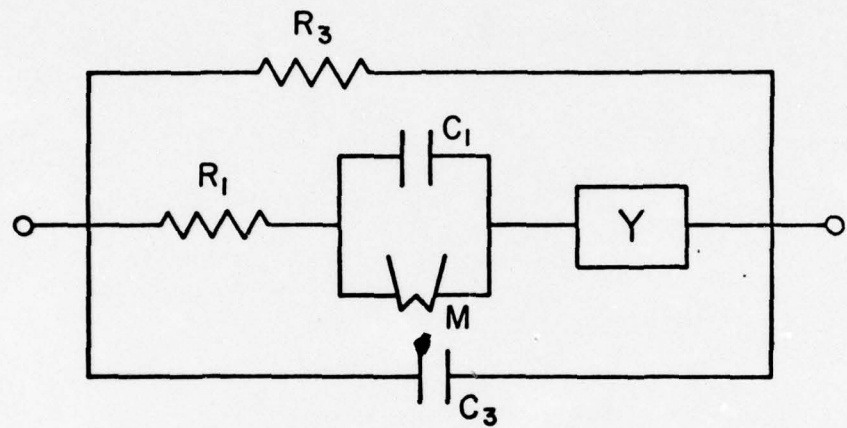


Figure III-33

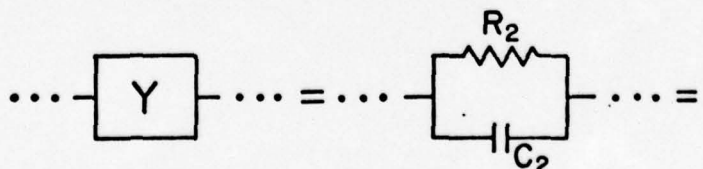


R_3 = ELECTRONIC RESISTANCE

C_3 = GEOMETRIC CAPACITANCE

R_1 = IONIC RESISTANCE

C_1 = DOUBLE LAYER CAPACITANCE



GRAIN BOUNDARY DIFFUSION

Figure III-34

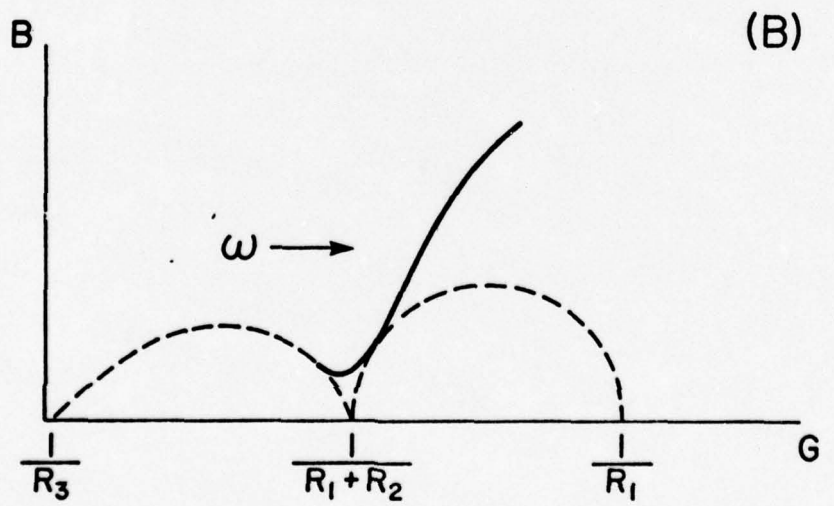
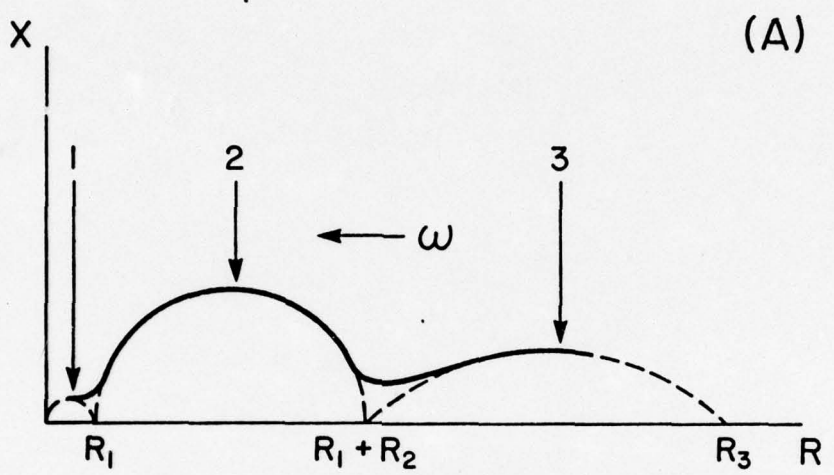


Figure III-35

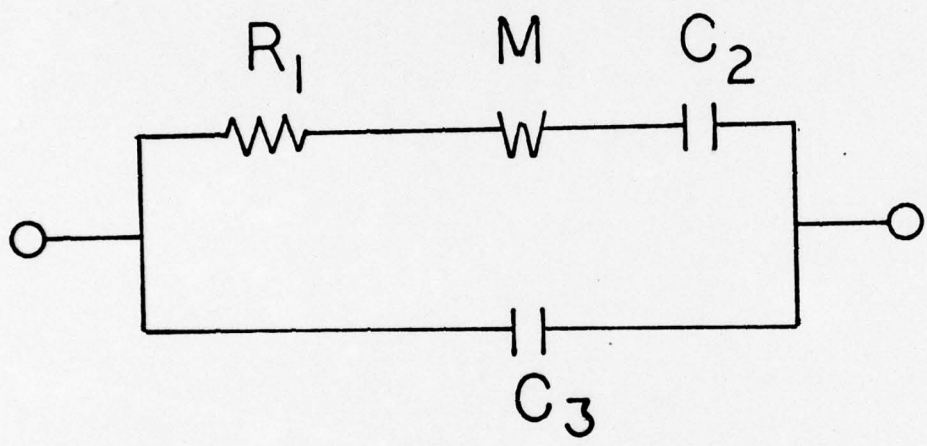


Figure III-36

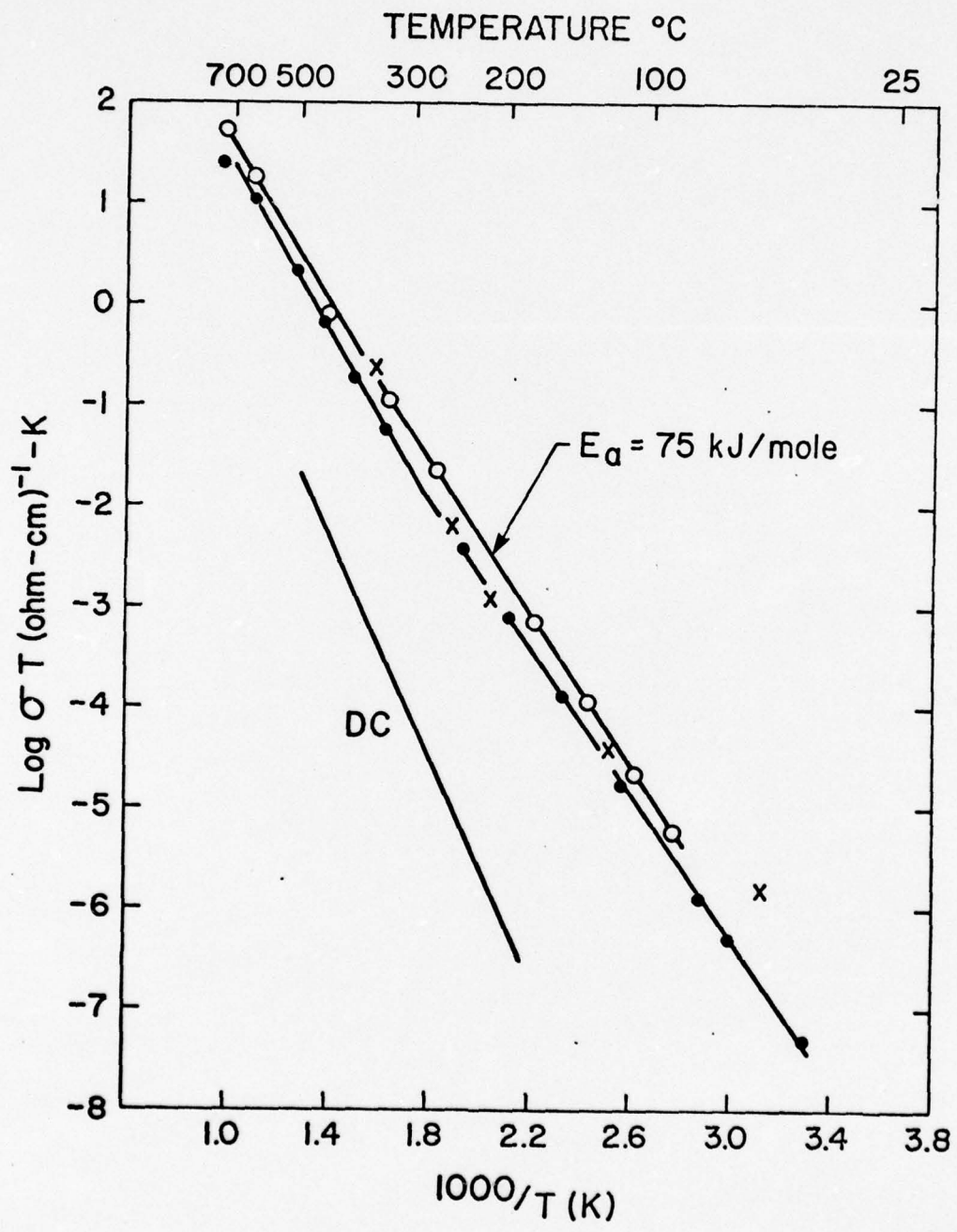


Figure III-37

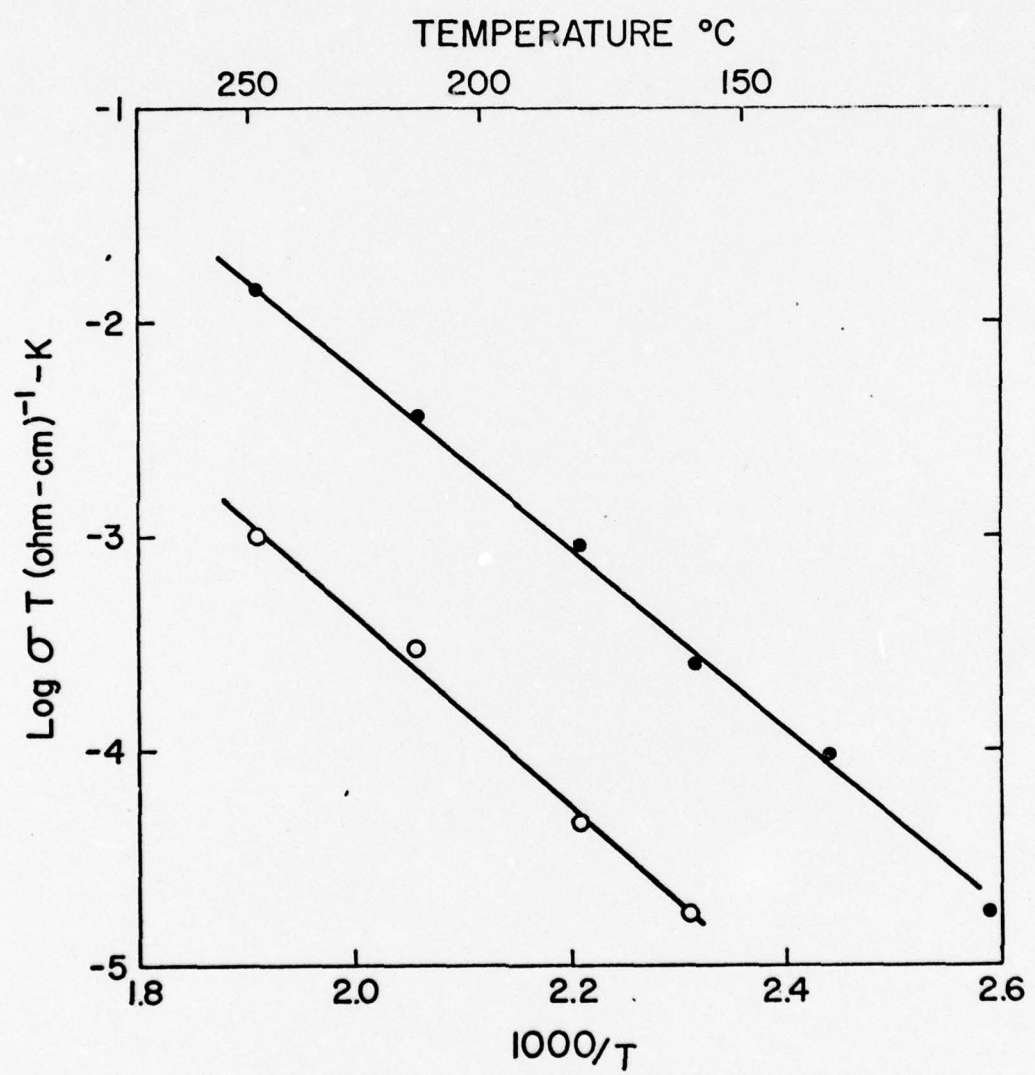


Figure III-38

IV. DEFECT STRUCTURE OF ABX_4 , A_2BX_5 AND A_3BX_6

A. Introduction

Since the thermodynamic treatment of ionic and electronic disorder types in ternary spinels AB_2X_4 by Schmalzried and Wagner [1,2] several authors have used a similar approach to derive possible defect structures of stoichiometric and nonstoichiometric ternary compounds of general composition ABX_3 [2,3], and ABX_4 [4] in order to interpret X_2 -dependent electrical conduction in materials such as CaTiO_3 [3] and CaWO_4 [4].

A recent study of the electrical properties of ternary potassium fluoaluminates and potassium pentachloroferrate III [5] has led to the object of this paper: possible defect structures in stoichiometric and nonstoichiometric compounds of composition ABX_4 , A_2BX_5 and A_3BX_6 , which can be prepared from the binary compounds AX and BX_3 . Here A represents a monovalent cation, B a trivalent cation, and X a monovalent anion.

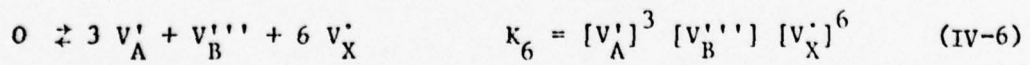
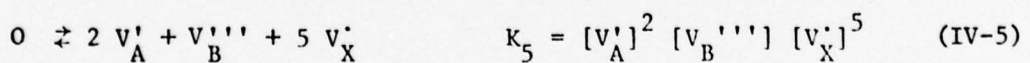
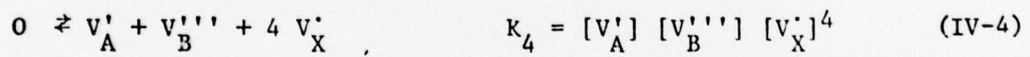
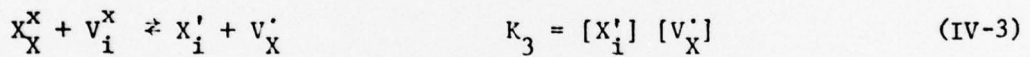
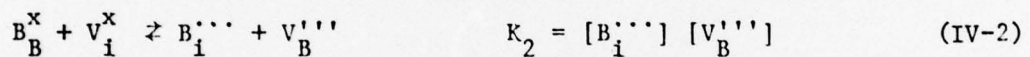
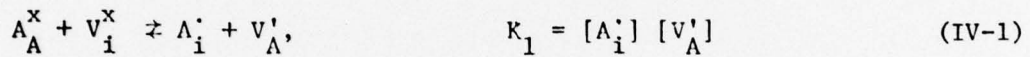
In describing possible incorporation mechanisms for aliovalent impurities we will disregard coupled substitution of two different aliovalent impurities, which would result in electro-neutral compositions without the presence of extrinsic ionic lattice defects. However, use will be made of the addition of appropriate amounts of the binary compounds constituting the ternary compound in order to obtain a balance in lattice sites and a simple regulation of the ionic conductivity of the compounds.

Attention will be partly focused on compounds of composition ABO_4 since Rigdon and Grace [4] limited their treatment to a particular choice of majority defect pairs necessary to describe the conduction results they obtained with CaWO_4 .

Throughout this paper the defect notation as introduced by Kröger and Vink [6] will be used, where ' denotes an effective charge +q, ' an effective charge -q, and ^x stands for zero charge.

B. Intrinsic Equilibria

The thermal generation of ionic lattice defects in stoichiometric ABX_4 , A_2BX_5 and A_3BX_6 can be represented by the quasi chemical reactions (1)-(6). Assuming low concentrations of non-interacting lattice defects leads to the law of mass action expressions $K_1 - K_6$.



The total electroneutrality condition can be represented by

$$[X'_i] + [V'_A] + 3[V''_B] = [V'_X] + [A'_i] + 3[B'''_i] \quad (IV-7)$$

It is expected that intrinsic defect equilibria of the type

$$A''_B \rightleftharpoons A'_i + V'''_B, \text{ and} \quad (IV-8)$$

$$B''_A \rightleftharpoons B'''_i + V'_A \quad (IV-9)$$

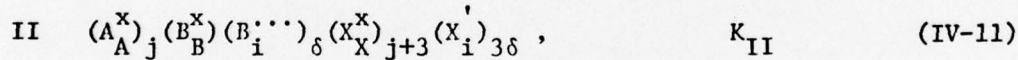
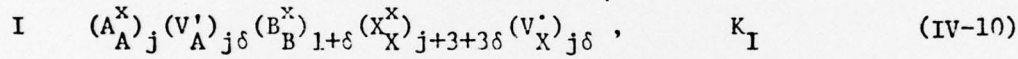
are unlikely in potassium fluoaluminates, potassium pentachloroferrate III, and in CaWO_4 . They will, therefore, not be considered.

In general, one of the above intrinsic defect equilibria predominates in a particular compound, leading to simplified electroneutrality conditions, e.g., $[A'_i] = [V'_A]$ for Frenkel defect formation in the sublattice of the A^+ ions.

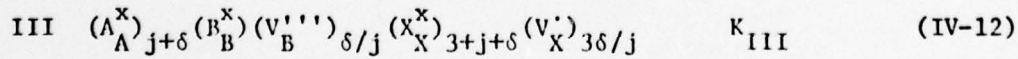
C. Nonstoichiometric Compositions

It is virtually impossible to prepare stoichiometric compounds from mixtures of binary compounds AX and BX_3 . The actual composition of the compound then determines the majority disorder type. In deriving a catalogue of possible majority ionic defect pairs, we have chosen the following representation, since it shows implicitly the appropriate electroneutrality conditions, and the preservation of balance in lattice sites.

In the presence of an excess δ of BX_3 the possible compositions are



For an excess δ of AX the possible compositions are

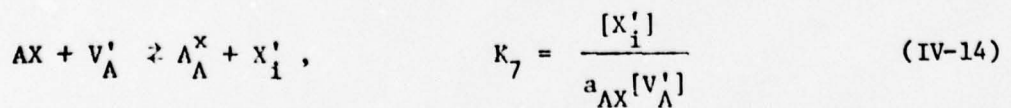


$$IV \quad (A_A^X)_j (A_i^{\cdot})_{\delta} (B_B^X) (X_X^X)_{j+3} (X_i^{\cdot})_{\delta} \quad K_{IV} \quad (IV-13)$$

Nonstoichiometric ABX_4 , A_2BX_5 or A_3BX_6 are represented by a value for j of 1, 2 or 3, respectively.

Relation (7) represents a general total electroneutrality condition. The majority defect pairs V_A^{\cdot} , $B_i^{\cdot\cdot\cdot}$ (excess BX_3) with electroneutrality condition 3 $[B_i^{\cdot\cdot\cdot}] = [V_A^{\cdot}]$, or A_i^{\cdot} , $V_B^{\cdot\cdot\cdot}$ (excess AX) with 3 $[V_B^{\cdot\cdot\cdot}] = [A_i^{\cdot}]$ do not lead to a balance in lattice sites, unless $B_A^{\cdot\cdot\cdot}$, or $A_B^{\cdot\cdot\cdot}$, respectively, are present within the appropriate electroneutrality conditions.

The variation of the ionic lattice defect concentrations as a function of the deviation from stoichiometry can be derived following the method of Schmalzried and Wagner [1], which uses the activity of one of the terminal phases on the pseudo-binary line as an independent variable. In order to ensure a well defined thermodynamic state at a given P_{X_2} . P and T we consider equilibrium with the surrounding atmosphere through the reaction



With the help of the intrinsic defect equilibria (1)-(6),
the formation equilibria of the compounds from AX and BX_3 , and
equilibrium (14) one obtains for the concentration of each
type of lattice defect i the general equation

$$d \ln[i] = n_i d \ln a_{\text{AX}} \quad (\text{IV-15})$$

The characteristic numbers n_i for the disorder types represented
by compositions I - IV, and the intrinsic disorder types are
gathered in Table IV-I.

TABLE IV-I

DEPENDENCE OF THE CONCENTRATIONS OF IONIC LATTICE DEFECTS ON a_{AX}
 FOR THE DISORDER TYPES IN COMPOSITIONS I - IV, AND IN STOICHIOMETRIC
 COMPOUNDS

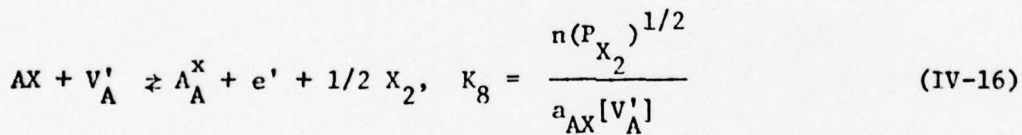
	ABX_4			A_2BX_5			A_3BX_6		
Disorder Type	$n_{A_i^+}$	$n_{B_i^+}$	$n_{X_i^+}$	$n_{A_i^+}$	$n_{B_i^+}$	$n_{X_i^+}$	$n_{A_i^+}$	$n_{B_i^+}$	$n_{X_i^+}$
A_i^+, X_i^+	1/2	-5/2	1/2	1/2	-7/2	1/2	1/2	-9/2	1/2
V_B^{+++}, V_A^+	5/4	-1/4	-1/4	3/2	-1/2	-1/2	7/4	-3/4	-3/4
A_i^+, V_A^+	0	-4	1	0	-5	1	0	-6	1
B_i^{+++}, V_B^{+++}	4/3	0	-1/3	5/3	0	-2/3	2	0	-1
X_i^+, V_X^+	1	-1	0	1	-2	0	1	-3	0
V_A^+, V_X^+	1/2	-5/2	1/2	1/2	-7/2	1/2	1/2	-9/2	1/2
X_i^+, B_i^{++}	5/4	-1/4	-1/4	3/2	-1/2	-1/2	7/4	-3/4	-3/4

D. Electronic Minority Defects

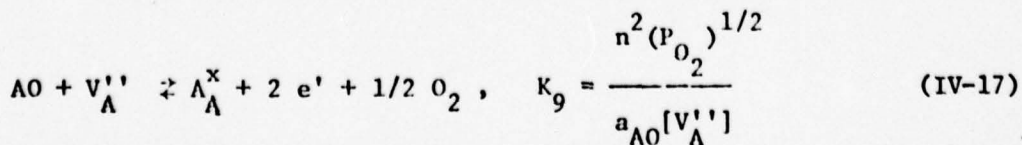
The literature provides examples of mixed ionic and electronic conduction in compounds in which the electronic defects (electrons or holes) are minority defects. When this is the case the electroneutrality condition (7) still holds. The concentrations of the minority defects depend on P_{X_2} , while the concentrations of the majority ionic lattice defects do not. The mixed conductivity originates from the large difference between the mobilities for ionic and electronic species,

$$\mu_e \gg \mu_i .$$

In order to obtain a relation between a_{AX} and the concentrations of the ionic lattice defects, and between a_{AX} and the minority electronic defects we consider for compounds ABX_4 , A_2BX_5 and A_3BX_6 the equilibrium



This equilibrium also applies for ABO_4 compounds with singly ionized ionic lattice defects. For fully ionized defects the equilibrium



may be used. One obtains from (16) for the concentrations of the minority electronic defects as a function of the partial X_2 pressure at fixed P, T, and a_{AX}

$$(\partial \ln n / \partial \ln p_{X_2})_{P, T, a_{AX}} = 1/2 , \quad (IV-18)$$

and as a function of a_{AX} at fixed P, p_{X_2} , and T

$$(\partial \ln n / \partial \ln a_{AX})_{P, p_{X_2}, T} = n_e' = 1 + n_{V_A}' \quad (IV-19)$$

From (17) we obtain

$$(\partial \ln n / \partial \ln p_{O_2})_{P, T, a_{AO}} = -1/4 \quad (IV-20)$$

and

$$(\partial \ln n / \partial \ln a_{AO})_{P, p_{O_2}, T} = n_e^* = 1/2 + 1/2 n_{V_A}' \quad (IV-21)$$

Values for n_e , and for n_e^* , are listed in Table IV-II. The intrinsic electronic equilibrium constant $K_{10} = np$ can now be used to evaluate n_h , and n_h^* . values for the listed defect pairs.

TABLE IV-II

DEPENDENCE OF THE CONCENTRATIONS OF MINORITY ELECTRONIC DEFECTS
ON a_{AX} FOR THE DISORDER TYPES IN COMPOSITION I - IV, AND THE
STOICHIOMETRIC COMPOSITIONS

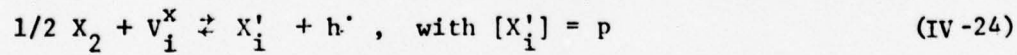
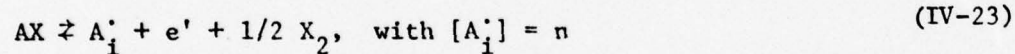
	ABX_4	A_2BX_5	A_3BX_6		ABO_4
Disorder Type	n_e'	n_e'	n_e'	Disorder Type	n_e^*
$\text{A}_i^{\cdot}, \text{X}_i^{\cdot}$	1/2	1/2	1/2	$\text{A}_i^{..}, \text{O}_i^{..}$	1/4
$\text{V}_B^{6\cdot}, \text{V}_X^{\cdot}$	-1/4	-1/2	-3/4	$\text{V}_B^{6\cdot}, \text{V}_0^{\cdot..}$	-1/8
$\text{A}_i^{\cdot}, \text{V}_A^{\cdot}$	1	1	1	$\text{A}_i^{..}, \text{V}_A^{..}$	1/2
$\text{B}_i^{6\cdot}, \text{V}_B^{6\cdot}$	-1/3	-1/6	-2/3	$\text{B}_i^{6\cdot}, \text{V}_B^{6\cdot}$	-1/6
$\text{X}_i^{\cdot}, \text{V}_X^{\cdot}$	0	0	0	$\text{O}_i^{..}, \text{V}_0^{\cdot..}$	0
$\text{V}_A^{\cdot}, \text{V}_X^{\cdot}$	1/2	1/2	1/2	$\text{V}_A^{..}, \text{V}_0^{..}$	1/4
$\text{X}_i^{\cdot}, \text{B}_i^{6\cdot}$	-1/4	-1/2	-3/4	$\text{O}_i^{..}, \text{B}_i^{6\cdot}$	-1/8

E. Equivalent Concentrations of Ionic and Electronic Defects

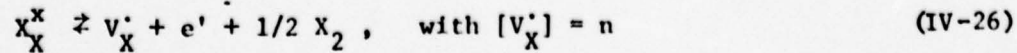
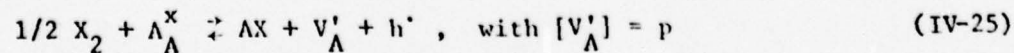
The predominant defects are assumed to be e' , h' , A_i^+ and X_i^+ for compositions with an excess AX , and e' , h' , V_A' and V_X' in the case of excess BX_3 . In addition to the general electroneutrality condition

$$p + [A_i^+] + [V_X'] = n + [V_A'] + [X_i'] \quad (\text{IV-22})$$

the following equilibria may be used to derive relations analogous to (18) and (19); compositions with excess AX



compositions with excess BX_3



It must be noted that the equilibria (16), and (23) - (26) are all interrelated through the intrinsic electronic equilibrium and the intrinsic ionic defect equilibria.

In Table IV-III values for N_i and N_i^* are listed for constant P , T and P_{X_2} ($N_i = \partial \ln [i]/\partial \ln a_{AX}$), and for constant P , T and a_{AX} ($N_i^* = \partial \ln [i]/\partial \ln P_{X_2}$). The values apply for different types of disorder and their respective compositions of ABX_4 , A_2BX_5 , A_3BX_6 and of ABO_4 with partially ionized defects. In Table IV-IV, values for N_i and for N_i^* are listed for ABO_4 with fully ionized defects.

From the assumptions made in this section it follows that for low X_2 partial pressures the electroneutrality condition reads $[V_A'] = [V_X']$, whereas (18) is applicable in this low pressure regime. With the results listed in Table IV-III it can be shown that relation (22) reduces to $[V_A'] = p$ for high partial pressures of X_2 . With an excess of AX, the low X_2 partial pressure regime is governed by $[A_i'] = [X_i']$, whereas at high partial pressures of X_2 relation (22) reduces to $[X_i'] = p$. For the stoichiometric compositions it is assumed that the intrinsic disorder is of the Frenkel type in the X^- ion sublattice, leading to the electroneutrality condition $[X_i'] = p$ in the high X_2 partial pressure regime.

TABLE IV-III
 DEPENDENCE OF THE CONCENTRATIONS OF IONIC AND ELECTRONIC DEFECTS
 ON a_{AX} AND ON P_{X_2} FOR COMPOSITIONS I - IV

Disorder Type	$N_{A_i^+}$	$N_{X_i^+}$	$N_{A_i^+}^*$	$N_{X_i^+}^*$
A_i^+, e^+	1/2	1/2	-1/4	1/4
X_i^+, h^+	1	0	-1/4	1/4
V_A^+, h^+	1/2	1/2	-1/4	1/4
V_X^+, e^+	1	0	-1/4	1/4

TABLE IV-IV

DEPENDENCE OF THE CONCENTRATIONS OF IONIC AND ELECTRONIC DEFECTS
ON a_{AX} AND ON P_{O_2} FOR ABO_4 WITH FULLY IONIZED DEFECTS

Disorder Type	$N_{A_i}^{..}$	$N_{X_i}^{..}$	$N_{A_i}^{*..}$	$N_{X_i}^{*..}$
$A_i^{..}, e'$	1/3	2/3	-1/6	1/6
$O_i^{..}, h'$	1	0	-1/6	1/6
$V_A^{..}, h'$	1/3	2/3	-1/6	1/6
$V_O^{..}, e'$	1	0	-1/6	1/6

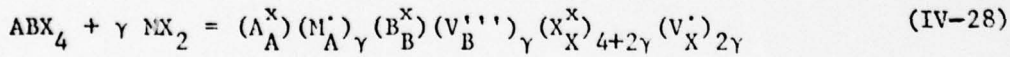
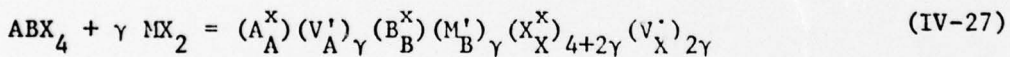
The results of the foregoing sections are presented as defect equilibrium diagrams in Figures IV-1 - IV-3. In addition to the assumptions made in this section, we have constructed the diagrams under the conditions that intrinsic ionic lattice disorder is governed by $[X'_i] = [V_X^*]$ with $[A_i^*] \gg [B_i^{**}]$ and with $[V_A^*] \gg [V_B^{**}]$. For sake of clarity not all the minority defect planes are presented in full detail in Figure 3, which is already rather complex. Moreover, defects in the B^{3+} ion sublattice are not included.

It should be noted that for compositions with an excess of BX_3 , V_A^* and V_X^* constitute the predominant defect pair, and that with an excess of AX the defects A_i^* and X'_i are predominant, irrespective of an intrinsic Frenkel disorder type in either the A^+ or X^- ion sublattice.

F. Influence of Aliovalent Impurities on the Ionic Defect Concentrations

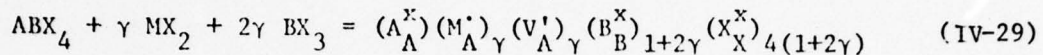
In this section we shall consider the results of the incorporation of aliovalent species into ABX_4 and A_3BX_6 compounds. By influencing the electroneutrality condition and the site balance equations, their presence causes changes in the concentrations of the intrinsic lattice defects, and thus the magnitude and temperature dependence of the electrical conductivity. The compounds are assumed to exhibit pure ionic conduction. We have chosen a method of representation similar to those used to describe the possible undoped nonstoichiometric compositions.

For stoichiometric ABX_4 the following cases can be considered, a) addition of $\gamma \text{ MX}_2$ under the assumption that either defects of the type M'_B or of the type M'_A are formed,

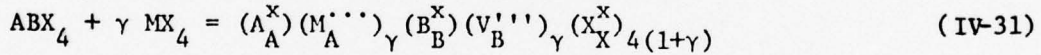
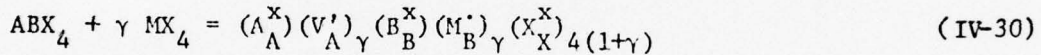


It seems unlikely that MX_2 will be very soluble in ABX_4 via reaction (28). Addition of stoichiometric proportions of BX_3

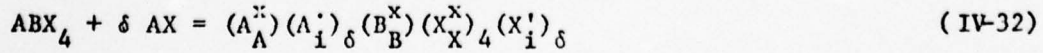
will increase the solubility of MX_2 and will lead to a simple relation between impurity concentration and defect concentration,



b) addition of $\gamma \text{ MX}_4$ under the assumption that either defects of the type M_B^{\cdot} , or of the type $\text{M}_A^{\cdot\cdot\cdot}$ are formed,



On the other hand, incorporation of $\gamma \text{ MX}_2$ into nonstoichiometric ABX_4 with, for instance, composition IV involves further considerations. Composition IV is obtained from the excess AX-regime according to



Following Nassau [11] we can write for K_{IV}

$$K_{IV} = [A_i^+] [X_i'] \quad (IV-33)$$

which, however, represents a true equilibrium constant only when AX is present as a separate phase. K_{IV} then describes the solution equilibrium.

In the dense crystal structure of, for instance, potassium tetrafluor aluminate this type of extrinsic defect pair seems rather unlikely. In other words, the homogeneity region in the excess AX regime is likely to be small. We assume that doping produces defects of the type M_B' as presented by reaction (27) above. Both the intrinsic equilibria and the electroneutrality condition

$$[A_i^+] + [V_X^+] = [V_A^+] + [X_i'] + [M_B'] \quad (IV-34)$$

must still hold. The interstitial anion concentration $[X_i']$ can then be found from the intrinsic equilibrium constants K_1 and K_3 along with the solution equilibrium K_{IV}

$$\{x'_i\} = -[M'_B]/\Lambda + \{([M'_B]/\Lambda)^2 + 2(\kappa_3 + \kappa_{IV})/\Lambda\}^{1/2} \quad (IV-35)$$

with $\Lambda = 2(\kappa_1/\kappa_{IV} + 1)$.

A decrease in the concentration of x'_i and an increase in the concentration of A'_i will result for γ of the order of δ . For $\gamma \gg \delta$ we obtain the composition

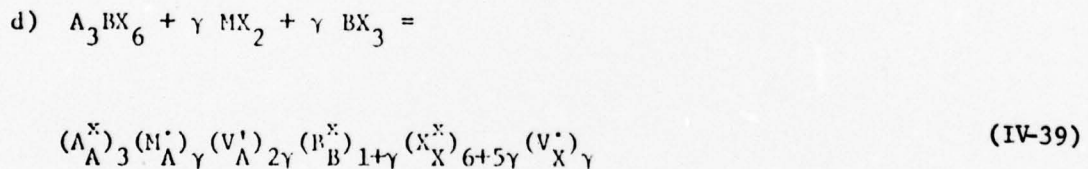
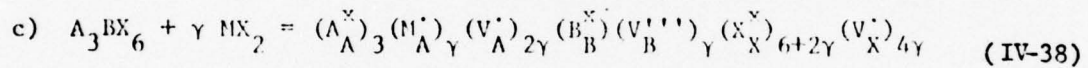
$$(A_A^X)_{1+\delta} (V_A')_{\gamma-\delta} (B_B^X)_{M'_B} (M'_B)_\gamma (X_X^X)_{4+2\gamma+\delta} (V_X')_{2\gamma-\delta} \quad (IV-36)$$

In other words, the compound ABX_4 has been doped with δ AMX_3 and with $(\gamma-\delta)$ MX_2 . Here δ represents the total amount of AX that is present, both in the form of a separate phase and as A'_i and X'_i in the lattice. This composition is essentially the same as composition I with M'_B defects, i.e.,

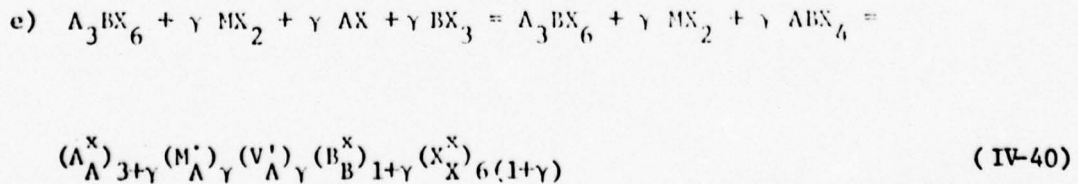
$$(A_A^X)_{1+\delta} (V_A')_{\gamma+\delta} (B_B^X)_{1+\delta} (M'_B)_\gamma (X_X^X)_{4+3\delta+2\gamma} (V_X')_{2\gamma+\delta} \quad (IV-37)$$

For a compound exhibiting ionic conduction via vacancies in the A^+ ion sublattice, the compounds represented by composition (36) and (37) will show different conductivity versus MX_2^- isotherms for moderate dopant levels. However, for $\gamma \gg \delta$ both compositions will show the same dependence of the conductivity on the MX_2^- concentration.

In doping stoichiometric A_3BX_6 compounds with MX_2^- under the assumption that M_A^+ defects are formed, one may consider several possibilities. They include compensation effects through additions of either BX_3 , or both BX_3 and AX in the appropriate stoichiometric proportions.



and



Stabilization of the composition expressed by reaction (38) through annihilation of vacancies via the intrinsic equilibrium (6), whereby A_i^+ and X_i^- defects are formed, preserving charge neutrality and balance in lattice sites seems energetically favorable.

However, again it is anticipated that the solubility of MX_2 will be larger in the presence of the binary compounds AX and BX_3 .

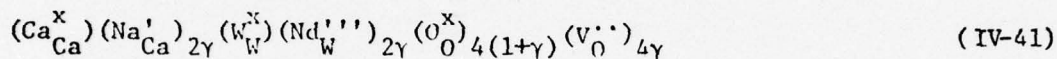
Dopant reactions for MX_2 with formation of M_B^+ , and for MX_4 with the formation of either M_A^{++} or M_B^+ can be easily worked out in a manner analogous to the reactions for compounds of composition ABX_4 .

G. Discussion and Concluding Remarks

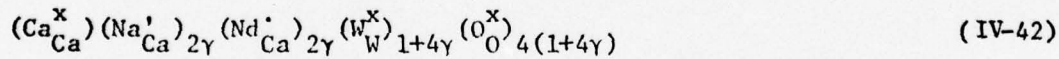
Considerations of the possible disorder types discussed here can be used as a guide in the elucidation of conductivity data for stoichiometric and nonstoichiometric ABX_4 , A_2BX_5 and A_3BX_6 compounds. However, these considerations offer in several situations no conclusive answers. This may be illustrated with compounds exhibiting mainly electronic conduction, while electronic species are in fact minority species. Relation (18) and the data gathered in Tables IV-I and IV-II show that a selection of the predominant ionic lattice defect pair based on the results of P_{X_2} -dependent measurements including equilibrium experiments with AX , cannot be as conclusive as desired.

Examination of the crystal structures could lead to a preference for vacancy pairs, or the intrinsic defect pairs given by reactions (1) and (3), instead of pairs of interstitial defects. This means that the homogeneity region in the excess AX regime for such compounds is assumed to be smaller than in the excess BX_3 regime. Such considerations are often included in the analysis of diffusion or conduction data. Gupta and Weirick [7] studied the self diffusion of Ca in CaWO_4 single crystals doped with neodymium and sodium for charge compensation. They proposed a vacancy mechanism for calcium diffusion. This mechanism originated from the assumption that the most probable defect structure in CaWO_4 would consist of the vacancy pair $\text{V}_{\text{Ca}}^{\prime\prime}, \text{V}_0^{\prime\prime}$, because of the dense packing of CaWO_4 , which

crystallizes in the scheelite structure. A spectrographic analysis of the samples showed about 1 or 3 atom percent each of Na and Nd calculated on the basis of occupancy of Ca^{2+} and W^{6+} sites, i.e., the defects Na'_{Ca} and Nd'''_{W} [7]. For equimolar proportions γ of Na_2O and Nd_2O_3 one should obtain the composition



An extrinsic concentration of V''_{Ca} would result for ratios $\text{Na}_2\text{O}/\text{Nd}_2\text{O}_3 < 1$. Under the assumption that both Na^+ ions and Nd^{3+} ions enter the calcium ion sublattice in equal proportions the composition that results can be represented by



In order to obtain this composition a proper amount of $\text{WO}_3(4\gamma)$ has to be added too. For variable ratios of Na_2O and Nd_2O_3 together with proper amounts of WO_3 it should be possible to obtain compositions with vacancies in the Ca^{2+} and O^{2-} sublattices [11].

Although the crystal structure of CaWO_4 is favorable for the existence of vacancies in the calcium ion and oxide ion

sublattices, their presence in the crystals Gupta and Weirick [7] used originated from the presence of the aliovalent impurities, Na and Nd.

According to Rigdon and Grace [4] the vacancy pair $v_{\text{Ca}}^{..}$, $v_0^{..}$ cannot explain their conductivity results. These authors studied the ac- and dc conductivity of undoped CaWO_4 in equilibrium with $\text{H}_2\text{O}-\text{H}_2-\text{Ar}$ gas mixtures. The conductivity is mainly electronic (n type), electrons being present as minority defects. Isothermal conductivity versus $P_{\text{H}_2\text{O}}/P_{\text{H}_2}$ plots revealed a slope of about -1/2. These authors made a selection from the intrinsic defect pairs, $A_i^{..}$, v_B^6 ; $O_i^{..}$, $v_0^{..}$; $v_A^{..}$, B_i^6 , the former and the latter pair originating from intrinsic defect equilibria analogous to reactions (8) and (9), which are, however, not likely to occur. Moreover significant concentrations of defects with such a high electrical charge are unlikely. Frenkel defects in the oxide ion sublattice were selected on the basis of the conductivity results.

Since electrons are minority defects (20) should hold, and due to their experimental circumstances, the relation

$$\partial \ln n = -1/2 \partial \ln(P_{\text{H}_2\text{O}}/P_{\text{H}_2}) = -1/4 \partial \ln P_{\text{O}_2} \quad (\text{IV-43})$$

holds. However, this conductivity behavior is independent of the identity of the predominant type of defect pair, and therefore, also of deviation from stoichiometry, if present.

In neither of the studies mentioned above were the crystal compositions discussed in detail. Excess W_3 or CaO are both readily soluble in $CaWO_4$ in small amounts [8]. However, the amount of CaO will be less than the amount of W_3 . $CaWO_4$ with an excess of W_3 has a green coloration, while with an excess of CaO the crystal becomes brown. In addition to conductivity experiments, doping experiments like reaction (36) should provide useful information about $CaWO_4$ with excess CaO , especially in the high O_2 partial pressure regime, where the transference number for electrons is expected to be less than 1.0.

Solid solutions between A_3BX_6 and MX_2 have been reported in the literature [9, 10]. According to Holm [9] there exists no significant solid solubility between Na_3AlF_6 (cryolite) and CaF_2 . With the assumption that calcium ions replace sodium ions, reaction (38) would describe the incorporation of CaF_2 into the cryolite lattice. Dewing [10] pointed out that CaF_2 would be soluble in solid cryolite only in the presence of excess AlF_3 , since then the fluoride ions from CaF_2 could enter the structure as AlF_6^{3-} . To confirm this expectation, Dewing

measured the electrical conductivity of undoped cryolite, and of cryolite crystals obtained from a melt containing 10 percent CaF_2 and 7.2 percent AlF_3 . The crystals obtained from this melt contained 6.9 percent CaF_2 . With the assumption that all the AlF_3 was incorporated as well, these figures imply that equimolar proportions of CaF_2 and AlF_3 were incorporated in the lattice, in accordance with reaction (39). A doping experiment following reaction (40) and concomitant conductivity experiments should help to clarify the basis for the observed increase in conductivity of cryolite doped with CaF_2 and AlF_3 .

H. References for Section IV.

- [1] H. Schmalzried and C. Wagner, *Z. Phys. Chem.* 31, 198 (1962).
- [2] H. Schmalzried, *Progr. Solid State Chem.* 2, 265 (1965).
- [3] W. L. George and R. E. Grace, *J. Phys. Chem. Solids* 30, 881 (1969).
- [4] M. A. Rigdon and R. E. Grace, *J. Amer. Ceram. Soc.* 56, 475 (1973).
- [5] J. Schoonman and R. A. Huggins, to be published.
- [6] F. A. Kröger and H. J. Vink, *Solid State Phys.* 3, 307 (1956).
- [7] Y. P. Gupta and L. J. Weirick, *J. Phys. Chem. Solids* 28, 2545 (1967).
- [8] K. Nassau and G. M. Loiacono, *J. Phys. Chem. Solids* 24, 1503 (1963).
- [9] J. L. Holm, *Acta Chem. Scand.* 22, 104 (1968).
- [10] E. W. Dewing, *Trans. Met. Soc. AIME* 245, 1829 (1969).
- [11] K. Nassau, *J. Phys. Chem. Solids* 24, 1511 (1963).

I. Figure Captions for Section IV.

Figure 1. Defect Equilibrium Diagram for ABX_4 , A_2BX_5 and
 A_3BX_6 with Composition I.

Figure 2. Defect Equilibrium Diagram for ABX_4 , A_2BX_5 and
 A_3BX_6 with Composition IV.

Figure 3. Three-dimensional Equilibrium Diagram for ABX_4 , A_2BX_5
and A_3BX_6 Under the Conditions Mentioned in the
Text.

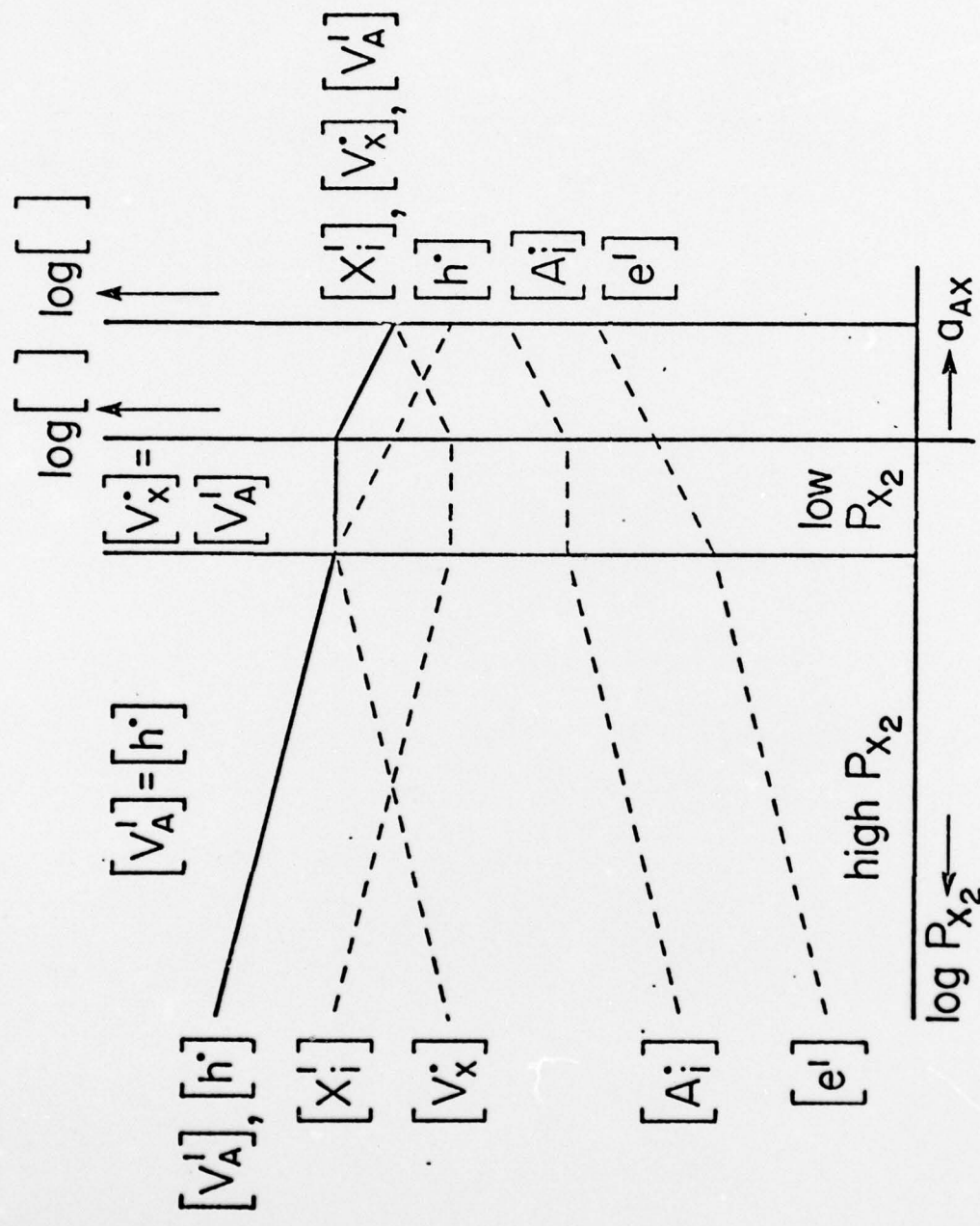


Figure IV-1

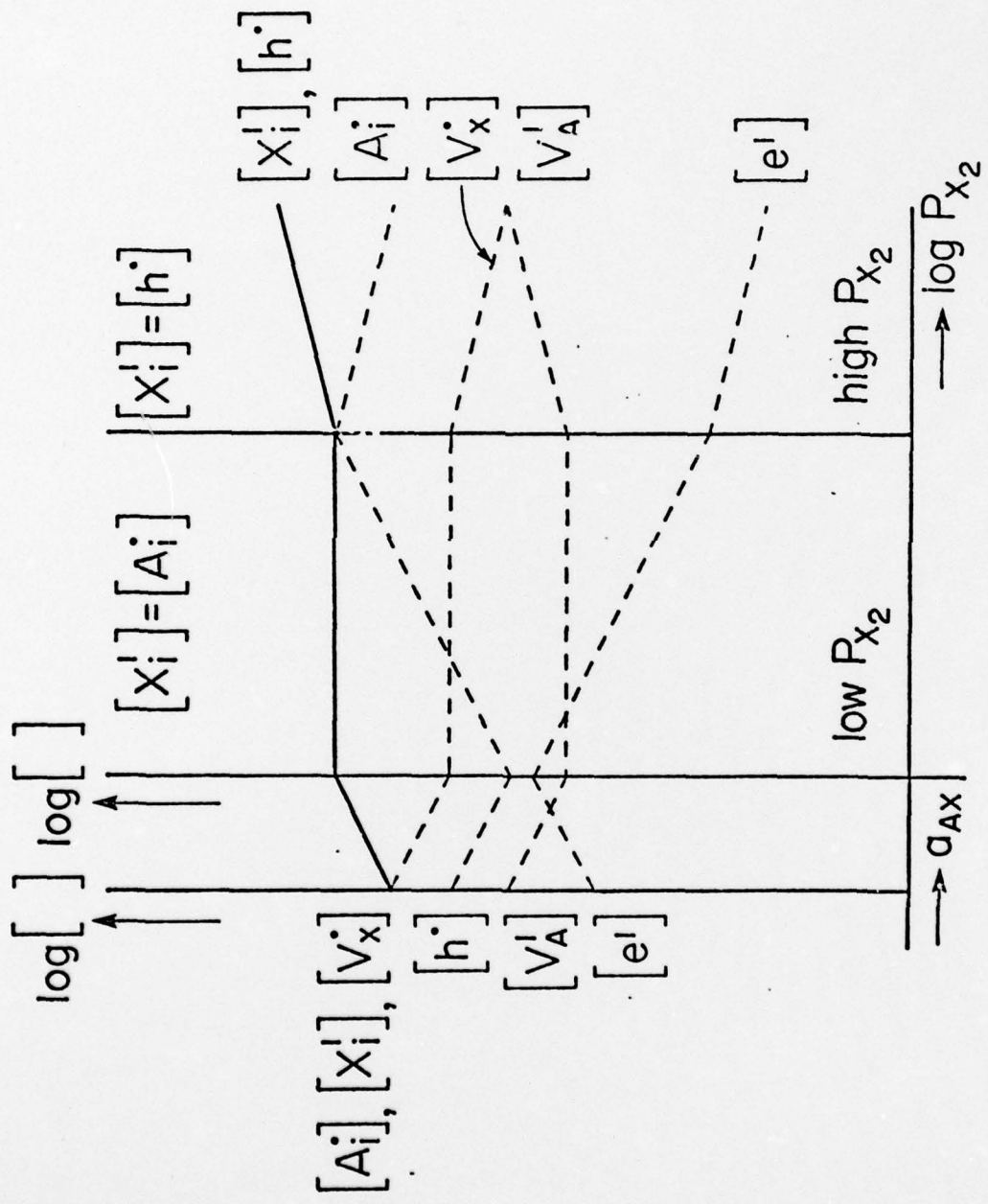


Figure IV-2

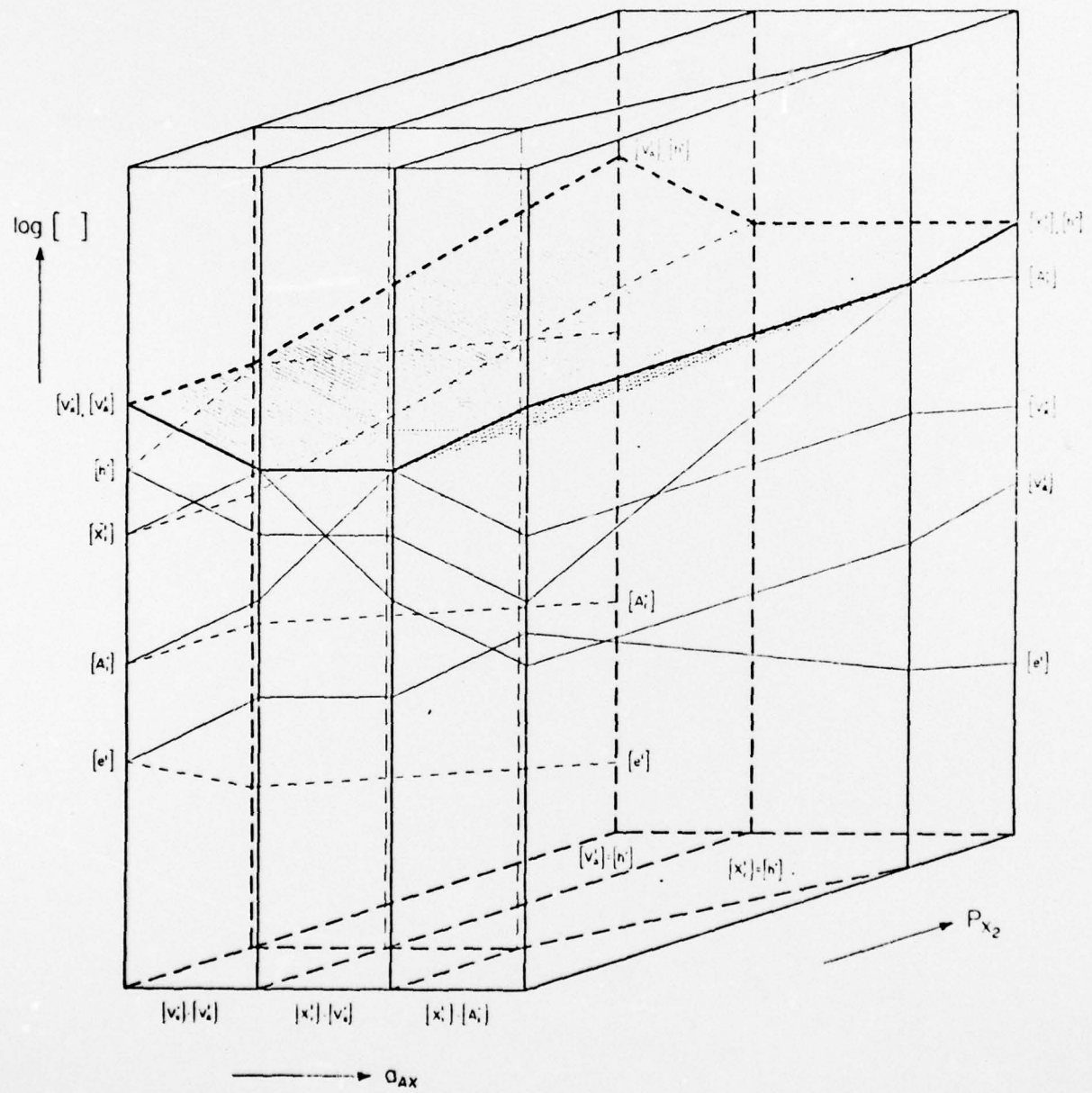


Figure IV-3

V. GRAPHITE INTERCALATION COMPOUNDS

A. Introduction

In our previous technical report [1], we detailed the potential of graphite intercalation compounds in solid state battery systems. We report here on work completed since that time.

B. Carbon/Fluorine Systems

Both known graphite/fluorine compounds, C_4F and CF , have been investigated as possible solid state cathode materials. Carbon monofluoride is in fact now commercially available in a battery utilizing a lithium anode.

In Technical Report 2, we pointed out that C_4F , as commonly prepared, contains not only two distinct fluorine NMR resonances but also a proton resonance. We reconciled these observations with the existence of both internal fluorine and an external HF layer. We have now confirmed this behavior with pulsed NMR studies of the decay envelope of the fluorine resonance.

An unexpected result was obtained in the case of carbon monofluoride. Second moment studies of the fluorine resonance indicated that the previously assumed trans-cyclohexane chair arrangement, illustrated in Figure V-1, was incorrect and that the most likely structure was one containing a cis-trans arrangement of cyclohexane boats (illustrated in Figure V-2).

Details of the second moment calculations are given in Figure V-3.
This work has been published in the Journal of the American
Chemical Society [2].

C. Graphite/Antimony Pentafluoride System

Our initial work on this compound has been published in communication form [3]. Since then, we have found that the rapid motion of SbF_5 found in SP-1 graphite/ SbF_5 is present over a wide range of stoichiometries and graphite particle sizes.

D. References for Section V.

- [1] R. A. Huggins, "Solid Electrolyte Battery Materials",
Technical Report #2, March 31, 1974, ONR Task No.
NR 056-555, pp. 134-141.
- [2] L. B. Ebert, J. I. Brauman and R. A. Huggins, J. Amer.
Chem. Soc. 96, 7841 (1974).
- [3] L. B. Ebert, R. A. Huggins and J. I. Brauman, J. C. S.,
Chem. Comm., 924 (1974).

E. Figure Captions for Section V.

Figure 1: The Previously Accepted Rudorff "Chair" Model
of CF.

Figure 2: Boat CF.

Figure 3: Boat Model/Chair Model.

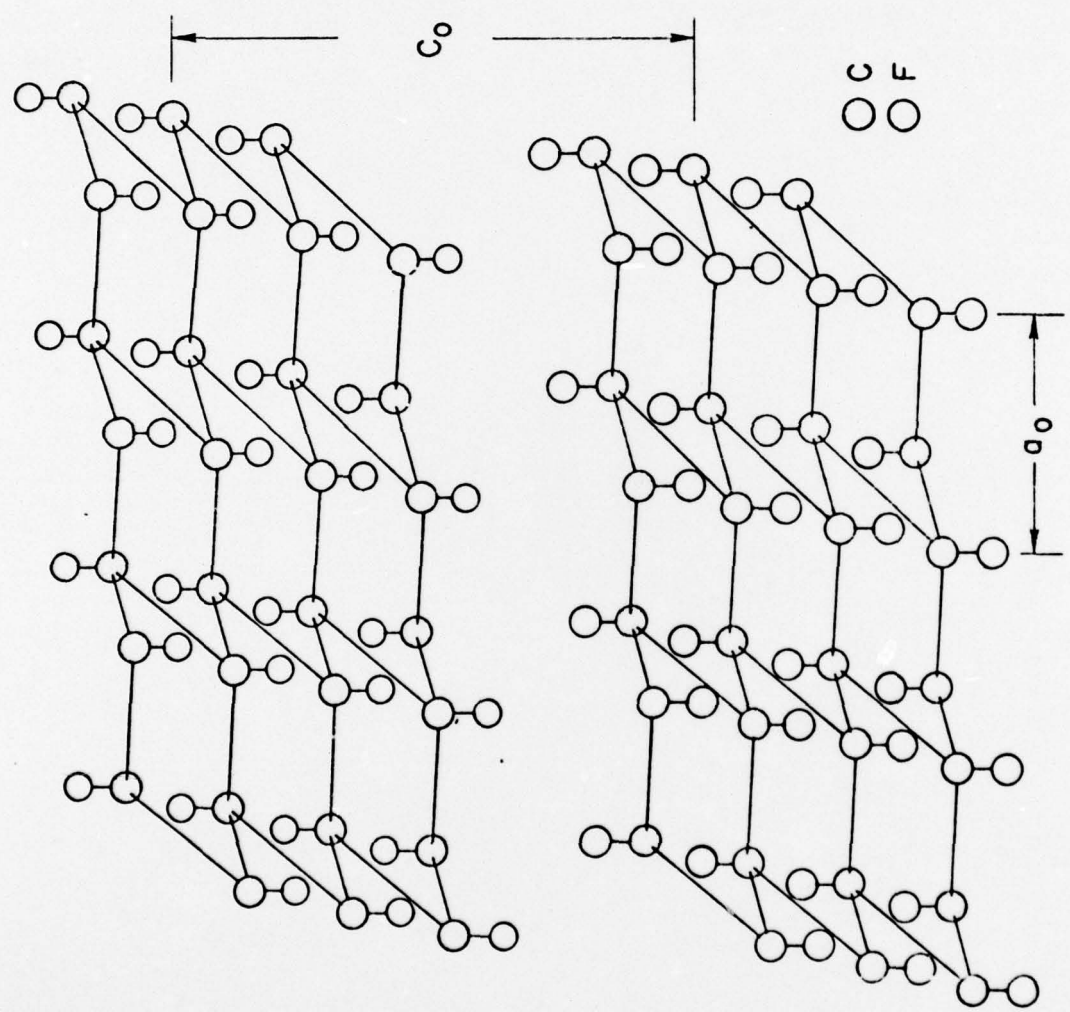


Figure V-1.

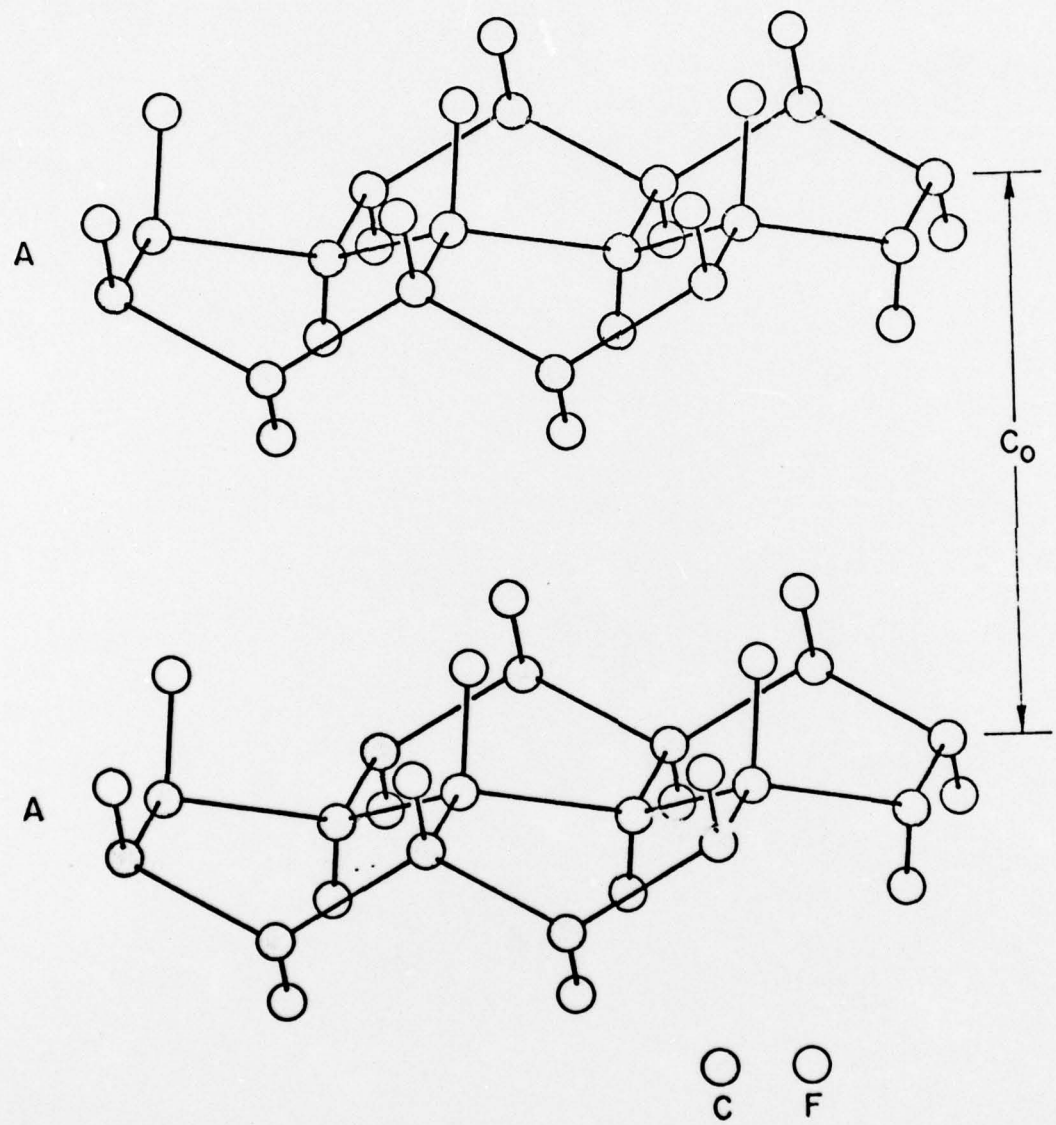


Figure V-2.

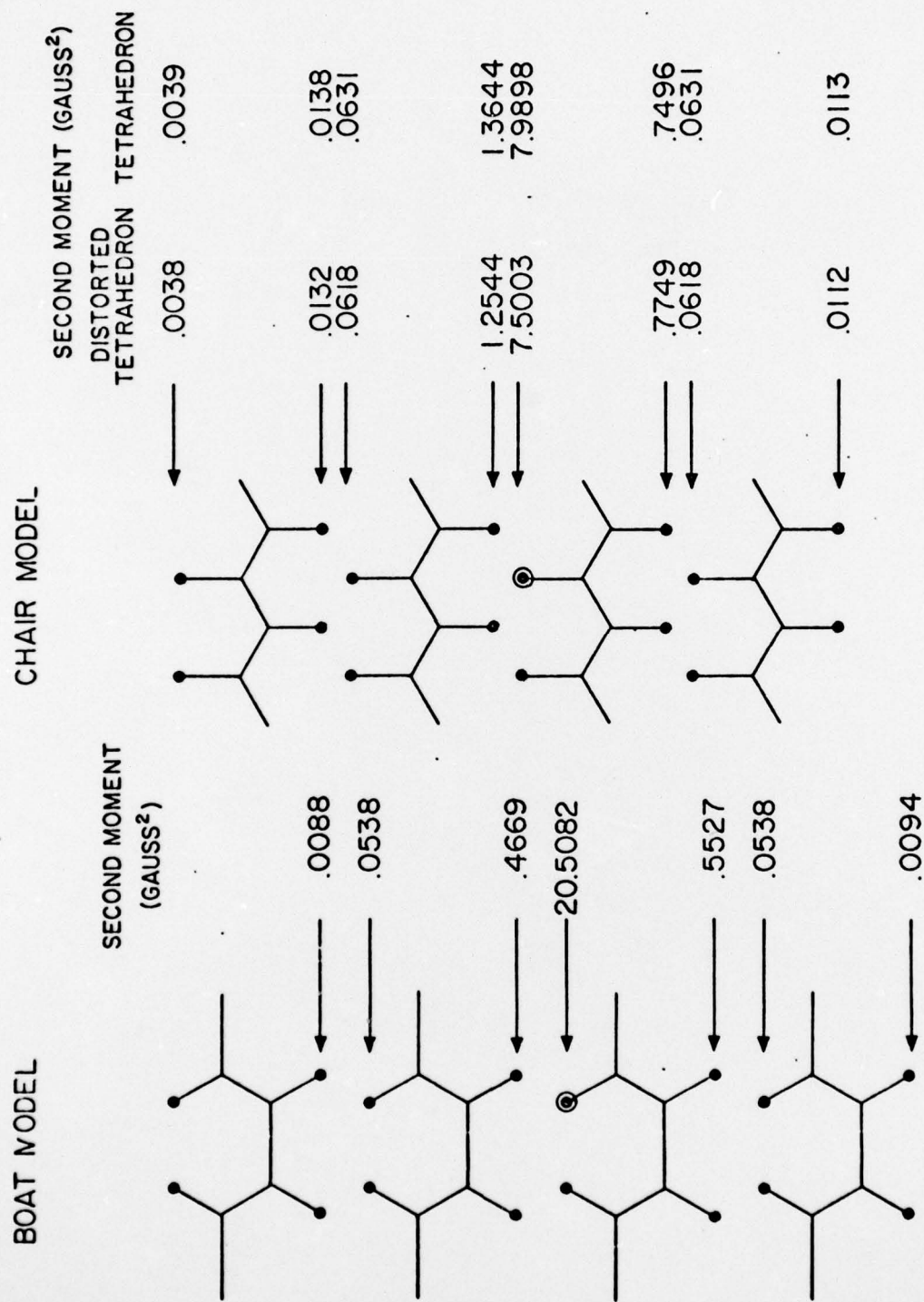


Figure V-3.

VI. OTHER POTENTIAL SOLID ELECTROLYTES OR MIXED CONDUCTORS

Work continues on several other materials with structures of potential interest for use in understanding solid electrolytes and mixed conductors. These include the fluorides $KAlF_4$, K_2AlF_5 , K_3AlF_6 , Li_3AlF_6 , and Na_3AlF_6 . Related materials are $K_2FeCl_5 \cdot H_2O$ and $K_2Mg_2(SO_4)_3$. Others with which we have been working for some time, and which were mentioned in earlier reports, are hollandite, $K_xMg_{x/2}Ti_{(8-x/2)}O_{16}$, and ramsdellite, $Li_2Ti_3O_7$. The activation energy for lithium ion motion in the latter material has been determined from NMR measurements to be about 3.8 kcal/mole. Direct conductivity experiments also indicate high lithium mobility, with an ionic conductivity at 400°C of about $5 \times 10^{-3} (\text{ohm-cm})^{-1}$. The electronic component of the total conductivity at that temperature is about 1%, according to measurements made on samples to date.

VII. DISTRIBUTION LIST

Dr. Paul Delahay New York University Department of Chemistry New York, New York 10003	1	Dr. T. Katan Lockheed Missiles & Space Co. P. O. Box 504 Sunnyvale, Calif. 94088	1
Dr. R. A. Osteryoung Colorado State University Department of Chemistry Fort Collins, Colorado	1	Dr. Joseph Singer Code 302-1 NASA-Lewis 21000 Brookpark Road Cleveland, Ohio 44135	1
Dr. E. Yeager Case Western Reserve Univ. Department of Chemistry Cleveland, Ohio 44106	1	Dr. D. R. Cogley EIC Incorporated Five Lee Street Cambridge, Massachusetts 02139	1
Dr. A. Heller GTE Laboratories, Inc Waltham Research Center 40 Sylvan Road Waltham, Mass. 02154	1	Library P. R. Mallory and Co., Inc. P. O. Box 706 Indianapolis, Indiana 46206	1
Dr. D. N. Bennion University of California Energy Kinetics Dept. Los Angeles, Calif. 90024	1	Office of Naval Research Code 472 Arlington, Virginia 22217	2
Dr. J. W. Kauffman Northwestern Univ. Department of Materials Science Evanston, Illinois 60201	1	ONR Branch Office 536 S. Clark Street Chicago, Illinois 60605 Attn: Dr. George Sandoz	1
Dr. R. A. Marcus Univ. of Illinois Dept. of Chemistry Urbana, Illinois 61801	1	ONR Branch Office 207 West 24th Street New York, New York 10011 Attn: Scientific Dept.	1
Dr. M. Eisenberg Electrochimica Corp. 2485 Charleston Road Mountain View, Calif. 94040	1	ONR Branch Office 1030 East Green Street Pasadena, California 91106 Attn: Dr. R. J. Marcus	1
Dr. S. J. Szpak Naval Electronics Laboratory, Inc. 271 Catalina Boulevard San Diego, Calif. 92152	1	ONR Branch Office 760 Market Street, Rm. 447 San Francisco, Calif. 94102 Attn: Dr. P. A. Miller	1

ONR Branch Office 495 Summer Street Boston, Massachusetts 02210 Attn.: Dr. L. H. Peebles	1	Naval Ship Research & Development Center Annapolis Division Annapolis, Maryland 21402 Attn.: Dr. Allan Evans Code 2833	1
Director Naval Research Laboratory Washington, D.C. 20390 Attn: Library, Code 2029 6 (ONRL) Technical Info.Div. 1 Code 6100, 6170 1		Commander Naval Undersea Research & Development Center San Diego, Calif. 92132 Attn.: Tech. Library Code 133	1
The Asst. Secretary of the Navy (R&D) Department of the Navy Room 4E736 Pentagon Washington, D.C. 20350 1		Naval Weapons Center China Lake, Calif. 93555 Attn.: Head, Chemistry Division	1
U. S. Naval Ordnance Lab. 1 White Oak Silver Spring, Maryland 20910 Attn: Code 230		Naval Civil Engineering Laboratory Port Hueneme, California 93041 Attn.: Mr. W. S. Haynes	1
Commander, Naval Air Sys. 1 Command Department of the Navy Washington, D.C. 20360 Attn: Code 310C (H.Rosenwasser)		Professor O. Heinz Dept, Physics and Chemistry Naval Postgraduate School Monterey, Calif. 93940	1
Defense Documentation Center Building 5, Cameron Station Alexandria, Virginia 22314	12	Dr. A. L. Slafkosky Scientific Advisor Commandant of the Marine Corps (Code RD-1) Washington, D.C. 20380	1
U. S. Naval Oceanographic Office 1 Library, Code 1640 Suitland, Maryland 20390		Army Research Office - Durham 1 Box CM, Duke Station Durham, North Carolina 27706 Attn.: CRD-AA-IP	
		Dr. S. Schuldiner Naval Research Laboratory Code 6160 Washington, D.C. 20375	1